Nanometer-Scale Structural and Electronic Properties of Low Dimensional Heterostructures

by

Vaishno Devi Dasika

A dissertation submitted in partial fulfillment
of the requirements for the degree of
Doctor of Philosophy
(Electrical Engineering)
in The University of Michigan
2010

Doctoral Committee:

Professor Rachel S. Goldman, Chair
Professor Pallab K. Bhattacharya
Professor Roy Clarke
Associate Professor Jamie Phillips

Dedication

Dedicated to my parents

Table of Contents

List of Figures

List of Tables

List of Appendices

Abstract

Nanometer-Scale Structural and Electronic Properties of Low Dimensional Heterostructures

by

Vaishno Devi Dasika

Chair: Rachel S. Goldman

Mercury cadmium telluride (MCT) based heterostructures and InAs/GaAs quantum dots have enabled significant advances in optoelectronic devices such as light emitters and detectors. In both cases, the atomic-scale structural and electronic properties of the heterostructure interfaces remain the least understood aspect of the devices. Further advances will require an improved understanding of issues such as interface abruptness, alloy non-uniformities, and local band-offsets. In this dissertation, the nanometer-scale structural and electronic properties of II-VI substrates and InAs/GaAs dots are investigated using a combination of cross-sectional scanning tunneling microscopy (XSTM) and variable separation scanning tunneling spectroscopy (STS).

The influence of crystal orientation and thickness on the cleavage of CdTe and $Cd_{1-x}Zn_xTe$ substrates, as well as the influence of In doping and annealing on the substrate resistivity are explored. The flattest cleaves were obtained for 900 μm thick (111) CdTe and $Cd_{1-x}Zn_xTe$ wafers cleaved along [110]. Furthermore, after In-doping ($n \sim 2.2 \times 10^{17}$ cm^{-3}) and post-growth annealing (T = 750 °C) in a Cd-rich environment, the

CdTe substrate resistivity was reduced to 0.04 Ω-cm, and XSTM measurements were performed.

The influence of surrounding $In_{0.2}Ga_{0.8}As$ alloy layers on the size and distribution of InAs/GaAs dots, as well as the thickness of the surrounding wetting layer (WL) are examined. XSTM images reveal that the surrounding alloy layers promoted a 38% (71%) increase in average dot diameter (height), and a three-fold increase in WL thickness. A strain-based mechanism for dot formation and collapse in the absence and presence of alloy buffer and capping layers is proposed.

The origins of electronic states in individual, uncoupled dots and the surrounding WL are investigated using a combination of XSTM and STS. Room temperature STS spectra reveal a gradient in the effective bandgap within the dots with smallest values near the dot core and top surfaces. The variations in effective bandgap are apparently dominated by indium composition gradients, with minimal effects due to dot shape and strain. Indium composition gradients also dominate the effective bandgap variations in the WL.

Chapter 1

Introduction

1.1 Overview

Over the past few decades, advances in semiconductor thin film growth have enabled the fabrication of semiconductor heterostructures with nanometer-scale precision.[1-26] Using growth techniques such as molecular beam epitaxy (MBE), it is possible to confine the dimensions of a semiconductor to < 1 nm.[25-33] Furthermore, through the formation of heterostructures consisting of materials with differing bandgaps, it is possible to tailor the local energy band offsets to confine or redistribute charge carriers, thereby influencing the optical and electronic properties of the material.[27-33] Built-in strain fields can also be utilized to alter the structural properties of heterostructures, thus enhancing their optoelectronic properties.[34-37] For example, the accumulated strain in InAs films leads to the formation of self-assembled quantum dots on GaAs via the Stranski-Krastanow growth mode transition.

Typically, the active regions of heterostructures used in optoelectronic devices are at the interfaces. However, the atomic scale structural and electronic properties of the heterostructure interfaces are generally the least understood aspects of the devices. For example, low dimensional heterostructures composed of mercury cadmium telluride (MCT or $Hg_{1-x}Cd_xTe$) are a common choice for use in infrared (IR) detectors since they are the only material sensitive to short-wavelength (1.4 – 3 μm, $x > 0.3$), mid-wavelength (3 – 5 μm, $x \sim 0.3$), and long-wavelength (8 – 14 μm, $x \sim 0.2$) IR radiation.[38-44] However, previous studies of MCT based infrared detectors have revealed significant concentrations of point defect clusters, dislocations, and alloy non-uniformities in MCT heterostructures, and the influence of these defects on detector performance remain unknown.[45-53]

Furthermore, strain-induced self-assembled InAs/GaAs quantum dots have enabled significant advances in several devices including light emitters and detectors, nano-biological devices, field-effect transistors, and quantum computing elements.[18-26] The structure of the dots can be influenced by a variety of growth parameters including substrate temperature, III/V flux ratio, growth rate, the presence of surrounding alloy layers, and post-growth intermixing.[1-17] For example, it has been reported that InAs dots grown on InGaAs buffers have higher densities than those grown directly on GaAs.[1-3] However, there have been conflicting reports on the effect of alloy buffers on dot size; thus, the influence of alloy buffer layers on dot size and WL thickness remains unknown. Furthermore, it has been suggested that capping InAs dots with InGaAs in lieu of GaAs minimizes the tendency for the reduction in dot height upon capping, often termed dot "collapse".[4-6] However, to date, the influence of alloy capping layers has primarily been investigated qualitatively using plan-view STM or AFM,[4,5] and therefore, the quantitative structure of the buried dots was not resolved.

In addition, several reports have suggested that the dots and the surrounding wetting layer (WL) often have non-uniform compositions across their width and height due to indium segregation and inter-diffusion at the InAs/GaAs interfaces.[54-63] However, to date, the effect of these compositional variations on the QD and WL electronic states remains unknown.

Thus, there exists a need to obtain nanometer-scale spatially resolved structural and electronic information from low-dimensional heterostructures. This chapter is organized as follows. First, methods typically used for examining the structural and electronic properties of heterostructures are described, with an emphasis on cross-sectional scanning tunneling microscopy and spectroscopy. Then, interface issues in MCT heterostructures are discussed. This is followed by an introduction to InAs/GaAs dots, and the influence of growth conditions on dot structure. In addition, the influence of nanometer-scale structural variations on the dot electronic states is discussed. The chapter concludes with an outline of the dissertation.

1.2 Methods for Examining the Structural and Electronic Properties of Materials

Various techniques are available for the investigation of interfaces in low dimensional heterostructures, including high-resolution transmission electron microscopy (TEM), cross-sectional scanning tunneling microscopy (XSTM), photoluminescence (PL) spectroscopy, scanning tunneling spectroscopy (STS) and capacitance-voltage (C-V) spectroscopy. High resolution TEM often has a lateral resolution on the order of angstroms. However, the data consist of an average of the foil thickness, which is typically on the order of 100's of Ås.[64] C-V spectroscopy typically involves the measurement of the differential capacitance of a *p-n* or *p-i-n* heterostructure as a function of the applied bias voltage. A variation in the applied bias modifies the depletion width in the heterostructure. Thus, sweeping the applied voltage moves the depletion region through the layers of the heterostructure, thereby altering the region of the heterostructure that contains charged carriers. In the case of QDs, for certain bias values, peaks corresponding to QD energy levels, appear in the C-V spectra.[65] The energy resolution is on the order of kT, and therefore, at low temperatures, the spacing between the sub-bands in the conduction and valence bands can be measured. However, the data typically corresponds to a spatial average over 100's of microns, so the spatial resolution for this measurement technique is limited.[66-69] To measure the energy difference between of the confined electron and hole states in low dimensional heterostructures, PL is commonly used.[70-73] However, PL spectra correspond to a spatial average whose interpretation requires several assumptions regarding interface abruptness, alloy composition, and lateral uniformity.[74,75] In addition, due to the fast decay times of the excited electron and hole states, PL is typically most sensitive to the energy difference between the ground electron and hole states.[75]

Cross sectional scanning tunneling microscopy (XSTM) allows direct observations of the spatial distribution of individual atoms on the surface.[76-81] One of the main advantages of XSTM is that the collected images are associated primarily with the top layer of the cleaved surface, instead of an average over many layers. As a result, it is possible to resolve the atomic-scale features of heterostructures over macroscopic length scales using XSTM. In addition, scanning tunneling spectroscopy (STS), which allows spatially-resolved electronic measurements within single layers of semiconductors, is a promising alternative to methods such as C-V and PL. In this dissertation, II-VI substrates were designed by the author, for the subsequent growth of MCT-based heterostructures for XSTM studies. The structural properties of InAs/GaAs quantum dot heterostructures were examined using XSTM. The electronic properties of the layers, such as the effective bandgap, i.e., the difference between the confined state energies, were measured by variable separation STS.

1.3 Mercury Cadmium Telluride Based Heterostructures

Mercury cadmium telluride (MCT or $Hg_{1-x}Cd_xTe$) has been used in the fabrication of infrared (IR) detectors since 1958.[38] MCT photodiodes have demonstrated high optical absorption coefficients and quantum efficiencies, and low thermal generation rates.[42] A variety of detectors and focal plane arrays have been fabricated using MCT based heterostructures.[43,44] However, dark currents, i.e. currents which are present in the absence of illumination, often limit the performance of MCT detectors. Issues at the interfaces of the heterostructure, such as alloy non-uniformities, interface abruptness, and point defects are expected to be the primary sources of dark currents.[45-50] Therefore, to optimize MCT heterostructures for improved detector performance, detailed nanometer-scale characterization of both the interface structure, and the local band-offsets is necessary.

To explore the nanometer-scale interface structure and local band offsets in MBE-grown MCT heterostructures using XSTM and STS, it is essential to (i) be able to obtain a flat cleave and (ii) measure a tunneling current. Thus, it is essential to (i) grow the epitaxial layers on substrates that produce an atomically flat surface upon cleaving, and (ii) ensure that the substrates have a sufficiently high conductivity (low resistivity).

Therefore, in this dissertation, investigations of the influence of substrate orientation and thickness on the cleavage of CdTe and $Cd_{1-x}Zn_xTe$ substrates are presented, as well as the influence of indium (In) doping and annealing on the substrate resistivity. In addition, we designed a heterostructure to enable the nanometer-scale examination of $Hg_{-x}Cd_xTe$ films sensitive to mid-to-long wavelength infrared radiation.

1.4 Structural and Electronic Properties of Quantum Dot Heterostructures

Quantum dots are nanostructures with dimensions on the order of the carrier de Broglie wavelength. Fig. 1.1 shows the energy dependence of the ideal electronic density of states (DOS) for a free electron gas (left), an electron confined in one dimension, as in a quantum well (middle), and an electron confined in three dimensions, as in a quantum dot (right).[82] The DOS for a material represents the number of states that are available to be occupied by a charge carrier at each energy level. Ideally, the energy dependence of the DOS is continuous for the free electron, step-function like for wells, and delta-function like for dots. In real systems, however, broadening of the electronic states due to dot size variations and finite temperatures occurs, and as a result, the DOS has been predicted to be broadened in comparison with the idealized plot in Fig. 1.1(right).[70-72,83,84] To date, low temperature STS has apparently been used to quantify the DOS for colloidal PbSe[85] dots and to measure the confined state energies for colloidal InAs dots.[33] However, to our knowledge, low temperature STS has not been performed on epitaxially-grown InAs/GaAs dots. As will be discussed in Section 2.4 of this dissertation, the measured STS spectra are proportional to the sample DOS. In the long term, STS spectra could be used to *directly* measure the DOS of individual dots.

Strain-induced self-assembled InAs/GaAs quantum dots have enabled enormous advances in a variety of optoelectronic devices such as light-emitters and detectors.[19-26] Further advances will require an improved understanding and control of dot size, density, and shape, and their influence on the dot electronic states. The structure of InAs/GaAs dots has been reported to be influenced by a variety of growth parameters including substrate temperature, III/V flux ratio, growth rate, and the presence of alloy buffer and/or capping layers.[1-17] For example, it has been reported that InAs/GaAs dots grown on InGaAs buffers have higher densities than those grown directly on GaAs.[1-3] However, there have been conflicting reports on the effect of alloy buffers on dot size. In addition, growth of InAs/GaAs dots with InGaAs in lieu of GaAs capping layers apparently minimizes the tendency for the reduction in dot height upon capping, often termed dot "collapse",[4-6] but the influence of alloy capping layers has primarily been investigated qualitatively using plan-view STM or AFM. Thus, the effects of alloy buffer and capping layers on the dot sizes and wetting layer (WL) thickness remain unknown.

In this dissertation, the influence of $In_{0.2}Ga_{0.8}As$ alloy layers on the diameter, height, shape, and density of InAs dots, as well as the thickness of the surrounding wetting layers (WLs) has been investigated. Large scale and high resolution XSTM images reveal larger dimensions, density, and WL thicknesses for the dots with alloy buffer and capping layers (termed alloy quantum dots or "AQDs") in comparison with the quantum dots (QDs) without surrounding alloy layers. A strain-based mechanism for dot formation and collapse in the absence and presence of alloy layers is proposed to explain the findings. This mechanism is likely to be applicable to a wide range of similarly lattice-mismatched thin-film systems.

A number of reports have suggested that QDs often have non-uniform compositions across their width[54,55] and height[15,27,28,54-57] due to indium (In) segregation and interdiffusion at the interface between the GaAs and InAs layers. These reports suggest that the lateral [In] is highest at the QD core and that the vertical [In] increases in the growth direction. The WLs between the QDs contain sparse concentrations of individual In atoms which have not agglomerated to form a three-dimensional island.[58] The WLs are typically two-dimensional inhomogeneous films with significant [In] gradients, including vertical In segregation and lateral In clustering.[57-63] To date, the effect of these compositional variations on the QD and WL electronic states remains unknown. Although one cross-sectional STS study of molecular beam epitaxially grown QDs revealed a variation in QD effective bandgap in the growth direction,[27] any corresponding lateral variation in the effective bandgap was not considered. Thus, the origins of the effective bandgap variations have not been identified.

In this dissertation, the influence of variations in dot shape, strain, and composition on the electronic states was examined. Using variable separation STS, the nanometer-scale variations in the effective bandgap, the energy difference between the lowest confined electron (E_e) and hole (E_h) energies, within individual dots and the surrounding WL was measured. The trends in the measured effective bandgap variation were compared to trends predicted for effective bandgap variation due to shape, strain, and [In] variations. The data reveals variations in the effective band gap across individual QDs both laterally and in the growth direction. Laterally, the effective bandgap decreases toward the QD core and vertically, the effective bandgap decreases in the growth direction. These results are consistent with an increase in [In] toward the center and top of the QD, suggesting that [In] variations dominate the variations in QD effective bandgap.

1.5 Dissertation Organization

This dissertation is organized as follows. In Chapter 2, the experimental procedures used for the fabrication and characterization of the II-VI substrates and III-V quantum dot heterostructures are described. Details about crystal growth by the Bridgman technique as well as thin film growth via molecular beam epitaxy (MBE) and migration enhanced epitaxy (MEE) are provided. XSTM and variable separation STS are also described in detail.

In Chapter 3, the design of an appropriate conductive substrate upon which a MCT heterostructure would subsequently be grown is described. The goal was to identify $Cd_{1-x}Zn_xTe$ and/or CdTe crystals that (i) produced an atomically flat surface upon cleaving and (ii) exhibited sufficient conductivity to measure a tunneling current with our STM. Thus, the influence of substrate orientation, thickness, doping, and annealing on the substrate cleavage and resistivity was explored. Flat cleaves of the (110) surface were obtained for ~ 900 μm thick (111)-oriented CdTe and $Cd_{1-x}Zn_xTe$ wafers. Furthermore, using both In-doping and post-growth annealing in a Cd-rich environment,[86-88] the CdTe substrate resistivity was reduced to 0.04 Ω-cm, and subsequent XSTM and STS measurements were performed. A sample structure was designed to enable the nanometer-scale examination of $Hg_{-x}Cd_xTe$ films sensitive to both mid-to-long wavelength infrared radiation.

Chapter 4 presents investigations of the influence of InGaAs alloy buffer and capping layers on the size, shape, and density of InAs/GaAs dots and corresponding WLs. Large-scale and high-resolution XSTM images reveal larger dimensions, density, and WL thicknesses for the AQDs in comparison with the QDs. Taking into account the reduction in misfit strain provided by the InGaAs alloy layers at the buffer/dot and dot/cap interfaces, we propose a strain-based mechanism for dot formation and collapse in the absence and presence of InGaAs alloy layers. This mechanism is likely to be applicable to a wide range of lattice-mismatched thin-film systems.

In Chapter 5, we report on the origins of the effective bandgap variations in individual, uncoupled QDs and the surrounding WL. Using a combination of XSTM and STS, we find decreases in the effective bandgap both laterally, towards the QD core, and vertically, in the growth direction. These trends are consistent with an increase in [In] toward the center and top of the QD. Similarly, in the clustered regions of the WL, the effective bandgap variations are dominated by variations in the [In]. Finally, a summary and suggestions for future work are presented in Chapter 6.

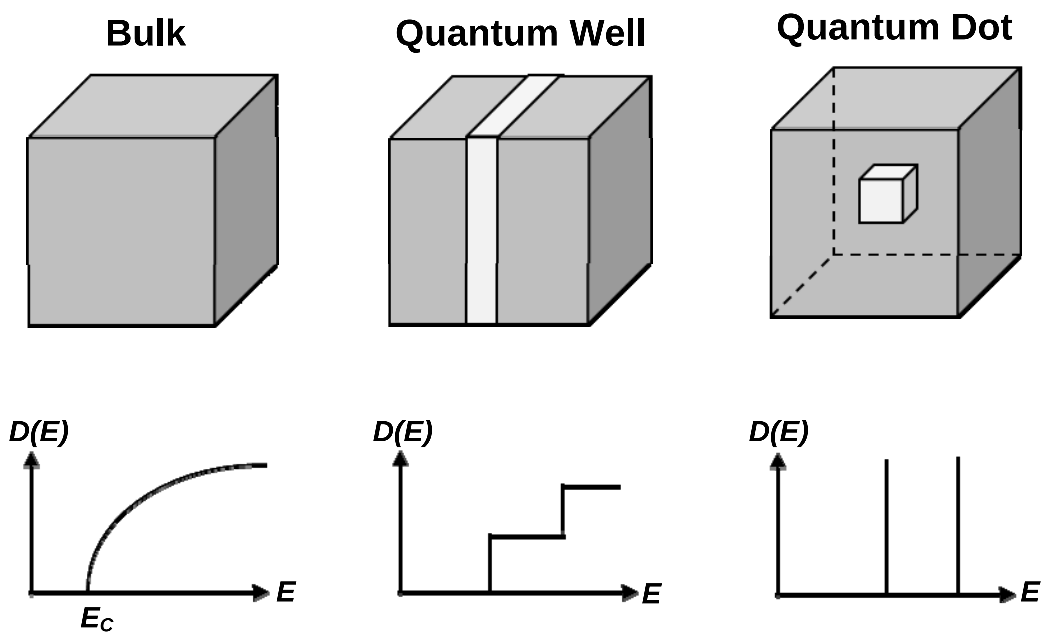

Fig. 1.1: Energy dependence of the density of states for an ideal free electron gas (left), an electron free in 2 directions but constrained in 1 direction (middle) and an electron constrained in 3 directions (right). For an unconstrained electron, the density of states has a parabolic dependence on energy. For an electron constrained in one direction, the density of states has a step function-like dependence on energy. For an electron confined in three directions, such as in a quantum dot, the density of states function has a delta function-like dependence on energy.

1.6 References

[1] H. Y. Liu, M. Hopkinson, C. N. Harrison, M. J. Steer, R. Frith, I. R. Sellers, D. J. Mowbray, and M. S. Skolnick, Journal of Applied Physics **93**, 2931 (2003).

[2] A. Stintz, G. T. Liu, A. L. Gray, R. Spillers, S. M. Delgado, and K. J. Malloy, Journal of Vacuum Science & Technology B **18**, 1496 (2000).

[3] J.-I. Chyi, T.-E. Nee, C.-T. Lee, J.-L. Shieh, and J.-W. Pan, Journal of Crystal Growth **175-176**, 777 (1997).

[4] R. Songmuang, S. Kiravittaya, and O. G. Schmidt, Journal of Crystal Growth **249**, 416 (2003).

[5] G. Costantini, A. Rastelli, C. Manzano, P. Acosta-Diaz, R. Songmuang, G. Katsaros, O. Schmidt, and K. Kern, Physical Review Letters **96** (2006).

[6] J. M. Ulloa, C. Celebi, P. M. Koenraad, A. Simon, E. Gapihan, A. Letoublon, N. Bertru, I. Drouzas, D. J. Mowbray, M. J. Steer, and M. Hopkinson, Journal of Applied Physics **101**, 081707 (2007).

[7] Y. Horikoshi, M. Kawashima, and H. Yamaguchi, Japanese Journal of Applied Physics **25**, L868 (1986).

[8] G. M. Guryanov, G. E. Cirlin, V. N. Petrov, N. K. Polyakov, A. O. Golubok, S. Y. Tipissev, V. B. Gubanov, Y. B. Samsonenko, N. N. Ledentsov, V. A. Shchukin, M. Grundmann, D. Bimberg, and Z. I. Alferov, Surface Science **352-354**, 651 (1996).

[9] G. E. Cirlin, V. N. Petrov, V. G. Dubrovskii, A. O. Golubok, S. Y. Tipissev, G. M. Guryanov, M. V. Maximov, N. N. Ledentsov, and D. Bimberg, Czechoslovak Journal of Physics **47**, 379 (1997).

[10] A. Bosacchi, P. Frigeri, S. Franchi, P. Allegri, and V. Avanzini, Journal of Crystal Growth **175-176**, 771 (1997).

[11] W. Cheng, Z. Zhong, Y. Wu, Q. Huang, and J. Zhou, Journal of Crystal Growth **183**, 279 (1998).

[12] Y. Horikoshi, Journal of Crystal Growth **201-202**, 150 (1999).

[13] J. D. Song, Y. M. Park, J. C. Shin, J. G. Lim, Y. J. Park, W. J. Choi, I. K. Han, J. I. Lee, H. S. Kim, and C. G. Park, Journal of Applied Physics **96**, 4122 (2004).

[14] T. Haga, M. Kataoka, N. Matsumura, S. Muto, Y. Nakata, and N. Yokoyama, Japanese Journal of Applied Physics **36**, L1113 (1997).

[15]P. B. Joyce, T. J. Krzyzewski, G. R. Bell, B. A. Joyce, and T. S. Jones, Physical Review B **58**, R15981 (1998).

[16]A. Rosenauer, D. Gerthsen, D. V. Dyck, M. Arzberger, G. Böhm, and G. Abstreiter, Physical Review B **64**, 245334 (2001).

[17]C. Heyn and W. Hansen, Journal of Crystal Growth **251**, 140 (2003).

[18]D. Loss and D. P. DiVincenzo, Physical Review A **57**, 120 (1998).

[19]E. Biolatti, R. C. Iotti, P. Zanardi, and F. Rossi, Physical Review Letters **85**, 5647 (2000).

[20]G. Yusa and H. Sakaki, Applied Physics Letters **70**, 345 (1997).

[21]J. O. Winter, T. Y. Liu, B. A. Korgel, and C. E. Schmidt, Advanced Materials **13**, 1673 (2001).

[22]I. R. Sellers, H. Y. Liu, K. M. Groom, D. T. Childs, D. Robbins, T. J. Badcock, M. Hopkinson, D. J. Mowbray, and M. S. Skolnick, Electronics Letters **40**, 1412 (2004).

[23]H. C. Yu, J. S. Wang, Y. K. Su, S. J. Chang, F. I. Lai, Y. H. Chang, H. C. Kuo, C. P. Sung, H. P. D. Yang, K. F. Lin, J. M. Wang, J. Y. Chi, R. S. Hsiao, and S. Mikhrin, IEEE Photonics Technology Letters **18**, 418 (2006).

[24]A. D. Stiff, S. Krishna, P. Bhattacharya, and S. Kennerly, Applied Physics Letters **79**, 421 (2001).

[25]J. Phillips, P. Bhattacharya, S. W. Kennerly, D. W. Beekman, and M. Dutta, IEEE Journal of Quantum Electonics **35**, 936 (1999).

[26]J. D. Phillips, K. Kamath, and P. K. Bhattacharya, Applied Physics Letters **73**, 1937 (1998).

[27]D. M. Bruls, J. W. A. M. Vugs, P. M. Koenraad, M. S. Skolnick, M. Hopkinson, and J. H. Wolter, Applied Physics A **72**, S205 (2001).

[28]A. Urbieta, B. Grandidier, J. P. Nys, D. Deresmes, D. Stievenard, A. Lemaitre, G. Patriarche, and Y. M. Niquet, Physical Review B **77**, 155313 (2008).

[29]T. Yamauchi, Y. Ohyama, Y. Matsuba, M. Tabuchi, and A. Nakamura, Applied Physics Letters **79**, 2465 (2001).

[30]T. Maltezopoulos, A. Bolz, C. Meyer, C. Heyn, W. Hansen, M. Morgenstern, and R. Wiesendanger, Physical Review Letters **91**, 196804 (2003).

[31]T. K. Johal, R. Rinaldi, A. Passaseo, R. Cingolani, A. Vasanelli, R. Ferreira, and G. Bastard, Physical Review B **66** (2002).

[32]B. Legrand, B. Grandidier, J. P. Nys, D. Stievenard, J. M. Gerard, and V. Thierry-Mieg, Applied Physics Letters **73**, 96 (1998).

[33]O. Millo, D. Katz, Y. W. Cao, and U. Banin, Physical Review B **61**, 16773 (2000).

[34]H. Jiang and J. Singh, Physical Review B **56**, 4696 (1997).

[35]H. Shin, Y. H. Yoo, and W. Lee, Journal of Physics D **36**, 2612 (2003).

[36]L. He, G. Bester, and A. Zunger, Physical Review B **70**, 235316 (2004).

[37]H. Shin, E. Yoon, Y. H. Yoo, and W. Lee, Journal of the Physical Society of Japan **73**, 3378 (2004).

[38]W. D. Lawson, S. Nielsen, E. H. Putley, and A. S. Young, Journal of Physics and Chemistry of Solids **9**, 325 (1959).

[39]P. Piotrowski, Infrared Physics & Technology **38**, 63 (1997).

[40]P. R. Norton, Proceedings of the SPIE **3379**, 102 (1998).

[41]J. Bajaj, Proceedings of the SPIE **3948**, 42 (2000).

[42]A. Rogalski, Progress in Quantum Electronics **27**, 151 (2003).

[43]A. Rogalski, Reports on Progress in Physics **68**, 2267 (2005).

[44]R. Breiter, W. Cabanski, K.-H. Mauk, W. Rode, and J. Ziegler, Proceedings of the SPIE **4369**, 579 (2001).

[45]X. Z. Liao and T. S. Shi, Applied Physics Letters **66**, 2089 (1995).

[46]M. W. Muller and A. Sher, Applied Physics Letters **74**, 2343 (1999).

[47]N. Mainzer and E. Zolotoyabko, Diffusion and Defect Data A **183**, 103 (2000).

[48]V. Gopal, S. K. Singh, and R. M. Mehra, Infrared Physics & Technology **43**, 317 (2002).

[49]J. D. Phillips, K. Moazzami, J. Kim, D. D. Edwall, D. L. Lee, and J. M. Arias, Applied Physics Letters **83**, 3701 (2003).

[50]T. Aoki, Y. Chang, G. Badano, J. Zhao, C. Grein, S. Sivananthan, and D. J. Smith, Journal of Crystal Growth **265**, 224 (2004).

[51]J. R. Yang, X. L. Cao, Y. F. Wei, and L. He, Journal of Electronic Materials **37**, 1241 (2008).

[52]Y. Chang, C. R. Becker, C. H. Grein, J. Zhao, C. Fulk, T. Casselman, R. Kiran, X. J. Wang, E. Robinson, S. Y. An, S. Mallick, S. Sivananthan, T. Aoki, C. Z. Wang, D. J. Smith, S. Velicu, J. Zhao, J. Crocco, Y. Chen, G. Brill, P. S. Wijewarnasuriya, N. Dhar, R. Sporken, and V. Nathan, Journal of Electronic Materials **37**, 1171 (2008).

[53]M. Reddy, J. Peterson, S. Johnson, T. Vang, J. Franklin, E. Patten, W. Radford, J. Bangs, and D. Lofgreen, Journal of Electronic Materials **38**, 1764 (2009).

[54]N. Liu, J. Tersoff, O. Baklenov, A. L. Holmes, Jr, and C. K. Shih, Physical Review Letters **84**, 334 (2000).

[55]A. Lenz, R. Timm, H. Eisele, C. Hennig, S. K. Becker, R. L. Sellin, U. W. Pohl, D. Bimberg, and M. Dahne, Applied Physics Letters **81**, 5150 (2002).

[56]A. Lemaitre, G. Patriarche, and F. Glas, Applied Physics Letters **85**, 3717 (2004).

[57]P. Wang, A. L. Bleloch, M. Falke, P. J. Goodhew, J. Ng, and M. Missous, Applied Physics Letters **89**, 072111 (2006).

[58]T. R. Ramachandran, A. Madhukar, I. Mukhametzhanov, R. Heitz, A. Kalburge, Q. Xie, and P. Chen, Journal of Vacuum Science & Technology B **16**, 1330 (1998).

[59]B. Lita, R. S. Goldman, J. D. Phillips, and P. K. Bhattacharya, Applied Physics Letters **75**, 2797 (1999).

[60]B. Lita, R. S. Goldman, J. D. Phillips, and P. K. Bhattacharya, Surface Review Letters **7**, 539 (2000).

[61]B. Shin, B. Lita, R. S. Goldman, J. D. Phillips, and P. K. Bhattacharya, Applied Physics Letters **81**, 1423 (2002).

[62]P. Offermans, P. M. Koenraad, R. Notzel, J. H. Wolter, and K. Pierz, Applied Physics Letters **87**, 111903 (2005).

[63]G. Sek, K. Ryczko, M. Motyka, J. Andrzejewski, K. Wysocka, J. Misiewicz, L. H. Li, A. Fiore, and G. Patriarche, Journal of Applied Physics **101**, 63539 (2007).

[64]A. Ourmazd, F. H. Baumann, M. Bode, and Y. Kim, Ultramicroscopy **34**, 237 (1990).

[65]D. Reuter, R. Roescu, M. Mehta, M. Richter, and A. D. Wieck, Physica E **40**, 1961 (2008).

[66]K. H. Schmidt, G. Medeiros-Ribeiro, M. Oestreich, P. M. Petroff, and G. H. Döhler, Physical Review B **54**, 11346 (1996).

[67]P. N. Brounkov, A. Polimeni, S. T. Stoddart, M. Henini, L. Eaves, P. C. Main, A. R. Kovsh, Y. G. Musikhin, and S. G. Konnikov, Applied Physics Letters **73**, 1092 (1998).

[68]G. Medeiros-Ribeiro, D. Leonard, and P. M. Petroff, Applied Physics Letters **66**, 1767 (1995).

[69]P. Blood, Semiconductor Science and Technology **1**, 7 (1986).

[70]M. Arzberger and M. C. Amann, Physica Status Solidi B **224**, 655 (2001).

[71]V. M. Apalkov, T. Chakraborty, N. Ulbrich, D. Schuh, J. Bauer, and G. Abstreiter, Physica E **24**, 272 (2004).

[72]M. Bayer and A. Forchel, Physical Review B **65** (2002).

[73]D. J. Mowbray and M. S. Skolnick, Journal of Physics D **38**, 2059 (2005).

[74]A. Kaneta, T. Izumi, K. Okamoto, Y. Kawakami, S. Fujita, Y. Narita, T. Inoue, and T. Mukai, Japanese Journal of Applied Physics **40**, 110 (2001).

[75]T. H. Gfroerer, in *Encyclopedia of Analytical Chemistry* (John Wiley & Sons Ltd, 2000), pp. 9209.

[76]R. S. Goldman, Journal of Physics D **37**, 163 (2004).

[77]R. M. Feenstra, Semiconductor Science and Technology **9**, 2157 (1994).

[78]O. Albrektsen, Ph.D. Thesis, Technical University of Denmark, 1990.

[79]B. Lita, Ph.D. Thesis, University of Michigan, 2001.

[80]R. J. Hamers, Annual Review of Physical Chemistry **40**, 531 (1989).

[81]T. Tsuruoka and S. Ushioda, Journal of Electron Microscopy **53**, 169 (2004).

[82]D. Bimberg, M. Grundmann, and N. N. Ledenstov, *Quantum Dot Heterostructures*. (John Wiley & Sons Ltd, West Sussex, 2001).

[83]R. Berkovits, Physical Review B **51**, 4653 (1995).

[84]B. Kramer and A. MacKinnon, Reports on Progress in Physics **56**, 1469 (1993).

[85]P. Liljeroth, P. A. Z. van Emmichoven, S. G. Hickey, H. Weller, B. Grandidier, G. Allan, and D. Vanmaekelbergh, Physical Review Letters **95**, 086801 (2005).

[86]Q. Li, W. Jie, L. Fu, G. Yang, G. Zha, T. Wang, and D. Zeng, Journal of Applied Physics **100**, 013518 (2006).

[87]V. Lyahovitskaya, L. Kaplan, J. Goswami, and D. Cahen, Journal of Crystal Growth **197**, 106 (1999).

[88] V. Lyahovitskaya, L. Chernyak, J. Greenberg, L. Kaplan, and D. Cahen, Journal of Crystal Growth **214-215**, 1155 (2000).

Chapter 2

Experimental Procedures

2.1 Overview

This chapter describes the experimental procedures used for the fabrication and characterization of the II-VI substrates and III-V heterostructures examined in this thesis. The $Cd_{0.96}Zn_{0.4}Te$ and CdTe substrates were grown by the Bridgman technique. The InAs/GaAs quantum dot heterostructures were fabricated via a combination of molecular beam epitaxy (MBE) and migration enhanced epitaxy (MEE). Ultra high vacuum (UHV) cross-sectional scanning tunneling microscopy (XSTM) was used to examine the atomic-to-nanometer scale structure of the II-VI substrates and III-V heterostructures. The effective bandgaps and confined state energies were measured by variable separation scanning tunneling spectroscopy (STS). Both techniques are described in more detail in this chapter. All procedures were carried out by the author except where noted in the text.

2.2 Substrate and Thin Film Growth

This section introduces substrate growth by the Bridgman technique and thin film growth by MBE and MEE.

2.2.1 Bridgman technique

The $Cd_{0.96}Zn_{0.4}Te$ and CdTe substrates were grown by Dr. M. Chu (of Fermionics) using the Bridgman technique. For crystal growth by the Bridgman technique, a seed crystal is placed in a quartz boat inside a sealed tube along with source materials (in this case Cd, Zn and Te).[1] The source material is heated above the melting point and then slowly cooled starting from the location of the seed crystal, producing a single-crystalline substrate. For the II-VI substrates discussed in this thesis, our goal was to increase their electrical conductivity to enable XSTM studies. Therefore, upon our suggestion, additional doping and annealing steps were also performed following crystal growth. These doping and annealing steps are described in more detail in Chapter 3.

2.2.2 Molecular Beam Epitaxy

Molecular Beam Epitaxy (MBE) involves the use of molecular beams to produce high quality epitaxial films.[2] MBE involves the sublimation or evaporation of solid or liquid sources, followed by the reaction and condensation of the constituent atoms or molecules on the surface.[3] Shutters in front of the effusion cells containing the sources are opened and closed during growth to control which constituent atoms or molecules are available for condensation on the substrate surface. Typically, the shutters for both the cation and anion atomic species are opened simultaneously, but the growth is limited by the cation flux. For example, during the growth of GaAs, the shutters for the Ga and As effusion cells are typically open simultaneously, and the growth rate is determined by the Ga flux. The Ga and As react to form GaAs islands on the surface, which once formed, are immobile due to the stable Ga-As bond.[4-6] Coalescence of the islands leads to the formation of a monolayer (ML) of GaAs. Thus, the surface roughness is dependent on the equilibrium between island formation and “smoothing” due to adatom migration.[7] At high growth temperatures, a higher As flux is needed to prevent As evaporation from the island periphery. Therefore, for a fixed As flux, it is possible to increase the Ga surface diffusion length by raising the substrate temperature.[8-10]

2.2.3 Migration Enhanced Epitaxy

An alternate method to significantly increase the group III diffusion length is to open the group III and group V shutters alternately instead of simultaneously. This alternate deposition of constituent atoms is often termed migration enhanced epitaxy (MEE). For example, for the MEE growth of 1 ML GaAs, each of the Ga and As shutters are alternately opened while the other remains closed. Thus, 1 ML of Ga is initially deposited, and when the As shutter is opened, 1 ML of GaAs is formed. During the “Ga shutter open” step, the cation diffusion length is significantly increased, leading to a growth surface with fewer steps and kinks compared to MBE growth.[3,8,11] The InAs/GaAs quantum dot heterostructures discussed in this dissertation were grown by Dr. J. D. Song’s group at the Korea Institute of Science and Technology (KIST). Although most of the structure was grown by MBE, the InAs dots were fabricated via MEE.

For dot growth via MEE, the In and As were deposited alternately for 8s, followed by a 5s growth interruption in the absence of As to allow dot nucleation.[12] The beam equivalent pressures for In and As were ~ 10^{-8} Torr and ~ 10^{-7} Torr respectively. A total of 3ML InAs was deposited in this way. Additional details of the heterostructure growth procedures are discussed in Appendix A.

2.3 Cross-sectional Scanning Tunneling Microscopy (XSTM)

In this section, an overview of cross-sectional scanning tunneling microscopy (XSTM) is provided, followed by details of sample and tip preparation for XSTM experiments. The XSTM experiments discussed in the bulk of this dissertation were carried out using a Park Scientific Instruments Autoprobe VP STM. A comprehensive review of the XSTM system used in my studies has been discussed in Section 2.3 of the PhD thesis of Dr. B. Lita, and some details are repeated here for completeness.[13] Additional preliminary experiments, discussed in Chapter 6, were carried out in an Omicron VT-STM.

2.3.1 Overview

For XSTM, a cross-section of the sample under investigation is prepared by cleaving it in ultra-high vacuum (UHV), to expose an atomically flat surface. Constant-current STM is then performed on the exposed surface, as illustrated in Fig. 2.1.[14] When the cleaved surface is atomically flat, with monolayer steps spaced hundreds of nanometers apart, the apparent topographic contrast observed in constant current images is primarily due to variations in the electronic properties of the individual layers.[15]

An example of an XSTM topographic image is shown in Fig. 2.2(a). The bright and dark regions visible in the image correspond to layers of InAs and GaAs respectively. Fig. 2.2(b) and Fig. 2.2(c) show schematic energy band diagrams for empty state imaging of the InAs and GaAs, respectively. In both cases, the application of a positive sample bias voltage, V, results in electron tunneling from the STM tip into the empty conduction band states of the semiconductor. Since the bandgap of GaAs (Fig. 2.2(c)) is larger than the bandgap of InAs (Fig. 2.2 (b)), fewer states are available for the electrons to tunnel into the GaAs than into the InAs. Thus, the STM tip must move closer to (away from) the GaAs (InAs) surface to maintain a constant tunneling current. Therefore, the GaAs (InAs) layer appears darker (brighter) in the XSTM image.

The success of an XSTM experiment relies upon the achievement of a flat cleavage surface, the availability of a clean, sharp probe tip, and the availability of a sufficient tunneling current between the sample and tip. The probability of achieving an atomically flat cleave, or the cleavage success rate, typically depends on the sample thickness, length-to-width ratio, crystallographic orientation, and strain balancing within the heterostructure.[13] Following cleaving, the image quality depends on the radius of curvature and cleanliness of the STM tip. The STM tip can be cleaned by electron emission (as described in Section 2.3.4 of this dissertation) or by passing a high current through the tip, by alternating between applying a very high positive and negative voltage to the sample.

Generally, the availability of a sufficient tunneling current is determined by the STM electronics and the sample conductivity. On the PSI Autoprobe VP, after the STM tip approaches the sample, a pre-amplifier converts the measured tunneling current into a voltage signal at 0.1 V/nA, and voltages below 0.01 V are converted to 0.[16] Thus, it is necessary to ensure that the samples are conductive enough to produce a tunneling current greater than 0.1 nA. For the III-V samples, the resistivity was typically $< 10^{-3}$ Ω-cm, and sufficient sample-tip tunneling currents were typically achieved. For the II-VI samples, tunneling was achieved for samples with resistivities < 0.05 Ω-cm, although lower resistivities would be optimal to increase the sample-tip tunneling current. Additional details regarding the minimum resistivity to detect a tunneling current are provided in Chapter 3.

2.3.2 Sample Polishing

The III-V heterostructures of interest were typically grown on a quarter of 3" wafer with standard thicknesses ranging from 300 to 500 μm. Earlier XSTM studies of InAs dots on *n*+ and *p*+ GaAs showed highest cleavage success rate for the $(1\bar{1}0)$ and (110) surfaces, respectively. Thus, we first identified the [110] and $[1\bar{1}0]$ directions using anisotropic etching with HF/H_2O_2:1/4, as described in Section 2.3.4 of the Ph.D. thesis of Dr. B. Lita.[13,17,18] Following <110> direction identification, wafer pieces were thinned to approximately 180 μm by mechanical polishing from the backside, as follows. Wafer pieces of dimensions ~ 22 mm x 6 mm were cleaved from the sample of interest such that the long axis corresponded to the $[1\bar{1}0]$ direction. Each piece was thinned to

~ 250 μm using 600 grit SiC paper (average particle size ~ 15 μm), to ~ 220 μm using 800 grit SiC paper (average particle size ~ 12 μm), and to ~ 200 μm using 1000 grit SiC paper (average particle size ~ 7 μm). The final step consisted of polishing to ~180 μm using 1200 grit SiC paper (average particle size ~ 5 μm) to minimize surface scratches.

Thinning the II-VI substrates such as CdTe to a thickness of approximately 900 μm provided the best cleaves whereas further thinning did not result in flat cleaves. As shown in Table D.1 of Appendix D, CdTe is softer (microhardness = 47 kg/mm^2)[19] than III-V substrates such as GaAs (microhardness = 670 kg/mm^2).[20] The yield strength, which influences whether a sample would bend or cleave upon pressure, is proportional to the microhardness.[21] The lower microhardness for CdTe in comparison with that of GaAs likely contributed to the need for a thicker substrate to achieve flat cleaves.

2.3.3 Sample Scribing

Following polishing, the samples were cleaved into smaller rectangular pieces with typical widths of 1.5 – 2 mm and typical lengths of 12 – 22 mm. On each rectangular piece, a shallow scratch was hand-scribed along the width of the epilayer side of the sample, approximately 6 mm away from one end of the sample, as shown in Fig. 2.3. Previous members of our research group found that a sample length-to-width ratio of 10 or more was typically necessary to obtain flat cleavage surfaces in the vicinity of the epilayers.[13,22] For the experiments described in this dissertation, flat cleaves were obtained from the III-V and II-VI samples with length-to-width ratios of approximately 9 and 5 respectively. For the II-VI samples with aspect ratios larger than 5, the sample would bend and then break in the sample holder (instead of breaking along the scribe mark), thus producing fracture surfaces with significant topography. The differences in the optimum length-to-width ratios of the III-V and II-VI samples are likely due to the significant differences in their microhardness.

After scribing, the sample was then mounted in the sample holder with the epilayer side facing up and the scribed end resting directly on the back of the sample holder. Schematic photos are shown in Section 2.3.4 of the Ph.D. thesis of Dr. B. Lita.[13] Since pushing, bending, or twisting of the sample in the sample holder can greatly decrease the probability of obtaining a flat cleave, great care was taken in loading the sample into the sample holder. Once the sample was secured in the sample holder, the sample holder was loaded into the load lock of the Autoprobe VP, for subsequent transfer into the STM chamber the following day.

2.3.4 Tip Preparation

All the STM and STS experiments described in this dissertation were performed with commercially available Pt/Ir STM tips from Materials Analytical Systems. The tips were cleaned *in situ* by electron bombardment from a heated Mo filament.[13,23] The tip cleaning procedure is as follows. Using the tip transfer arm, the tip to be cleaned is brought within 3 – 5 mm of the filament. A current is passed through the filament using a Hewlett Packard 6286 A DC current source. A positive bias of 350 V is then applied to the tip relative to the Mo filament using a Bertran 230 Series high voltage power supply. This causes the emission of electrons from the filament, and these emitted electrons are accelerated towards the end of the positively biased tip. The resulting emission current is measured using a Fluke Series II Multimeter.

To clean the Pt/Ir tips, the Mo filament current is increased gradually to 1.5 – 2 A until an emission current of 1 mA is measured.[13] This emission current is held constant for 3 minutes, and is then reduced to zero to allow the chamber base pressure to recover. The procedure is then repeated 2 – 3 times, or until the chamber pressure does not exceed 1×10^{-9} Torr during cleaning. Since this procedure increases the STM chamber pressure, tips for an experiment are cleaned *in situ* at least 12 hours before an experiment, but no longer than 24 hours prior to an experiment, to prevent tip contamination in the meantime.

2.3.5 UHV Sample Preparation

After the sample has been loaded in the load-lock, there are several steps that are performed in UHV prior to collecting XSTM data. First, the sample is cleaved, and the cleavage surface is visually examined. Once it is confirmed that the surface does not display significant topography, the sample is lowered onto the STM stage. These steps are described in more detail below.

For an XSTM experiment, the sample under investigation is transferred from the load lock to the main STM chamber, where it is subsequently cleaved. The samples can be cleaved either using the cleaver or the tip transfer arm. Typically, the sample is cleaved using the cleaver, which is a 60° diamond tip attached to a VG XYZ manipulator.[13] Upon contact with the cleaver, the sample ideally falls straight down to the bottom of the STM chamber. If a sample is too short to be cleaved using the manipulator (sample length < 15 mm), then the tip transfer arm is used instead. Typically, the cleave success rate is highest for cleaving with the manipulator.

The cleaved (110) surface of most III-V semiconductor compounds does not reconstruct, and dangling bond states typically do not lie within the band gap.[23-25] It is therefore possible to obtain information about the bulk-like structure, chemistry, and electronic properties of the layers.[14] For the *n*+ III-V heterostructures in this dissertation, the (001) oriented samples were cleaved to expose a $(1\bar{1}0)$ surface upon cleaving, as shown in Fig. 2.3(a).[17,26,27] For the II-VI substrates, the substrates were cleaved to expose a (110) plane, as shown in Fig. 2.3(b) and 2.3(c) for (001) and (111) oriented substrates, respectively. Typically, flat (110) surfaces are more often formed via cleavage of (111) vs. (100) oriented substrates. Additional details of the cleaving attempts of II-VI substrates are discussed in Chapter 3.

Following cleaving, the surface is visually examined using a Spindler & Hoyer 1.2x reading telescope with a 240-300 mm auxiliary close-up lens, resulting in a total magnification of 21x. The surface features on the cleaved surface are noted in the lab notebook to keep track of the cleave success rate. Fig. 2.4 shows a diagram representing an ideal cleaved surface. Fracture lines are confined to the area directly below the scribe mark, and a flat area is present to the right of the fracture lines. If visual examination with the telescope reveals a flat area, then we would proceed with STM imaging of that cleaved surface. In that case, the sample is lowered onto the STM stage using the manipulator. A tip is transferred to the scanner head and the tip is moved toward the sample. The initial STM tip approach is performed as far away as possible from the rough regions, as indicated by the filled circles in Fig. 2.4. Next, the walk-off procedure is performed as described in Section 2.3.5 of Dr. B. Lita's Ph.D. Thesis.[13]

2.3.6 Heterostructure Design

In this section, heterostructure design strategies for optimizing the XSTM experiment success rate will be discussed. These include the design of a strain balanced structure, use of marker layers, and the use of high doping.

To increase the probability of obtaining an atomically flat cleave in the region of interest, the heterostructures are designed to be strain-balanced, with a typical cap layer thickness ≥ 300 nm. In addition, to enable the identification of a given region of the sample, marker layers are incorporated into the design. For the III-V heterostructures, AlAs/GaAs superlattices sandwiched between layers of GaAs provided electronic contrast with respect to the surrounding GaAs, thereby functioning as a marker layer. Similarly, superlattices of HgCdTe and CdTe would serve as markers for the II-VI heterostructures. The growth and sample structure details of the II-VI and III-V heterostructures can be found in Chapters 3 and 4 respectively.

To increase the sample-tip tunneling current and to reduce the effects of tip-induced band bending, which will discussed in more detail in section 2.5, high doping concentrations within the substrate and heterostructure layers are needed. Tip-induced band bending, which occurs when the applied voltage bias is dropped across both the vacuum gap and the semiconductor itself, can introduce shifts in the effective band edges.[24,28] For example, for GaAs, the expected shifts range from several tenths of an eV, for 1×10^{17} cm^{-3} to ~ 0.1 eV for > 1×10^{18} cm^{-3}.[29]

2.4 Variable-Separation Scanning Tunneling Spectroscopy (VS-STS)

For the research presented in this dissertation, we used variable-separation scanning tunneling spectroscopy (VS-STS), which is an adaptation of a tunneling experiment in superconductivity.[30] In the VS-STS method, both the bias voltage and tip-sample separation are varied in a controlled manner and the resulting tunneling current and differential conductance are measured. The feedback loop is deactivated, and a continuous linear voltage ramp is applied to the sample, while the tip height is varied in a controlled manner.[31] The tip is moved towards (away from) the surface as the magnitude of the bias voltage is decreased (increased). As a result, the measured tunneling current and differential conductance are increased in the vicinity of the band edges, enabling a more accurate determination of their energetic positions, in comparison to constant-separation STS. The main advantage of the variable-separation method is that the conductance and current at low voltages are amplified while the noise level remains constant. The dynamic range, i.e. the ratio of the largest to smallest detectable signal, increases by 2 – 3 orders of magnitude using this technique, making it possible to accurately identify the energetic positions of the band edges.[29] In this section, the measurement of the differential conductance using a lock-in amplifier, the experimental steps involved in a VS-STS measurement, and the analysis of the data are presented.

2.4.1 Differential Conductance

The differential conductance, *dI/dV*, is measured using a lock-in technique, as shown schematically in Fig. 2.7. The sample bias, $V_{bias}(t)$ is the sum of a voltage ramp, $V_{ramp}(t)$, which is applied to the sample via the STM interface module, and an AC signal, $V_{mod}\cos(\omega_{ref}t)$, which is applied by the lock-in amplifier.

$$V_{bias}(t) = V_{ramp}(t) + V_{\text{mod}} \cos(\omega_{ref} t) \tag{2.1}$$

where V_{mod} is the amplitude of the modulated signal sent to the sample from the lock-in amplifier, and ω_{ref} is the reference frequency. A modulation voltage with frequency of 900 Hz and amplitude of 33-50 mV was typically used in our experiments. A plot of the sample bias as a function of time is shown in Fig. 2.8. In Fig. 2.8, V_{min} is the minimum voltage applied the sample during the spectroscopy measurement (typically -2 V), V_{max} is the maximum voltage applied to the sample during the spectroscopy measurement (typically 2 V), and t_{ramp} is the time period over which the voltage is ramped (typically 0.5 s). The time dependent voltage ramp can be written as:

$$V_{ramp}(t) = V_{\min} + \Delta V_{ramp} \frac{t}{t_{ramp}} \tag{2.2}$$

where $\Delta V_{ramp} = V_{\max} - V_{\min}$ is the range of voltages applied to the sample. Equation 2.2 can be substituted into equation 2.1 to give:

$$V_{bias}(t) = \left(V_{\min} + \Delta V_{ramp} \frac{t}{t_{ramp}} \right) + V_{\mathrm{mod}} \cos(\omega_{ref} t) \tag{2.3}$$

The modulation in applied voltage produces a modulation in the measured tunneling current, $I[V(t)]$. The signal $I[V(t)]$ is measured directly and also sent to the lock in amplifier, which detects the magnitude of signals oscillating at ω_{ref}. Using a Taylor's series expansion, the measured current can be written as:

$$I[V(t)] = I[V_{ramp}(t)] + \frac{1}{1!}\frac{dI}{dV}\bigg|_{V=V_{ramp}(t)} (V - V_{ramp}(t)) + \frac{1}{2!}\frac{d^2I}{dV^2}\bigg|_{V=V_{ramp}(t)} (V - V_{ramp}(t))^2 \tag{2.4}$$

Using equation (2.1), the above equation becomes:

$$I[V(t)] = I[V_{ramp}(t)] + \frac{dI}{dV}\bigg|_{V=V_{ramp}(t)} (V_{\mathrm{mod}}(t)) + \frac{1}{2}\frac{d^2I}{dV^2}\bigg|_{V=V_{ramp}(t)} (V_{\mathrm{mod}}(t))^2 + \ldots \tag{2.5}$$

Since the frequency of the voltage modulation is known, we can use the lock-in amplifier to extract the differential conductance, $\frac{dI}{dV}\Big|_{V=V_{ramp}(t)}$.

2.4.2 Experimental Steps

The first step of VS-STS involves setting up the appropriate tip extension, *z(V)*, as shown in Fig. 2.5(a). Care must be taken to avoid damaging the tip and sample by extending the tip too much. Typically, the tip is moved 6-10 Å toward (away from) the sample while the applied bias voltage was increased from -2.5 to 0 V (increased from 0 V to 2.5 V). The precise parameters were optimized for each particular tip-sample combination. Prior to collecting STS spectra from a region of interest, calibration spectra on "known" regions, such as GaAs, were first collected. In a region of GaAs, the tip was sequentially moved closer to the sample in steps of 1 – 2 Å, until a reasonable bandgap (1.43 ± 0.5 eV) was measured for the known layers (usually GaAs), as shown in Fig. 2.6. If spectra from the "known" region did not reveal bandgaps close to what was expected for the "known" regions of the sample, spectra are not collected from the "unknown" regions (such as the InAs QDs).

The measured sample current as a function of voltage, *I(V)*, is plotted in Fig. 2.5(b). The measured current is positive (negative) for large positive (negative) voltage values, while the current is negligible for voltage values close to 0 V. This region of negligible current corresponds to the bandgap of the sample. Since there are few electronic states in the band gap, there is minimal tunneling to or from those states; therefore, the measured current and conductance within the bandgap are negligible.

The measured differential conductance, *dI/dV*, is plotted as a function of sample bias in Fig. 2.5(c). In the plot, there is a region of increased differential conductance for "large" negative voltage values, followed by a region of negligible conductance for low absolute voltages, and finally, another region of increased conductance for "large" positive voltage values. The boundaries of these regions correspond approximately to the valence (E_V) and conduction band edges (E_C) of the GaAs, respectively.

2.4.3 STS Analysis

In this section, the relationship between the measured differential conductance and the sample density of states, as well as the differential conductance normalization procedure, will be discussed. The total measured tunneling current is proportional to the probability of an electron tunneling from the tip (*t*) to the sample (*s*), $f(E_t)\left[1-f(E_s+eV)\right]$, the probability of an electron tunneling from the sample to the tip, $f(E_s+eV)\left[1-f(E_t)\right]$, and the modulus of the probability of electron transmission across the vacuum gap between the sample and tip, $|M_{st}|$.[31] If these probabilities are summed over all tip and sample states, then the equation for current can be written as:

$$I=\frac{2\pi e}{\hbar}\sum_{s,t}\left\{f(E_t)\left[1-f(E_s+eV)\right]-f(E_s+eV)\left[1-f(E_t)\right]\right\}\left|M_{st}\right|^2\delta\left(E_t-E_s\right) \tag{2.6}$$

where the subscript *t* represents tip states, the subscript *s* represents sample states, *eV* is the energy difference between the tip and sample Fermi levels, and M_{st} is the tunneling matrix element between the electron wave functions of the sample and tip. For finite voltages, the above equation can be re-written as an integral over the local density of states of the sample and tip:

$$I \approx \frac{2\pi e}{\hbar} \int_{0}^{eV} \rho_s(E)\rho_t(E-eV)\left|M_{st}\right|^2 dE \tag{2.7}$$

where ρ_s and ρ_t correspond to the local density of states of the sample and tip respectively. Assuming a metallic tip with an energy independent ρ_t, then $\rho_t = \rho_t(0)$, and can be taken out of the integral. Thus, the equation for current can be written as:

$$I \approx \frac{2\pi e}{\hbar} \rho_t(0) \int_{0}^{eV} \rho_s(E)\left|M_{st}\right|^2 dE \tag{2.8}$$

Dividing the differential conductance, *dI/dV*, by total conductance, *I/V*, will remove the transmission probability term, $\left|M_{st}\right|^2$, and the resulting ratio of the measured differential conductance to the total conductance, *dI/dV/(I/V),* has been attributed the local density of states of the sample.[32,33]. However, within the bandgap, the total conductance approaches zero, leading to a divergence in *dI/dV/(I/V)* near the band edges. To prevent this divergence, the total conductance is broadened by convoluting the measured *I/V* with an exponential function to yield $\overline{I/V}$, as described by Feenstra:[23]

$$\overline{I/V} = \frac{1}{2\Delta V} \int_{-\infty}^{\infty} \left[I(V')/V'\right] \exp\left\{\frac{-\left|V'-V\right|}{\Delta V}\right\} dV' \tag{2.9}$$

We note that the shape of the spectra and the position of the spectral features are typically not influenced by convoluting with an exponential function.

Following the collection of the current and conductance spectra, the conductance is normalized using the program AnalysiSTS, written by M. Beck in C++, based on the work of R. M. Feenstra.[29] The band edges are then identified on the normalized conductance plot. Additional details of this program, along with details on band edge identification, are provided in the Ph.D. Thesis of Dr. B. Lita.[13]

2.5 Tip Induced Band Bending

The high electric field between sample and tip in a typical STM measurement can shift the energy bands on the surface of the semiconductor relative to the bulk. This phenomenon is called tip induced band bending, and will be described in more detail in this section.

Electron tunneling between the tip and sample during a STM measurement was described in Section 2.3. In the PSI Autoprobe VP, a voltage bias is applied to the sample while the tip is grounded and, electrons tunnel from the tip to the sample, producing a tunneling current. Ideally, the applied voltage is dropped entirely across the vacuum barrier, as shown in Fig. 2.2(c). However, the applied voltage is often dropped partly across the vacuum and partly across the semiconductor sample, producing a depletion region within the semiconductor, as shown in Fig. 2.9(a). This is often termed "tip-induced band bending" or "dynamic band bending".[24,29,34,35]

In Fig. 2.9, the apparent band edges due to tip induced band bending are marked as 'E_C' and 'E_V' while the expected band edges are marked as E_C and E_V. Significant band bending can take place within the semiconductor when a voltage bias is applied, as shown in Fig. 2.9(b) and Fig. 2.9(c). When the applied bias is negative, the Fermi level of the tip is lower in energy than the Fermi level of the sample ($E_{Ft} < E_{Fs}$) and electrons tunnel from the valence band of the sample to the tip, as shown in Fig. 2.9(b). However, due to band bending, the apparent valence band edge, 'E_V' is lower than the expected band edge, E_V. Similarly, when the applied bias is positive, $E_{Ft} > E_{Fs}$ and electrons tunnel from the tip to the conduction band of the sample, as shown in Fig. 2.9(c). Due to band bending, the apparent conduction band edge, 'E_C', is higher than the expected band edge, E_C. During an STS measurement, the voltage is swept from negative to positive values; therefore, the apparent band gaps are shifted so that the measured band gap, 'E_C' – 'E_V' is larger than the expected band gap, $E_C – E_V$.

Electrostatic solutions to quantify the tip induced band bending have been proposed previously.[34-37] In addition, preliminary calculations of tip-induced band-bending using three-dimensional finite element analysis have been carried out recently by our collaborators, W. Morgan and Dr. H. T. Johnson from the University of Illinois at Urbana Champaign (UIUC). A commercially-available Poisson equation solver (COMSOL) has been used to simulate the potential drop from an idealized tip, across the gap, and into the dielectric substrate containing the cleaved quantum dot. The calculations reveal the strong sensitivity of the band-bending field to the tip-sample separation distance (ranging from ~ 0.5 eV at 3 nm to ~ 1 eV at 0.5 nm). Details of these calculations will be published elsewhere.[38,39]

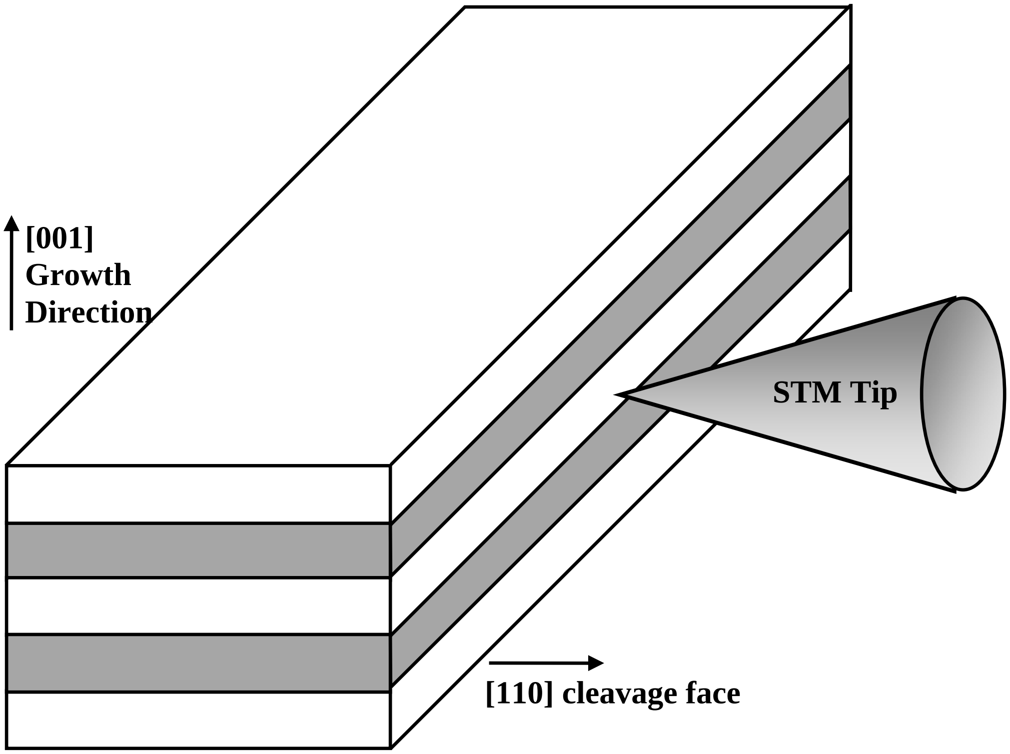

Fig. 2.1: Schematic of cross-sectional scanning tunneling microscopy applied to the III-V heterostructures investigated in this dissertation. The STM tip is brought within a few nanometers of the cleaved [110] face.[13]

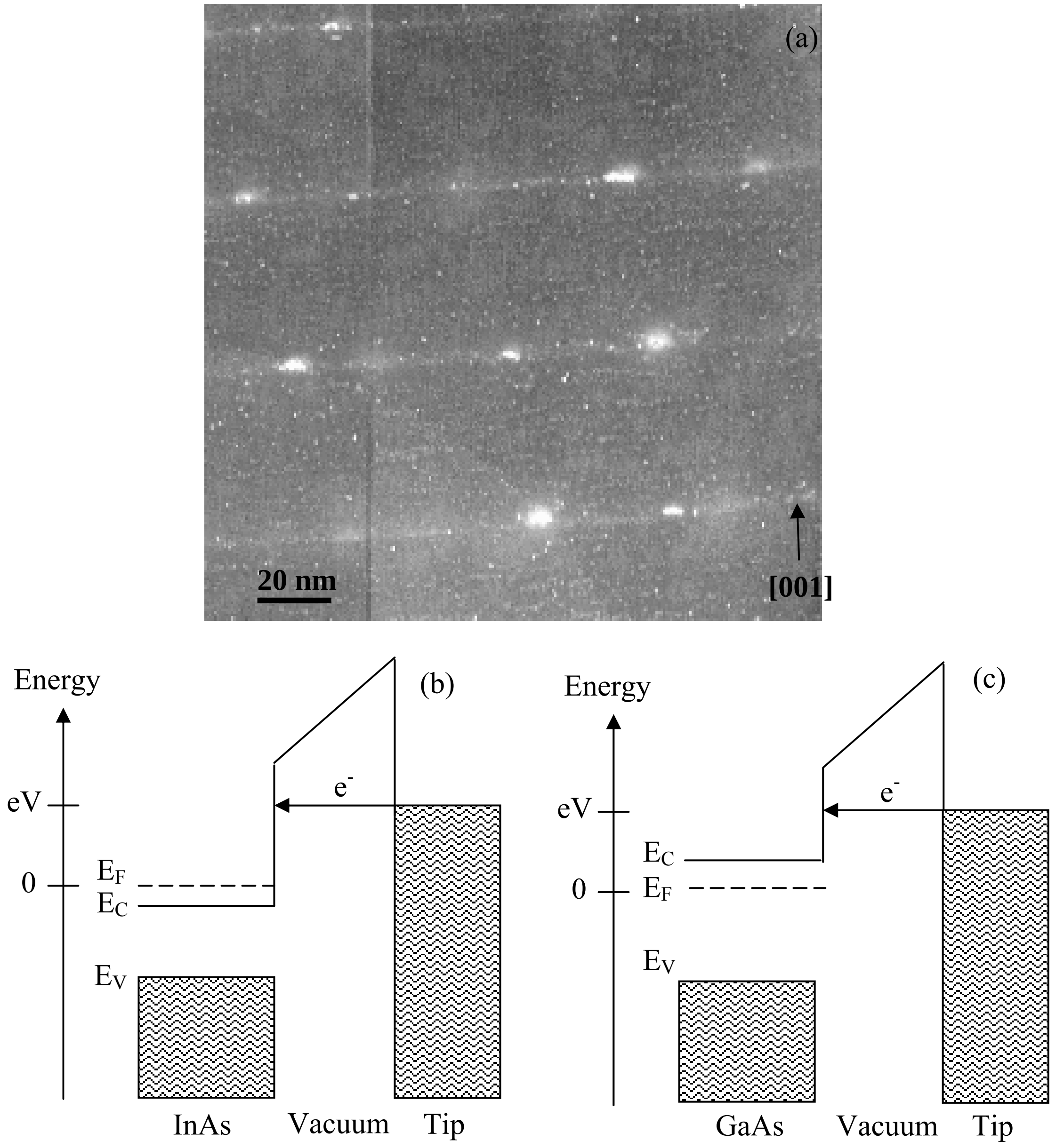

Fig. 2.2: (a) XSTM topographical image of InAs dots in a GaAs matrix. Schematics of the tunneling process between a tip and a sample under positive sample bias are shown below. The electrons tunnel from the tip into the energy levels above the Fermi level (E_F) of either (b) InAs or (c) GaAs. Since there are more states available to tunnel into in InAs than GaAs, the InAs layers will appear brighter in a constant-current STM image.

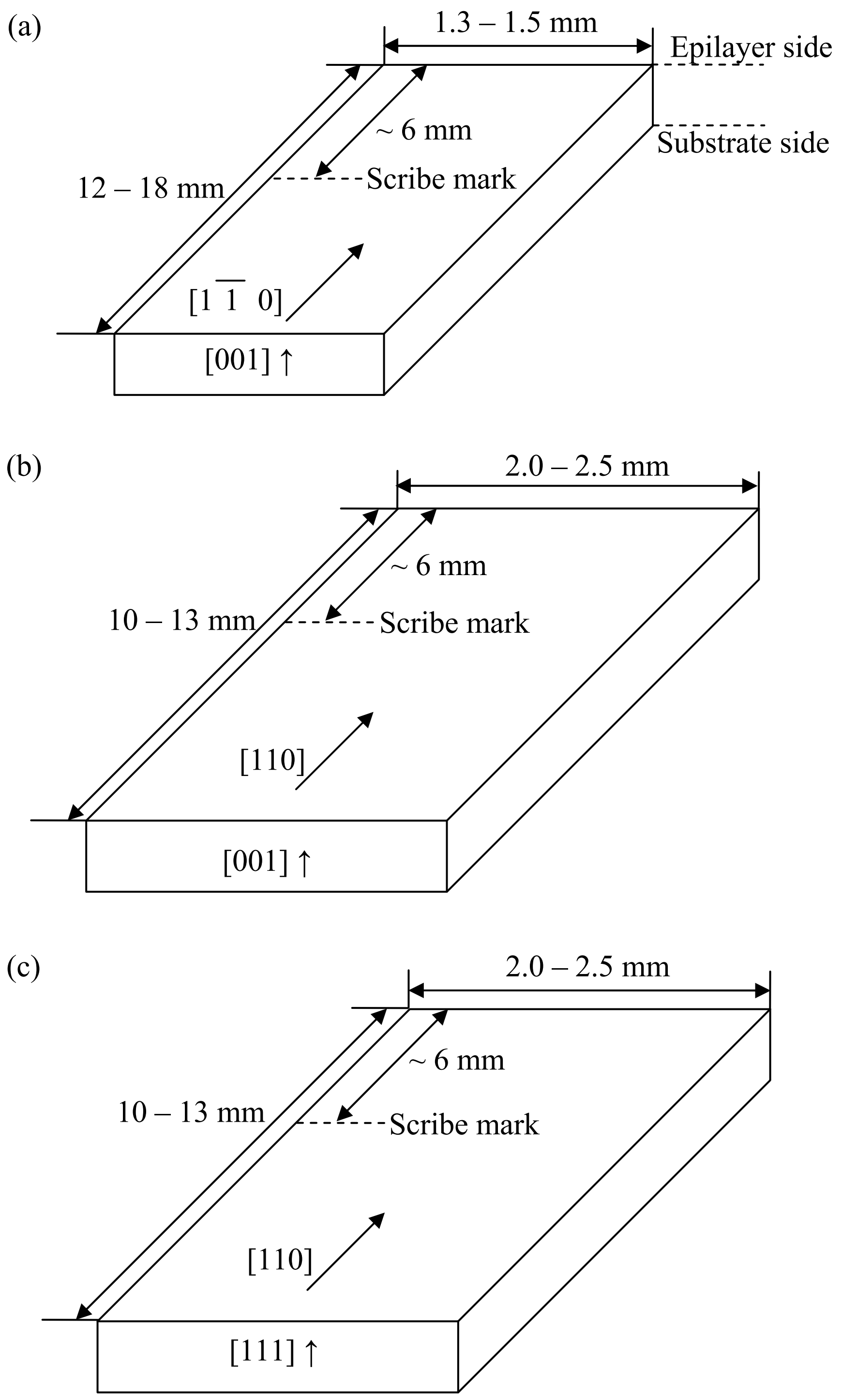

Fig. 2.1: Diagram showing the orientations of (a) the (001)-oriented III-V heterostructures and (b) the (001)-oriented CdZnTe substrates, and (c) the (111)-oriented CdTe and CdZnTe substrates. For both the II-VI and III-V structures examined in this dissertation, a shallow scratch or scribe mark is hand-scratched on the epi-layer side prior to mounting the sample onto the sample holder.

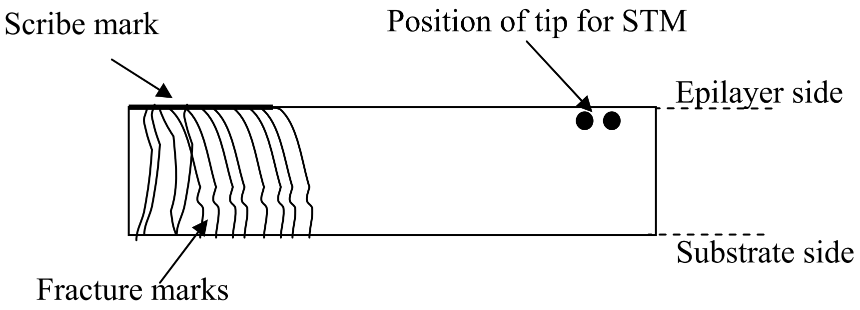

Fig. 2.4: Schematic of an ideal cleaved surface, as observed from the telescope. The area just underneath the scribe mark, shown towards the left, shows pronounced topography, while the rest of the exposed surface appears smooth. The tip is placed as far away from the rough regions as possible.

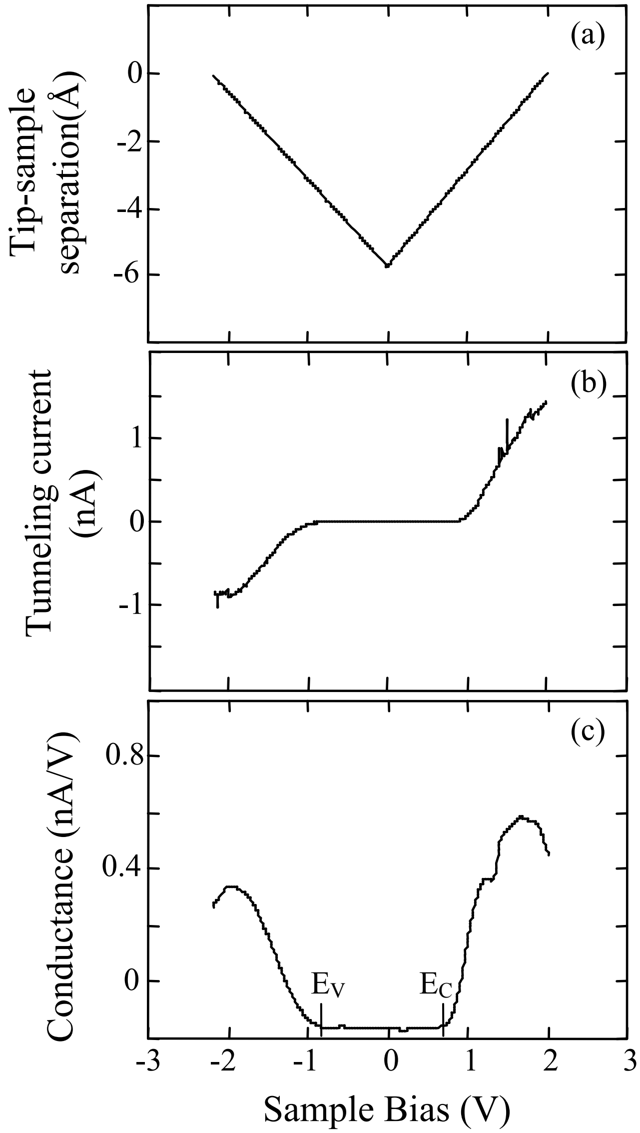

Fig. 2.5: Plots of measured (a) tip height, (b) tunneling current, and (c) differential conductance vs. sample bias voltage for GaAs using variable-separation scanning tunneling spectroscopy. For plot (c), the boundaries between regions of positive conductance and regions of negligible conductance correspond approximately to the valence and conduction band edges GaAs.[13] Note: Since the conductance data in (c) has not been normalized, the plot is slightly offset relative to 0.

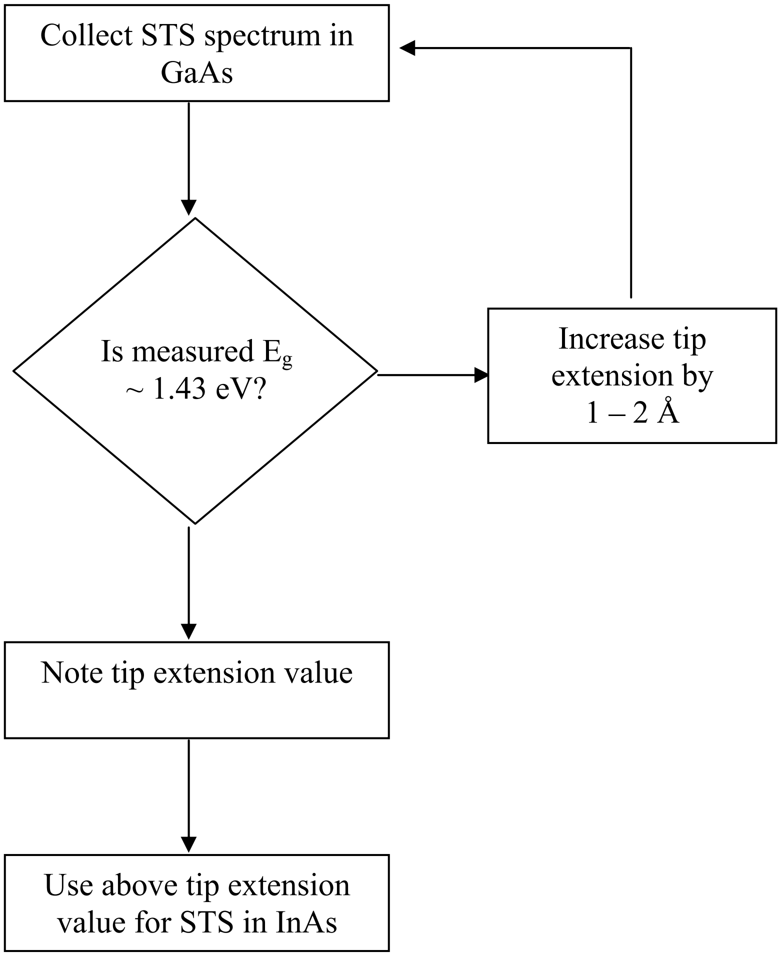

Fig. 2.6: Flowchart showing the process for optimizing the tip-sample separation for a variable-separation STS measurement. The tip extension is gradually increased in steps of 1 – 2 Å until a reasonable bandgap for GaAs is measured.

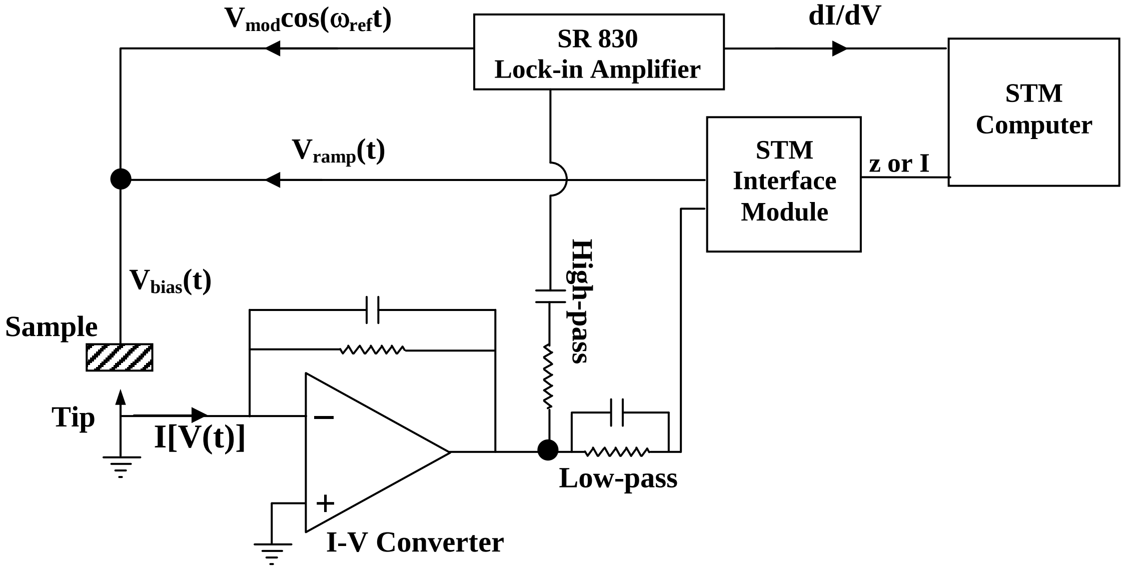

Fig. 2.7: Block diagram showing the set up for the lock-in amplification used for variable-separation scanning tunneling spectroscopy.[13] The sample is biased with respect to the grounded tip. A linear ramp, $V_{ramp}(t)$ is applied to the sample. An AC signal, $V_{mod}\cos(\omega_{ref}t)$, is added to the voltage ramp, and this signal is also used as a reference by the lock-in amplifier, to determine the differential conductance, dI/dV. The two voltage signals are added, producing a time varying bias voltage, $V_{bias}(t)$. The tunneling current, I, is converted to a voltage prior to being split and sent to both the lock-in amplifier and the STM interface module.

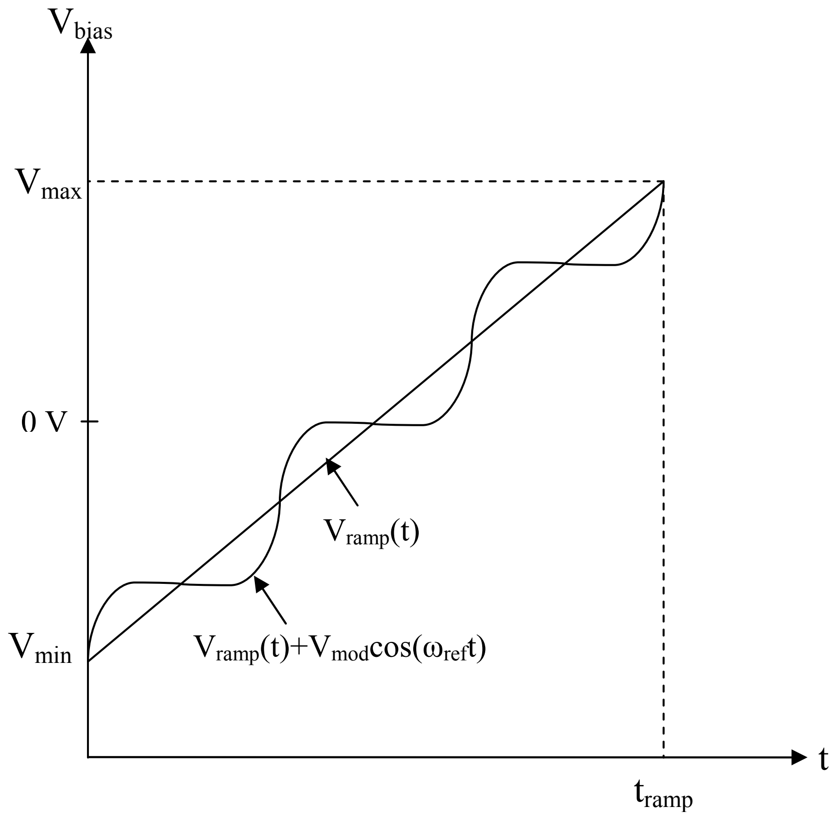

Fig. 2.8: Plot showing V_{bias}, the total applied bias, as a function of time, as the bias voltage is ramped from negative to positive values. A time-varying AC signal from the lock-in amplifier, $V_{mod}\cos(\omega_{ref}t)$, is superimposed on $V_{ramp}(t)$ such that the total sample bias, $V_{bias}(t) = V_{ramp}(t) + V_{mod}\cos(\omega_{ref}t)$.

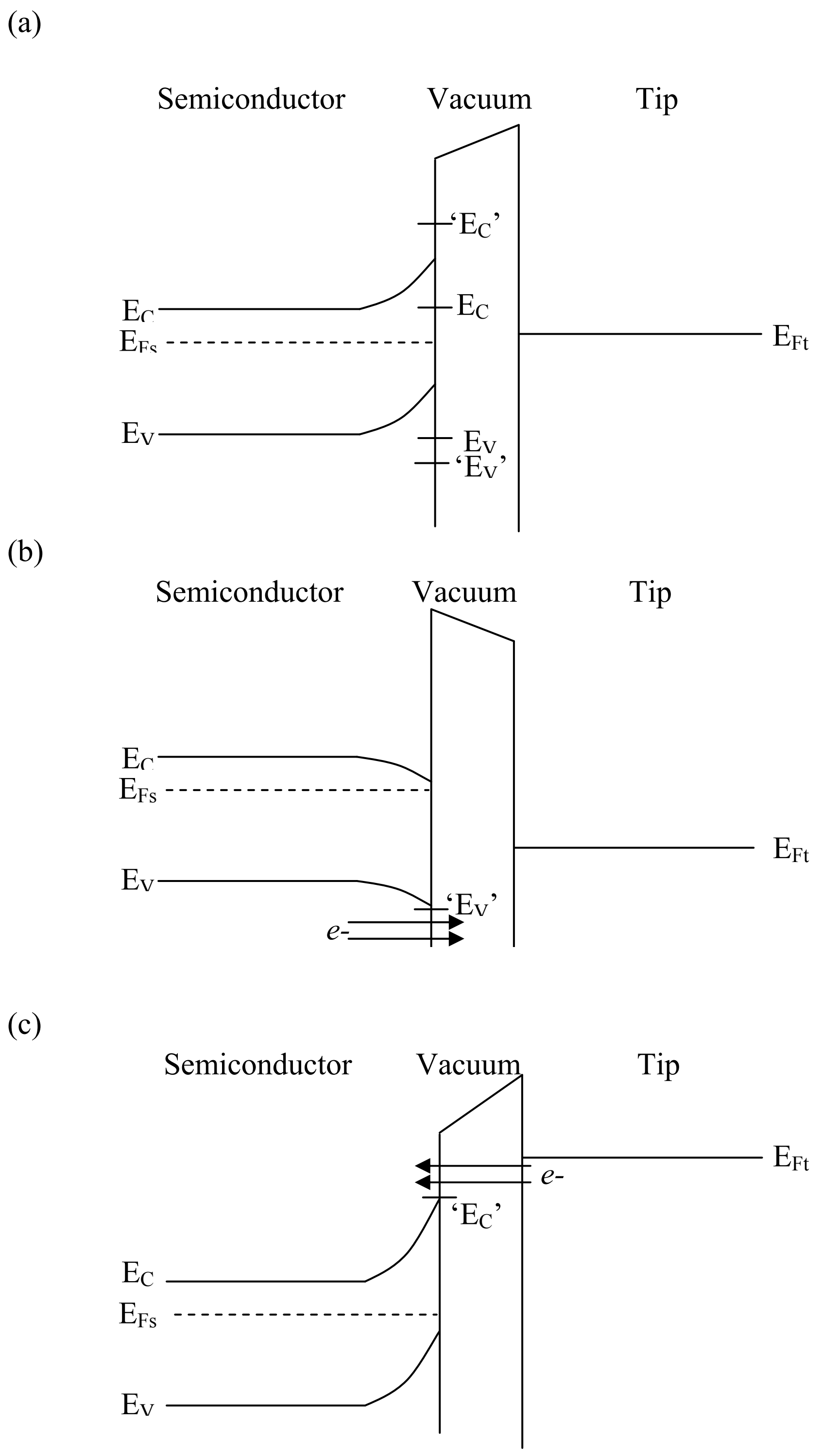

Fig. 2.9: Band diagram of semiconductor-vacuum-tip system at (a) zero bias (b) positive bias and (c) negative bias, for an n-type semiconductor. E_{Fs} (E_{Ft}) corresponds to the Fermi level of the sample (tip). Due to tip induced band bending, the measured positions of the conduction ('E_C') and valence ('E_V') band edges are shifted relative to the expected positions of the conduction (E_C) and valence (E_V) band edges.

2.6 References

[1] P. Cheuvart, U. El-Hanani, D. Schneider, and R. Triboulet, Journal of Crystal Growth **101**, 270 (1990).

[2] A. Y. Cho and S. E. Stokowsk, Solid State Communications **9**, 565 (1971).

[3] M. A. Herman, W. Richter, and H. Sitter, *Epitaxy Physical Principles and Technical Implementation*. (Springer, 2004).

[4] J. H. Neave, P. J. Dobson, B. A. Joyce, and J. Zhang, Applied Physics Letters **47**, 100 (1985).

[5] S. Nagata and T. Tanaka, Journal of Applied Physics **48**, 940 (1977).

[6] Y. Horikoshi and M. Kawashima, Journal of Crystal Growth **95**, 17 (1989).

[7] R. A. Stradling and P. C. Klipstein, *Growth and Characterisation of Semiconductors*. (Adam Hilger, Bristol, 1990).

[8] Y. Horikoshi, Semiconductor Science and Technology **8**, 1032 (1993).

[9] W. Cheng, Z. Zhong, Y. Wu, Q. Huang, and J. Zhou, Journal of Crystal Growth **183**, 279 (1998).

[10] G. E. Tsyrlin, A. O. Golubok, S. Y. Tipisev, and N. N. Ledentsov, Semiconductors **29**, 884 (1995).

[11] S. Franchi, G. Trevisi, L. Seravalli, and P. Frigeri, Progress in Crystal Growth and Characterization of Materials **47**, 166 (2003).

[12] J. D. Song, Y. M. Park, J. C. Shin, J. G. Lim, Y. J. Park, W. J. Choi, I. K. Han, J. I. Lee, H. S. Kim, and C. G. Park, Journal of Applied Physics **96**, 4122 (2004).

[13] B. Lita, Ph.D. Thesis, University of Michigan, 2001.

[14] R. M. Feenstra, Semiconductor Science and Technology **9**, 2157 (1994).

[15] R. S. Goldman, Journal of Physics D **37**, 163 (2004).

[16] P. S. Instruments, *User's Guide to the Autoprobe VP2*. (Park Scientific Instruments, Sunnyvale, 1996).

[17] B. Lita, R. S. Goldman, J. D. Phillips, and P. K. Bhattacharya, Applied Physics Letters **74**, 2824 (1999).

[18]J. N. Gleason, M. E. Hjelmstad, V. D. Dasika, R. S. Goldman, S. Fathpour, S. Charkrabarti, and P. K. Bhattacharya, Applied Physics Letters **86**, 011911 (2005).

[19]R. Triboulet, A. Lasbley, B. Toulouse, and R. Granger, Journal of Crystal Growth **79**, 695 (1986).

[20]E. P. Trifonova and L. Hitova, Thin Solid Films **224**, 153 (1993).

[21]W. D. Callister, *Fundamentals of Materials Science and Engineering*. (John Wiley & Sons, New York, 2001).

[22]J. N. Gleason, Master's Thesis, University of Michigan, 2006.

[23]R. M. Feenstra, Physical Review B **50**, 4561 (1994).

[24]R. M. Feenstra and J. A. Stroscio, Journal of Vacuum Science & Technology B **5**, 923 (1987).

[25]B. A. Orlowski, J. P. Lacharme, S. Bensalah, and C. A. Sebenne, Surface Science **200**, L460 (1988).

[26]B. Lita, R. S. Goldman, J. D. Phillips, and P. K. Bhattacharya, Applied Physics Letters **75**, 2797 (1999).

[27]B. Shin, B. Lita, R. S. Goldman, J. D. Phillips, and P. K. Bhattacharya, Applied Physics Letters **81**, 1423 (2002).

[28]M. McEllistrem, G. Haase, D. Chen, and R. J. Hamers, Physical Review Letters **70**, 2471 (1993).

[29]R. M. Feenstra, Physical Review B **50** (1994).

[30]C. K. Shih, R. M. Feenstra, and G. V. Chandrashekhar, Physical Review B **43**, 7913 (1991).

[31]J. A. Stroscio and W. J. Kaiser, in *Scanning Tunneling Microscopy* (Academic Press, Inc, 1993), Vol. 27, pp. 96.

[32]N. D. Lang, Physical Review B **34**, 5947 (1986).

[33]R. M. Feenstra, J. A. Stroscio, and A. P. Fein, Surface Science **181**, 295 (1987).

[34]M. Weimer, J. Kramar, and J. D. Baldeschwieler, Physical Review B **39**, 5572 (1989).

[35]S. Aloni and G. Haase, Journal of Vacuum Science & Technology B **17**, 2651 (1999).

[36]R. M. Feenstra, Journal of Vacuum Science & Technology B **21**, 2080 (2003).

[37] R. M. Feenstra, J. Y. Lee, M. H. Kang, G. Meyer, and K. H. Rieder, Physical Review B **73**, 035310 (2006).

[38] W. Morgan, Master's Thesis, University of Illinois at Urbana-Champaign, (in preparation).

[39] W. Morgan, H. T. Johnson, V. D. Dasika, and R. S. Goldman, (in preparation).

Chapter 3

CdZnTe Substrate Design and Characterization

3.1 Overview

This chapter begins with an introduction to mercury cadmium telluride (HgCdTe or MCT) based photodiode operation, sources of dark current, doping, and typical diode configurations. Then, the design of an appropriate substrate for the subsequent growth of MCT heterostructures is discussed. Details of our studies of the influence of the substrate thickness and orientation on cleaving, as well as our studies of the influence of substrate doping and annealing on resistivity are included. Finally, a sample structure to enable the examination of nanometer-scale structural and electronic variations in the MCT epitaxial layers is proposed. This work was supported by the Army Research Office Multidisciplinary University Research Initiative under Grant No. ARO-MURI DAAD19-01-1-0462.

3.2 Background

Mercury cadmium telluride (MCT or $Hg_{1-x}Cd_xTe$) has been used in the fabrication of infrared (IR) detectors since 1958.[1] MCT photodiodes have demonstrated high optical absorption coefficients and quantum efficiencies, and low thermal carrier generation rates.[2] A variety of detectors and focal plane arrays are fabricated using MCT based heterostructures.[3-9] However, currents which are present in the absence of the targeted illumination (termed dark currents), often limit the performance of MCT detectors. These dark currents are attributed to a combination of intrinsic effects such as thermally generated carriers, and extrinsic effects related to dislocations,[10-14] point defect clusters,[15,16] and alloy non-uniformities,[17,18] at the heterostructure interfaces. In this section, an overview of MCT diode operation and the extrinsic sources of dark current are presented, followed by details of doping of MCT films, examples of MCT diode configurations, and substrate choice.

3.2.1 MCT Photodiode Operation and Limitations

A photodiode is a *p-n* junction that is used to convert incident radiation into electricity. When a photon with energy equal to the bandgap energy, E_g, arrives at the depletion region of the *p-n* junction, an electron is excited from the valence band to the conduction band, producing a mobile electron-hole pair. The built-in field of the depletion region accelerates the holes toward the anode, and the electrons toward the cathode, thereby producing a photocurrent. For $Hg_{1-x}Cd_xTe$, the bandgap depends on the ratio of CdTe to HgTe, x, and temperature, T, and is expressed as:[19]

$$E_g = -0.303 + 1.93x - 0.81x^2 + 0.832x^3 + 5.35(1-2x)10^{-4}T \qquad (3.1)$$

The room temperature dependence of the MCT bandgap and wavelength on the cadmium fraction, x, is shown in Fig. 3.1. By adjusting x, MCT can potentially be used to detect radiation with wavelengths in the range of 0.7 – 25 μm. Thus, MCT photodiodes have applications in short-wavelength (1.4 – 3 μm), mid-wavelength (3 – 8 μm), and long-wavelength (8 – 14 μm) IR detection.[3-9]

The detector current is determined by the minority carriers collected from either side of the *p-n* junction. Thus, the highest detector currents occur for a maximum minority carrier diffusion length, L, given by:

$$L = \sqrt{D\tau} \tag{3.2}$$

where D is the minority carrier diffusivity and τ is the minority carrier lifetime. The minority carrier lifetime can be reduced due to the presence of recombination centers, which act as mid-gap carrier traps. Furthermore, MCT diode operation can be limited by a variety of materials issues, which will be discussed below.

3.2.2 MCT Materials Issues

Materials issues at the interfaces of the MCT heterostructure, such as alloy non-uniformities,[17,18] point defect clusters,[15,16] and dislocations,[10-14] are expected to be the primary sources of the dark currents, i.e. currents which are present in the absence of the targeted illumination. These issues and their influences on MCT diodes will be discussed below.

In MCT diodes, dark currents have been attributed to alloy non-uniformities and point defects. As indicated by Eq. 3.1, alloy non-uniformities can alter the bandgap of the material, thereby altering the wavelength to which the heterostructure is sensitive, leading to an increase in the detector current in the absence of the targeted illumination. Thus, dark currents in the MCT photodiode are often attributed to alloy non-uniformities within the layers.[17,18] Furthermore, x-ray diffraction studies of MCT films have revealed point defects such as Hg-vacancies or Te-antisites with concentrations as high as 10^{18} cm^{-3}.[15] Point defect concentrations of such a large magnitude can lead to the outward relaxation of the atoms surrounding the defect site, thereby altering the lattice constant, and thus, the bandgap of the material.[16] Similar to the case of alloy non-uniformities, a change in the bandgap of the material due to point defects can lead to an increase in the dark current.

Dark currents in MCT photodiodes have also been attributed to dislocations. For example, it has been suggested that Shockley-Read-Hall (SRH) recombination centers, which produce generation-recombination currents in the absence of light, as shown in Fig. 3.2(a), are due to the dangling bonds associated with dislocations.[10-14] In addition, trap-assisted tunneling currents, depicted in Fig. 3.2(b), have been attributed to the tunneling of minority carriers from one side of the depletion region to the other side via dangling bonds associated with dislocations located at or near the junction.[20] Thus, minimizing the lattice mismatch between the layers of a photodiode is critical because a large lattice mismatch can lead to the nucleation and propagation of dislocations through the device.[21] The lattice constant for $Hg_{1-x}Cd_xTe$ is given by the following equation:[22]

$$a = 6.4614 + (84x + 11.68x^2 - 5.7x^3)10^{-3} \qquad (3.3)$$

Thus, although the $Hg_{1-x}Cd_xTe$ bandgap varies significantly with the cadmium fraction, x, the lattice constant varies by < 1.4 % when x changes from 0 to 1. As a result, MCT heterostructures sensitive to a wide variety of wavelengths can be grown in a strain balanced structure on a CdTe or $Cd_{0.96}Zn_{0.04}Te$ substrate. [9,22]

3.2.3 MCT Diode Configurations

Typically, indium (In) and arsenic (As) are used as n-type and p-type dopants for MCT heterostructures, respectively.[23-30] During the MBE growth of MCT heterostructures, In is incorporated into the epilayers without the need for any additional annealing, resulting in *n*-doped MCT layers with high mobilities and long minority carrier lifetimes.[24,29] However, *p*-type doping of MBE-grown MCT layers is more challenging. The as-grown layers are typically *n*-type, and further annealing is required to activate the *p*-type dopants, such as As. To activate As doping for *p*-type layers, the films must be annealed at high temperatures of 400°C – 500°C, followed by an additional anneal at 250°C under Hg-rich conditions.[25,26]

Examples of *n*-on-*p* and *p*-on-*n* backside-illuminated MCT photodiodes are shown in Fig. 3.3.[2] Longer minority carrier lifetimes and lower trap concentrations have be achieved with an *n*-type base layer than in a *p*-type base layer.[24,29] Thus, *n*-type substrates are typically used for the subsequent growth of the MCT heterostructures.[2,31,32]

Furthermore, to minimize surface recombination, the *p*-*n* junction is typically designed with a larger (smaller) *p*-type (*n*-type) bandgap.

3.2.4 Nanometer-scale Examination of MCT Heterostructures

A few prior studies have considered the effects of dislocations and alloy non-uniformities on MCT photodiode performance. Prior TEM studies of MCT-based structures have revealed significant insights into the type and concentrations of dislocations.[14,33] However, as discussed in Section 1.2, the ability of TEM to resolve atomic-scale features is limited. Furthermore, previous studies of the influence of alloy non-uniformities on the MCT photodiode performance were limited to the micron length-scale.[34,35] Thus, the atomic-scale structure and electronic properties of interfaces remain the least understood aspect of MCT-based IR detector heterostructures.

To optimize MCT heterostructures for improved detector performance, detailed nanometer-scale characterization of the interface structure and local band-offsets is needed. XSTM is a powerful tool for exploring interfacial issues such as interface abruptness, diffusion of impurities, and the electronic properties of the *p*-*n* junction in MCT-based infrared detector structures. In the rest of this chapter, we report on the design of a substrate suitable for future XSTM studies of MCT-based heterostructures. As will be described in Section 3.5 of this dissertation, further work on this topic would require a new STM system capable of cleaving and XSTM in separate chambers.

3.3 Design and Growth of CdZnTe Substrates

Appendix D lists the lattice constants of MCT-based materials and some standard semiconductors.[36] The lattice mismatch between MCT-based materials and the substrates is ~ 12 – 19 % (8 – 14 %) for Si (for GaAs). The use of $Cd_{1-x}Zn_xTe$ or CdTe as a substrate would reduce the lattice mismatch to < 1.4% and would therefore be ideal for the subsequent growth of MCT for XSTM studies.[22,37]

CdTe substrates have traditionally been used as substrates for subsequent MCT heterostructure growth due to their commercial availability in 1" sizes.[9] CdTe substrates are typically grown by the Bridgman technique, under Te-rich conditions from Te-rich melts, leading to crystals with resistivities ranging from 10^3 to 10^4 Ω–cm, presumably due to p-type doping by Cd vacancies.[38] Thus, CdTe substrates are doped with group III elements such as In or Al to compensate for the excess of acceptors.[30] It is possible to synthesize alloys of $Cd_{0.96}Zn_{0.04}Te$ (CZT) which have the same lattice parameter as $Hg_{0.23}Cd_{0.77}Te$. Therefore, CZT is commonly used as the substrate for the subsequent growth of MCT heterostructures.[9,12,14,39] For epitaxial growth, (111)- and (211)-oriented substrates have produced films with fewer hillocks and twin faults than (100)-oriented substrates.[12,40,41] Thus, higher electronic quality films are expected to be possible for growth on (111)- and (211)- vs. (100)-oriented substrates.

To design an appropriate conductive substrate upon which a MCT heterostructure could subsequently be grown, we collaborated with J. Dinan from the Night Vision Laboratory (NVL) and M. Chu from Fermionics. The In-doped CdZnTe and CdTe substrates were grown by M. Chu using the Bridgman technique.[42] The In dopant was added directly to the crucible along with the Cd, Zn, and Te source materials. Once received, the substrates were polished and scribed as described in Section 2.3 of this dissertation. In this section, we discuss the influence of substrate orientation and thickness on cleaving, and the influence of doping and annealing on substrate resistivity. We were able to identify wafers for future use as a substrate for the subsequent growth of MCT heterostructures. Examining the MCT heterostructures using XSTM will require a new STM system capable of cleaving and XSTM in separate chambers, as will be discussed in Section 3.5.

3.3.1 Influence of Substrate Orientation and Thickness on Cleaving

A summary of the various substrates that were examined is provided in Table 3.1. First, we attempted to cleave undoped (100) $Cd_{0.96}Zn_{0.04}Te$ wafers (provided by J. Dinan). An example optical microscope image of the cleaved $Cd_{0.96}Zn_{0.04}Te$ (110) surface is shown in (a). For successful XSTM experiments, a typical cleaved surface consists of fracture lines confined to the region directly below the scribe mark, while the rest of the surface remains flat, as shown in Fig. 2.4. However, the surface shown in Fig. 3.4(a) is covered with fracture marks and it is likely that no flat area is available for XSTM. Several attempts at cleaving these wafers did not yield flat cleaves. Therefore, the (001) $Cd_{0.96}Zn_{0.04}Te$ wafers were considered unfit for our investigations.

Ideally, the XSTM sample under investigation is very brittle, and upon contact with the cleaver, the sample breaks along a specified scribe line, as described in Section 2.3.3 of this dissertation. However, various attempts at cleaving the $Cd_{0.96}Zn_{0.04}Te$

substrates revealed that if the substrates were thinned to < 500 μm, they would bend prior to breaking in the sample holder. The microhardness of $Cd_{0.96}Zn_{0.04}Te$ is approximately 48 kg/mm^2 (calculated using the law of mixtures and the microhardness values for CdTe and ZnTe in Table D.1) whereas the microhardness of GaAs is 670 kg/mm^2.[43,44] Thus, the lower optimal sample thickness for cleaving CdZnTe in comparison with that of GaAs is likely due to its lower microhardness.

We next attempted to cleave (111) $Cd_{0.96}Zn_{0.04}Te$ crystals (provided by M. Chu).[42] Polishing the (111) $Cd_{0.96}Zn_{0.04}Te$ crystals to a thickness of approximately 900 μm provided a flat cleave, as shown in Table 3.1. An optical microscope image of the exposed (110) surface of this substrate is shown in Fig. 3.4(b). A flat surface available for XSTM, along with fracture marks confined to the region below the scribe line, are clearly visible in this image. Thus, we identified the orientation (111) and thickness (900 μm) of $Cd_{0.96}Zn_{0.04}Te$ substrates that provided the best cleaves.

3.3.2 Influence of Doping and Annealing on Substrate Resistivity

As discussed in Section 2.3.1, to prevent tip crashes into the sample, it is essential to ensure that the sample is conductive enough to produce a tunneling current greater than 0.1 nA. Otherwise, the tip can crash into the sample while trying to detect a current, thus destroying both the tip and sample. A summary of the doping concentrations and resistivities of structures that have previously been examined by XSTM is presented in Table 3.2. In general, GaAs substrates doped to > 10^{18} cm^{-3} are utilized. The resistivities are usually $< 10^{-3}$ Ω-cm. Therefore, we aimed to fabricate substrates with a resistivity $< 10^{-3}$ Ω-cm.

The (111) $Cd_{0.96}Zn_{0.04}Te$ crystals were In-doped at ~ 8×10^{16} cm^{-3}.[45] The resistivity of the as-grown $Cd_{0.96}Zn_{0.04}Te$:In wafers varied from wafer to wafer and from location to location, within the range 0.5 – 3 Ω-cm. Although we were able to obtain a flat cleave from these substrates as discussed in the previous section, the sample resistivity was too high. As a result, during the auto-approach, instead of stopping a few Å away from the surface, the STM tip crashed into the sample, as indicated by the hole in Fig. 3.4(b). Thus, further reduction of the substrate resistivity was necessary.

To lower the resistivity of the CdZnTe crystals, post-growth annealing was performed using a recipe in the literature.[46,47] Specifically, (111) $Cd_{0.96}Zn_{0.04}Te$:In was annealed under Cd and Zn overpressure, producing a substrate with a uniform resistivity of 0.2 – 0.3 Ω-cm. However, as shown in Table 3.1, we were still unable to detect a tunneling current from this sample.

To further lower the resistivity, we moved to (111) CdTe:In crystals, which have exhibited resistivities lower than 0.1 Ω-cm.[48] Thus, we moved to (111) CdTe substrates in lieu of (111) $Cd_{0.96}Zn_{0.04}Te$ substrates. A (111) CdTe crystal was heavily doped with In to ~ 2.2×10^{17} cm^{-3} to bring the resistivity down to 3-5 Ω-cm. Following doping, the substrate was annealed under Cd overpressure at 750 °C.[48] This further lowered the resistivity to 0.04 Ω-cm. As summarized in Table 3.1, we obtained a flat cleave from this (111) CdTe sample, and we were also able to tunnel into the substrate. Fig. 3.5 shows an example XSTM topographic image of the (110) surface of the CdTe substrate, with an total grey scale range of 8.2 Å. Thus, after several attempts at doping and annealing

$Cd_{0.96}Zn_{0.04}Te$ and CdTe crystals, we identified wafers that can be used as a substrate for the subsequent growth of MCT heterostructures. In addition, these CdTe:In substrates also have potential applications in x-ray and γ-ray detectors.[49-52] For example, doping with In has been found to reduce the leakage current and improve the energy resolution of the CdTe-based x-ray and γ-ray detectors.[49-52]

3.4 Proposed Heterostructure

The goal of these studies was to investigate the interfacial structure and local band-offsets in HgCdTe based heterostructures at the nanometer-scale. As shown in Fig. 3.6, a possible structure consists of HgCdTe layers grown on a (111) CdTe:In substrate. The heterostructure consists of a single *p-n* junction and a multilayer consisting of 50 nm of CdTe/HgCdTe superlattice, which would serve as a marker layer. The *p-n* junction is composed of *p*-type $Hg_{0.68}Cd_{0.32}Te$:As ($\lambda \sim 3 - 5$ μm) and *n*-type $Hg_{0.77}Cd_{0.23}Te$:In ($\lambda \sim 8 - 12$ μm). Indium would be used as the n-type dopant while As will be used as the p-type dopant.

3.5 Planning for a Separate Cleaving Chamber

XSTM experiments are typically conducted under ultra high vacuum (UHV) conditions. Since MCT has a very high Hg vapor pressure at ~ 70 °C, Hg will vaporize from the MCT surface, in appreciable quantities, at ~ 70 °C.[24,53] This is problematic in systems such as ours, where the sample cleaving and imaging occur in the same UHV chamber. Any cleaved pieces of MCT on the chamber bottom would release appreciable quantities of Hg during a chamber bakeout (typically ~ 150 °C), detrimentally contaminating the STM and the chamber. Thus, in order to pursue XSTM studies of the structure in Fig. 3.6, a dedicated system with cleaving capabilities in a separate but interconnected chamber would be needed.

3.6 Conclusions

In summary, we have investigated the influence of substrate orientation and thickness on the cleavage of CdTe and $Cd_{0.96}Zn_{0.04}Te$ substrates, as well as the influence of In doping and annealing on the substrate resistivity. Although cleaving (100)-oriented $Cd_{0.96}Zn_{0.04}Te$ wafers along the (110) resulted in significant surface topography, flat cleaves were obtained for (111)-oriented CdTe and $Cd_{0.96}Zn_{0.04}Te$ wafers cleaved along (110). The wafer thickness was also optimized and the flattest cleaves were obtained for substrates that were approximately 900 μm thick. Furthermore, we developed substrate growth and processing procedures to lower the substrate resistivity, thereby enabling the detection of an STM tunneling current. Using both In-doping ($n \sim 2.2 \times 10^{17}$ cm^{-3}) and post-growth annealing ($T = 750$ °C) in a Cd-rich environment, the CdTe substrate resistivity was reduced to 0.04 Ω-cm. For these samples, both XSTM imaging and spectroscopy were successfully performed. A sample structure to enable the nanometer-scale examination of $Hg_{-x}Cd_xTe$ films sensitive to mid-to-long wavelength infrared radiation was subsequently proposed. However, to pursue XSTM studies of the MCT heterostructures, a dedicated system with cleaving capabilities in a separate but interconnected chamber is needed.

Substrate	**Orientation**	**Doping (cm^{-3})**	**Resistivity (Ω-cm)**	**Flat Cleave**	**Tunneling**
$Cd_{0.96}Zn_{0.04}Te$	(100)	Undoped	5×10^{10}	No	No
$Cd_{0.96}Zn_{0.04}Te$	(111)	$\sim 8 \times 10^{16}$	0.5 – 3	Yes	No
$Cd_{0.96}Zn_{0.04}Te$	(111)	$\sim 8 \times 10^{16}$ (Annealed)	0.2 – 0.3	Yes	No
CdTe	(111)	$\sim 2.2 \times 10^{17}$ (Annealed)	~ 0.04	Yes	Yes

Table 3.1: Summary of cleaving and tunneling attempts of various MCT-based substrates. A flat cleave implies that after cleaving, the cross section of the sample included a flat area suitable for XSTM studies. ‘Tunneling’ indicates that a tunneling current was detected when the tip approached the sample, and that the tip did not crash into the sample.

	GaAs (n-Si)	**GaAs (p-Be)**	**Si (n)**	**Si (p)**	**InAlAs**	**$Hg_{1-x}Cd_xTe$ (n-In)**	**$Hg_{1-x}Cd_xTe$ (p-As)**	**$Hg_{1-x}Cd_xTe$**
Doping concentration (cm^{-3})	[58]5×10^{18} [62]3×10^{18} [61]1×10^{18} [63]4×10^{17}	[58]1×10^{19} [60,61]5×10^{18}	[58]2×10^{18}	[58]2×10^{18} [59]$1\text{-}5 \times 10^{17}$	[57]Undoped	[56]2×10^{15} (x=0.323) [23]1.1×10^{16} (x=0.23) [55]3×10^{18} (x=0.23)	[54]3×10^{16} (x=0.3) [54]5×10^{15} (x=0.32) [55]2×10^{18} (x=0.3)	Undoped
Resistivity (Ω-cm)	[58]0.00015 [62]0.00045 [61]0.00070 [63]0.0018	[58]0.0016 [61]0.0031	[58]0.0021	[58]0.0069 [59]0.029-0.139	[57]0.11-0.21	[56]0.1221 [23]0.0111 [55]0.0001	[54]0.2586 [54]0.0667 [55]0.114	0.0111 (x=0.23) 0.0667 (x=0.30) 0.1128 (x=0.32)
Depletion width (nm)	25.18	25.18	36.10	36.10	-	10.44	10.44	

Table 3.2: Table summarizing sample details on previous XSTM experiments on GaAs, Si and MCT *p-n* junctions.

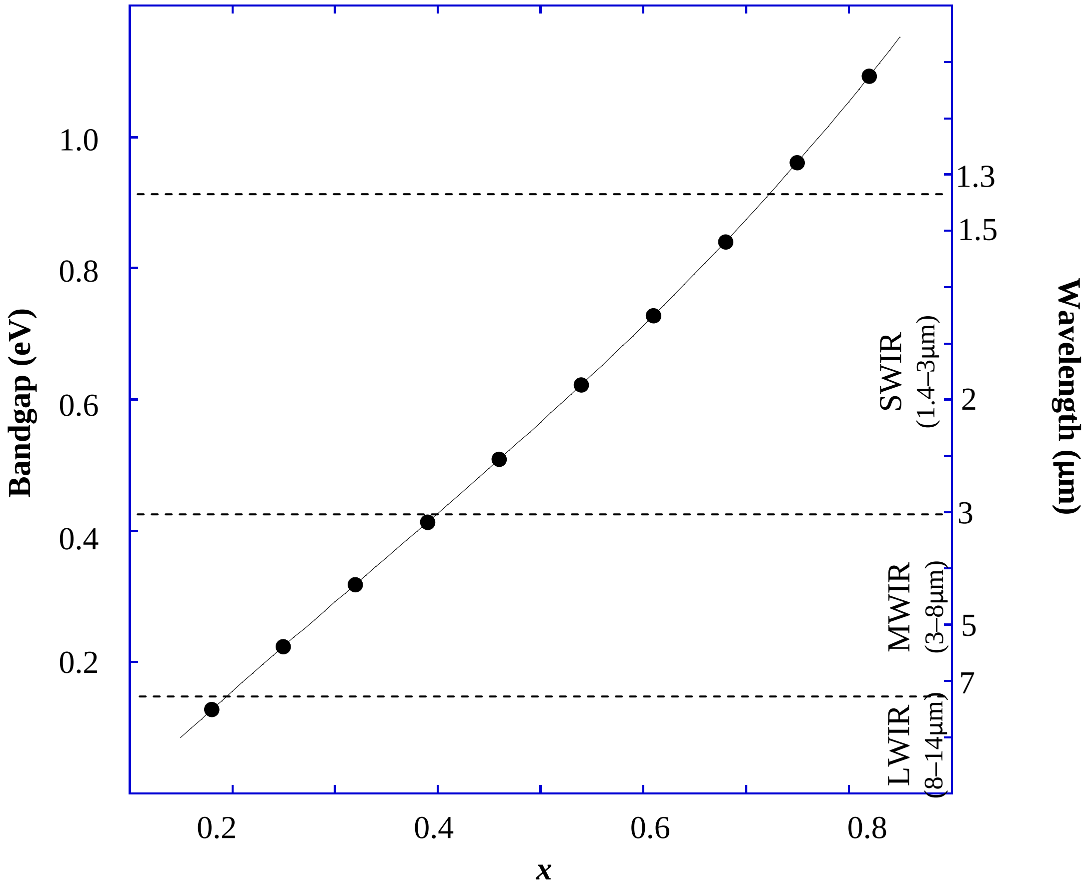

Fig. 3.1: Calculated bandgap and wavelength variation with percentage of CdTe, *x*, in $Hg_{1-x}Cd_{x}Te$.[19] MCT photodiodes have applications in short-wavelength (SWIR, $x \sim 0.5$-0.7), mid-wavelength (MWIR, $x \sim 0.3$), and long-wavelength (LWIR, $x \sim 0.2$) infrared detection.[3-9]

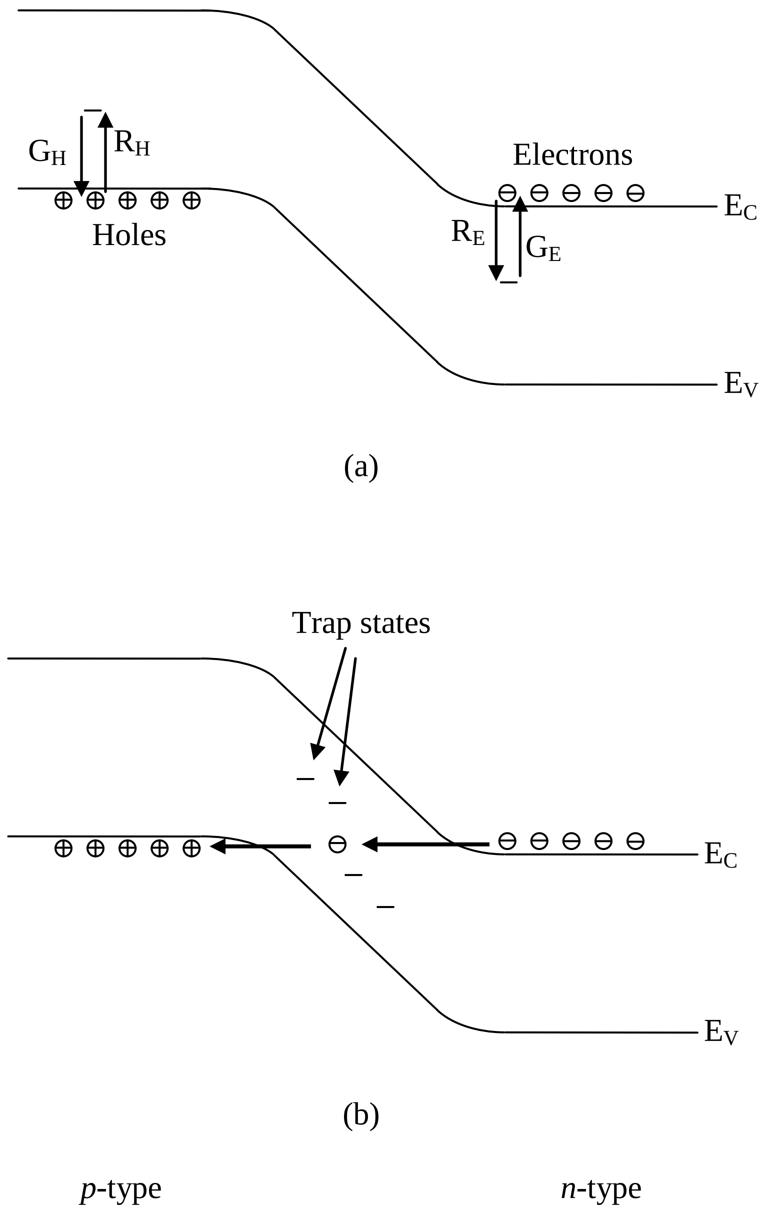

Fig. 3.2: Band diagram depicting possible sources of the dark current in MCT heterostructures: (a) Shockley-Read-Hall (SRH) recombination, and (b) trap assisted tunneling.

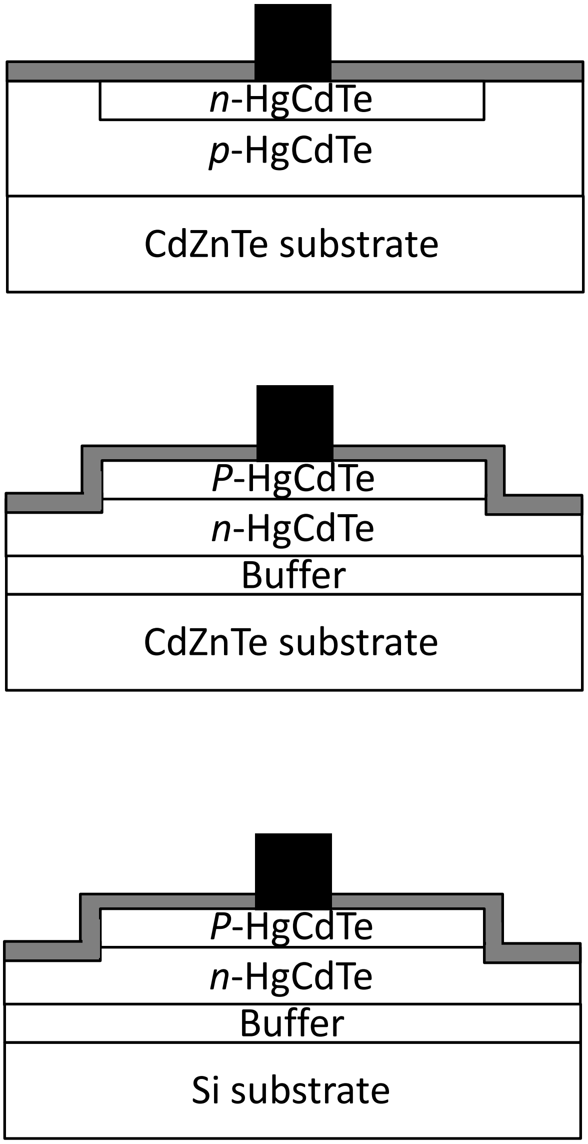

Fig. 3.3: Examples of backside illuminated HgCdTe photodiode architectures: (a) planar ion implanted *n*-on-*p* homojunction grown on CdZnTe substrate, (b) *P*-on-*n* heterojunction, and (c) *P*-on-*n* heterojunction on silicon substrate.[2]

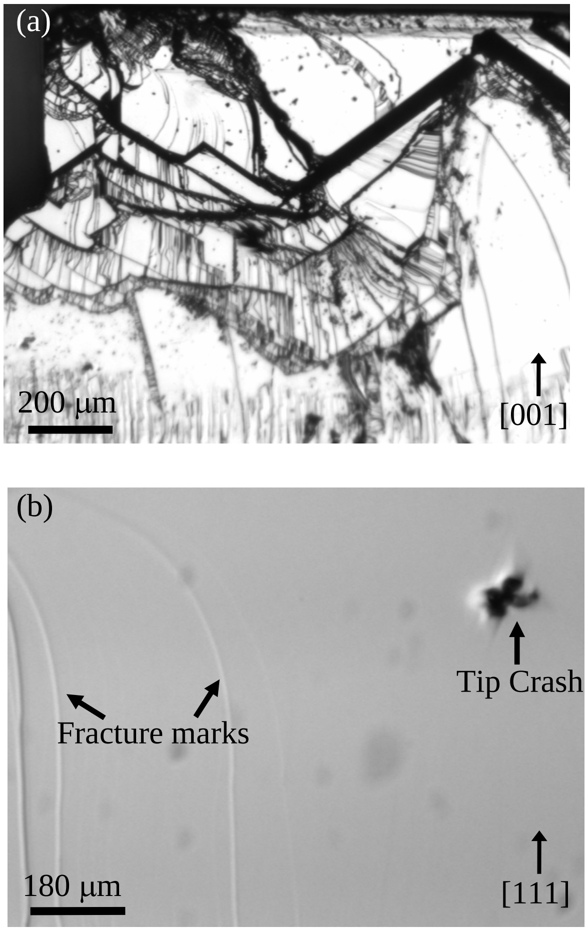

Fig. 3.4: Optical microscopy images of cleaved CdZnTe (110) surfaces: (a) (001)-oriented undoped CdZnTe, showing significant cleaved surface topography, and (b) (111)-oriented CdZnTe, doped at approximately 8×10^{16} cm^{-3}, showing a smooth surface and evidence of a tip crash due to insufficient sample conductivity.

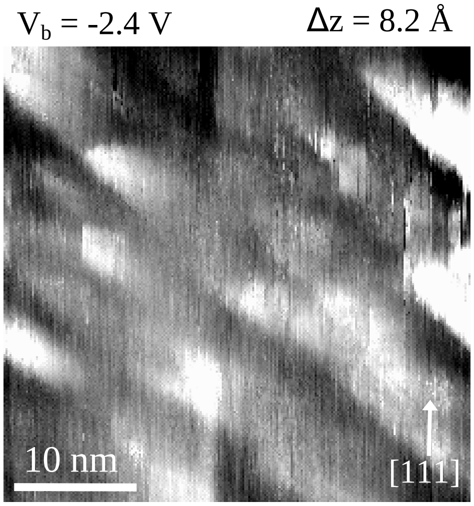

Fig. 3.5: XSTM topographic image of low-resistivity CdTe (left) collected at a bias voltage of -2.4 V. The total grayscale range displayed is 8.2Å.

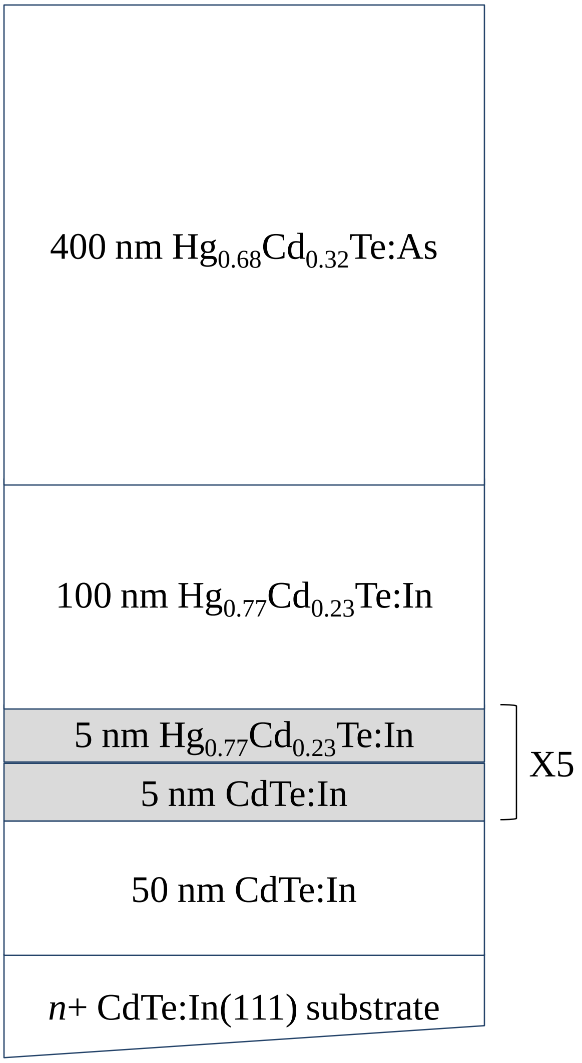

Fig. 3.6: Cross-section of the target layer structure which consisted of a *p*-*n* junction consisting of *p*-type $Hg_{0.68}Cd_{0.32}Te$:As and *n*-type $Hg_{0.77}Cd_{0.23}Te$:In. The entire structure is to be grown on a (111)-oriented CdTe:In substrate. A multilayer consisting of 50 nm of CdTe:In/$Hg_{0.77}Cd_{0.23}Te$:In superlattices would serve as a marker layer.

3.7 References

[1] W. D. Lawson, S. Nielsen, E. H. Putley, and A. S. Young, Journal of Physics and Chemistry of Solids **9**, 325 (1959).

[2] A. Rogalski, Progress in Quantum Electronics **27**, 151 (2003).

[3] S. E. Botts, IEEE Transactions on Electron Devices **32**, 1584 (1985).

[4] L. Bubulac, W. Tennant, J. Pasko, L. Kozlowski, M. Zandian, M. Motamedi, R. De Wames, J. Bajaj, N. Nayar, W. McLevige, N. Gluck, R. Melendes, D. Cooper, D. Edwall, J. Arias, R. Hall, and A. D'souza, Journal of Electronic Materials **26**, 649 (1997).

[5] P. Tribolet, S. Blondel, P. Costa, A. Combette, L. Vial, G. Destefanis, P. Ballet, J. P. Zanatta, O. Gravrand, C. Largeron, J. P. Chamonal, and A. Million, Infrared Technology and Applications XXXII **6206**, 62062F (2006).

[6] M. B. Reine, J. W. Marciniec, K. K. Wong, T. Parodos, J. D. Mullarkey, P. A. Lamarre, S. P. Tobin, K. A. Gustavsen, and G. M. Williams, Journal of Electronic Materials **36**, 1059 (2007).

[7] R. Singh, S. Velicu, J. Crocco, Y. Chang, J. Zhao, L. Almeida, J. Markunas, A. Kaleczyc, and J. Dinan, Journal of Electronic Materials **34**, 885 (2005).

[8] M. Carmody, J. G. Pasko, D. Edwall, E. Piquette, M. Kangas, S. Freeman, J. Arias, R. Jacobs, W. Mason, A. Stoltz, Y. Chen, and N. K. Dhar, Journal of Electronic Materials **37**, 1184 (2008).

[9] P. Norton, Opto-Electronics Review **10**, 159 (2002).

[10] S. M. Johnson, D. R. Rhiger, J. P. Rosbeck, J. M. Peterson, S. M. Taylor, and M. E. Boyd, Journal of Vacuum Science & Technology B **10**, 1499 (1992).

[11] R. List, Journal of Electronic Materials **22**, 1017 (1993).

[12] H. Figgemeier, M. Bruder, K.-M. Mahlein, R. Wollrab, and J. Ziegler, Journal of Electronic Materials **32**, 588 (2003).

[13] V. Gopal and S. Gupta, Journal of Applied Physics **95**, 2467 (2004).

[14] T. Aoki, Y. Chang, G. Badano, J. Zhao, C. Grein, S. Sivananthan, and D. J. Smith, Journal of Crystal Growth **265**, 224 (2004).

[15] N. Mainzer and E. Zolotoyabko, Diffusion and Defect Data A **183**, 103 (2000).

[16] N. Mainzer, E. Lakin, and E. Zolotoyabko, Applied Physics Letters **81**, 763 (2002).

[17] X. Z. Liao and T. S. Shi, Applied Physics Letters **66**, 2089 (1995).

[18] V. Gopal, S. K. Singh, and R. M. Mehra, Infrared Physics & Technology **43**, 317 (2002).

[19] G. L. Hansen, J. L. Schmit, and T. N. Casselman, Journal of Applied Physics **53**, 7099 (1982).

[20] Y. Nemirovsky, R. Fastow, M. Meyassed, and A. Unikovsky, Journal of Vacuum Science & Technology B **9**, 1829 (1991).

[21] P. Sheldon, B. G. Yacobi, K. M. Jones, and D. J. Dunlavy, Journal of Applied Physics **58**, 4186 (1985).

[22] W. M. Higgins, G. N. Pultz, R. G. Roy, R. A. Lancaster, and J. L. Schmit, Journal of Vacuum Science & Technology A **7**, 271 (1989).

[23] P. S. Wijewarnasuriya, J. P. Faurie, and S. Sivananthan, Journal of Crystal Growth **159**, 1136 (1996).

[24] J.-P. Faurie, Progress in Crystal Growth and Characterization of Materials **29**, 85 (1994).

[25] S. Sivananthan, P. Wijewarnasuriya, F. Aqariden, H. Vydyanath, M. Zandian, D. Edwall, and J. Arias, Journal of Electronic Materials **26**, 621 (1997).

[26] D. Edwall, E. Piquette, J. Ellsworth, J. Arias, C. Swartz, L. Bai, R. Tompkins, N. Giles, T. Myers, and M. Berding, Journal of Electronic Materials **33**, 752 (2004).

[27] J. Hails, S. Irvine, D. Cole-Hamilton, J. Giess, M. Houlton, and A. Graham, Journal of Electronic Materials **37**, 1291 (2008).

[28] G. K. O. Tsen, R. H. Sewell, A. J. Atanacio, K. E. Prince, C. A. Musca, J. M. Dell, and L. Faraone, Semiconductor Science and Technology **23**, 015014 (2008).

[29] V. Varavin, S. Dvoretskii, D. Ikusov, N. Mikhailov, Y. Sidorov, G. Sidorov, and M. Yakushev, Semiconductors **42**, 648 (2008).

[30] V. Babentsov, J. Franc, and R. B. James, Applied Physics Letters **94**, 052102 (2009).

[31] E. A. Berkman, N. A. El-Masry, A. Emara, and S. M. Bedair, Applied Physics Letters **92**, 101118 (2008).

[32] I. Kimukin, N. Biyikli, B. Butun, O. Aytur, S. M. Unlu, and E. Ozbay, IEEE Photonics Technology Letters **14**, 366 (2002).

[33]C. Wang, X. Wang, J. Zhao, Y. Chang, C. H. Grein, S. Sivananthan, and D. J. Smith, Journal of Crystal Growth **309**, 153 (2007).

[34]M. W. Muller and A. Sher, Applied Physics Letters **74**, 2343 (1999).

[35]J. D. Phillips, K. Moazzami, J. Kim, D. D. Edwall, D. L. Lee, and J. M. Arias, Applied Physics Letters **83**, 3701 (2003).

[36]O. Madelung, *Semiconductors - Basic Data*. (Springer-Verlag, 1996).

[37]J. H. Dinan and S. B. Qadri, Journal of Vacuum Science & Technology A **4**, 2158 (1986).

[38]C. Szeles, IEEE Transactions on Nuclear Science **51**, 1242 (2004).

[39]R. Schoolar, S. Price, and J. Rosbeck, Journal of Vacuum Science & Technology B **10**, 1507 (1992).

[40]R. J. Koestner and H. F. Schaake, Journal of Vacuum Science & Technology A **6**, 2834 (1988).

[41]A. Parikh, S. D. Pearson, T. K. Tran, R. N. Bicknell, R. G. Benz, B. K. Wagner, P. Schäfer, and C. J. Summers, Journal of Crystal Growth **159**, 1152 (1996).

[42]M. Chu, S. Tererian, D. Ting, C. Wang, J. D. Benson, J. H. Dinan, R. B. James, and A. Burger, Journal of Electronic Materials **32**, 778 (2003).

[43]R. Triboulet, A. Lasbley, B. Toulouse, and R. Granger, Journal of Crystal Growth **79**, 695 (1986).

[44]E. P. Trifonova and L. Hitova, Thin Solid Films **224**, 153 (1993).

[45]M. Chu, S. Tererian, D. Ting, C. Wang, J. D. Benson, J. H. Dinan, R. B. James, and A. Burger, Journal of Electronic Materials **32** (2003).

[46]Q. Li, W. Jie, L. Fu, G. Yang, G. Zha, T. Wang, and D. Zeng, Journal of Applied Physics **100**, 013518 (2006).

[47]V. Lyahovitskaya, L. Chernyak, J. Greenberg, L. Kaplan, and D. Cahen, Journal of Crystal Growth **214-215**, 1155 (2000).

[48]V. Lyahovitskaya, L. Kaplan, J. Goswami, and D. Cahen, Journal of Crystal Growth **197**, 106 (1999).

[49]R. Sudhaesanan, G. Vakerlis, and N. Karam, Journal of Electronic Materials **26**, 745 (1997).

[50]C. Matsumoto, T. Takahashi, K. Takizawa, R. Ohno, T. Ozaki, and K. Mori, IEEE Transactions on Nuclear Science **45**, 428 (1998).

[51] M. Niraula, A. Nakamura, T. Aoki, H. Tatsuoka, and Y. Hatanaka, Journal of Electronic Materials **30**, 911 (2001).

[52] C. Szeles, Physica Status Solidi (b) **241**, 783 (2004).

[53] R. F. C. Farrow, G. R. Jones, G. M. Williams, P. W. Sullivan, W. J. O. Boyle, and J. T. M. Wotherspoon, Journal of Physics D **12**, L117 (1979).

[54] J. P. Rosbeck, R. E. Starr, S. L. Price, and K. J. Riley, Journal of Applied Physics **53**, 6430 (1982).

[55] R. Zucca, M. Zandian, J. M. Arias, and R. V. Gil, Journal of Vacuum Science & Technology B **10**, 1587 (1992).

[56] N. K. Dhar, M. Zandian, J. G. Pasko, J. M. Arias, and J. H. Dinan, Applied Physics Letters **70**, 1730 (1997).

[57] B. Shin, A. Lin, K. Lappo, R. S. Goldman, M. C. Hanna, S. Francoeur, A. G. Norman, and A. Mascarenhas, Applied Physics Letters **80**, 3292 (2002).

[58] K.-J. Chao, A. R. Smith, A. J. McDonald, D.-L. Kwong, B. G. Streetman, and C.-K. Shih, Journal of Vacuum Science & Technology B **16**, 453 (1998).

[59] E. T. Yu, K. Barmak, P. Ronsheim, M. B. Johnson, P. McFarland, and J.-M. Halbout, Journal of Applied Physics **79**, 2115 (1996).

[60] J. N. Gleason, M. E. Hjelmstad, V. D. Dasika, R. S. Goldman, S. Fathpour, S. Charkrabarti, and P. K. Bhattacharya, Applied Physics Letters **86**, 011911 (2005).

[61] S. Gwo, K.-J. Chao, and C. K. Shih, Applied Physics Letters **64**, 493 (1994).

[62] B. Lita, R. S. Goldman, J. D. Phillips, and P. K. Bhattacharya, Applied Physics Letters **74**, 2824 (1999).

[63] A. Vaterlaus, R. M. Feenstra, P. D. Kirchner, J. M. Woodall, and G. D. Pettit, Journal of Vacuum Science & Technology B **11**, 1502 (1993).

Chapter 4

Influence of Alloy Buffer and Capping Layers on Quantum Dot Formation

4.1 Overview

Quantum dots are typically surrounded by a larger bandgap material to enable carrier confinement within the nanostructures. Thus, InAs quantum dots are typically grown on buffers of and capped with layers of GaAs or $In_xGa_{1-x}As$ alloys. This chapter describes investigations of the influence of InGaAs alloy buffer and capping layers on the size, shape, and density of InAs/GaAs dots and corresponding wetting layers (WLs). Large scale and high resolution cross-sectional scanning tunneling microscopy (XSTM) images reveal larger dimensions, density, and WL thicknesses for the dots with alloy buffer and capping layers (termed alloy quantum dots or “AQDs”) in comparison with the quantum dots (QDs) without surrounding alloy layers. Taking into account the reduction in misfit strain at the buffer/dot and dot/cap interfaces, a mechanism for dot formation and collapse in the absence and presence of InGaAs alloy buffer and capping layers is proposed.

This chapter opens with an introduction to QD nucleation, followed by a brief review of prior experimental investigations into the influence of alloy layers on quantum dot formation. The experimental methods are then described. Next, we report the influence of InGaAs alloy buffer and capping layers on dot dimensions, density, and WL thickness. Finally, a strain-based mechanism for dot formation and collapse in the absence and presence of alloy layers is presented. This mechanism is likely to be applicable to a wide range of similarly lattice-mismatched thin-film systems. The chapter concludes with a summary. This work was supported in part by the Army Research Office Multidisciplinary University Research Initiative under Grant No. ARO-MURI DAAD19-01-1-0462 and by the Department of Energy under Grant No. DE-FG02-06ER46339, monitored by J. Zhu.

4.2 Background

The atomic structure of InAs/GaAs dots has been reported to be influenced by a number of growth parameters including substrate temperature, III/V flux ratio, growth rate, and the presence of alloy buffer and/or capping layers.[1-6] For example, growth with an alternating supply of anion and cation species is expected to increase the cation diffusion length, thereby lowering the film thickness for the 2D to 3D Stranski-Krastanow (S-K) growth mode transition, resulting in larger dots.[7-13] In addition, for quantum dot superlattices, strain fields in the GaAs capping layers above the underlying dots typically leads to vertical dot alignment often termed ‘stacking’.[14-18] Furthermore, intermixing between the InAs dots and the GaAs buffer and capping layers leads to alloy formation within the dots and the surrounding wetting layer (WL), thereby altering their atomic structure.[19-22] The use of intentionally alloyed buffer and capping layers has also been found to influence dot atomic structure.[1-6] However, the effects of alloy buffer and capping layers on the dot sizes and wetting layer (WL) thickness remain unknown. In this section, a review of the dot formation process is presented, followed by a summary of previous studies on the influence of alloy layers on dot size and density.

4.2.1 Dot Nucleation

Three growth modes are generally encountered during thin film growth, as shown in Fig. 4.1: (a) Frank-van der Merwe (FvdM), (b) Volmer-Weber (V-W), and (c) Stranski-Krastanow (S-K).[23] The growth mode is determined by the relative surface energies of the growing thin film, γ_f, with respect to the sum of the substrate surface energy, γ_s, plus the interface energy, γ_{int}.[24] When $\gamma_f < \gamma_s + \gamma_{int}$, the atoms of the film are more strongly attracted to the substrate than to each other, leading to layer-by-layer growth (FvdM), as shown in Fig. 4.1(a). On the other hand, when $\gamma_f > \gamma_s + \gamma_{int}$, the atoms of the film are more strongly attracted to each other than to the substrate, leading to island growth (VW), as shown in Fig. 4.1(b).[23] In some systems, γ_{int} is thickness-dependent, increasing with the thickness of the growing film. Thus, layer-by-layer growth occurs up to a critical film thickness, followed by a so-called “Stranski-Krastanow” transition to island growth, as shown in Fig. 4.1(c). Strain-induced S-K growth has been observed in a wide variety of systems, including Ge/Si[25-27] and InAs/GaAs.[28-30] In those cases, the film/substrate mismatch strain is relaxed elastically by the formation of islands.

The dependence of the critical film thickness and maximum dot volume on the mismatch strain can be derived from the equation for the surface energy. The free energy of the surface during film growth, *E*, is composed of surface and elastic terms:

$$E = E_{elastic} + E_{surface} = E_{elastic} + \gamma_f \quad (4.1)$$

The elastic energy of the film is a function of the film's biaxial modulus, M, mismatch strain, ε, and volume, V, and can be expressed as:[31]

$$E_{elastic} = (1-\alpha)M\varepsilon^2 V \quad (4.2)$$

where α is the fractional elastic relaxation of the film relative to the substrate. Therefore, for 3D islands, $\alpha = h/D$ where h is the height of the island and D is the diameter, and for 2D films, $\alpha \rightarrow 0$. Thus for the growth of a 2D film such as the WL, the free energy per unit area can be written as:[32]

$$E_{2D} = M\varepsilon^2 h_f + \gamma_f \quad (4.3)$$

where h_f is the thickness of the film. Similarly, after the S-K transition, the free energy per unit area of the 3D film can be expressed as: [32]

$$E_{3D} = (1-\alpha)M\varepsilon^2 h_f + \gamma_f + \Delta\gamma \quad (4.4)$$

where $\Delta\gamma = \gamma_{SK} - \gamma_f$, and γ_{SK} is the surface energy of the 3D film. At the onset of dot nucleation, $h_f = h_c$, the critical thickness, and $E_{2D} = E_{3D}$, so equations (4.3) and (4.4) above can be set equal:

$$M\varepsilon^2 h_c + \gamma_f = (1-\alpha)M\varepsilon^2 h_c + \gamma_{SK} \tag{4.5}$$

Solving the above equation for h_c yields:

$$h_c = \frac{\Delta\gamma}{M\varepsilon^2\alpha} \tag{4.6}$$

Thus, the critical thickness for dot nucleation scales as $1/\varepsilon^2$.[33,34] Thus, we can expect a larger critical WL thickness for systems in which the mismatch strain between the buffer layer and the dot material is lower. The mismatch strain, ε, is dependent on the film and substrate lattice constants, a_f and a_s, as follows:

$$\varepsilon = (a_s - a_f)/a_f \tag{4.7}$$

Following the transition from 2D to 3D growth, additional deposition of the thin film leads to an increase in island size. The islands continue to increase in size, and after the islands reach a critical volume, V_c, dislocation nucleation occurs. The critical volume scales as:[31,35]

$$V_C \sim \frac{1}{\varepsilon^6} \tag{4.8}$$

The misfit, ε_f, is defined as:

$$\varepsilon_f = (a_f - a_s)/a_s \tag{4.9}$$

Thus, we can expect a larger critical volume for systems in which the buffer/dot misfit is lower. A summary of the dependence of the critical WL thickness and dot volume on mismatch strain is shown in Fig. 4.2. In the following sub-sections, a review of previous studies on the use of intentionally alloyed buffer and capping layers is provided.

4.2.2 Influence of Alternate Cation and Anion Deposition on Dot Formation

Thin film growth by MBE and MEE has been described in Chapter 2. During film growth by MBE, the cation diffusion length is typically dependent on the substrate temperature.[36-38] For example, increasing the substrate temperature during the growth of GaAs has been reported to increase the Ga surface diffusion length.[36,37] In the case of the alternate deposition of cation and anion species as in MEE, the cation diffusion length may be tuned via the variation of the on/off time-periods of the sources.[7,12] Thus, during the MEE growth of InAs, a longer cation diffusion length is typically observed, similar to the case of MBE at a higher substrate temperature. In several papers, InAs/GaAs dot growth via MBE and MEE has been compared.[8-13] In all cases, dot growth via MEE and MBE both displayed a RHEED pattern change indicating a 2D to 3D growth mode transition, confirming that dot growth occurs via the S-K growth mode transition. Thus, this investigation of the influence of alloy buffer and capping layers on InAs/GaAs dot formation has general applicability to thin film systems which exhibit the S-K growth mode transition.

4.2.3 Influence of Alloy Buffer Layers on Dot Formation

To enable carrier confinement, InAs dots are typically grown on buffers of GaAs or $In_xGa_{1-x}As$ alloys. Interestingly, it has been reported that InAs/GaAs dots grown on InGaAs buffers have higher densities than those grown directly on GaAs.[1-3] However, there have been conflicting reports on the effect of alloy buffers on dot size. For example, in one report, AFM images suggested that the presence of an alloy buffer does not influence dot size[1]; other studies have suggested that similar alloy buffers lead to an increase[2] or decrease[3] in dot dimensions. Thus, the influence of alloy buffer layers on dot size and WL thickness remains unknown.

4.2.4 Influence of Alloy Capping Layers on Dot Formation

Quantum dots are typically capped with a larger bandgap material to confine carriers within the nanostructures. For example, InAs dots are typically capped with GaAs or $In_xGa_{1-x}As$ alloys. The procedure of capping can change the dot morphology, leading to a reduction in dot height, also known as dot “collapse”.[4-6] It has been suggested that capping InAs/GaAs dots with InGaAs or GaAsSb in lieu of GaAs minimizes the tendency for dot “collapse”.[4-6] However, to date, the influence of alloy capping layers has primarily been investigated qualitatively using plan-view STM or

AFM.[4,5] Therefore, the quantitative structure of the buried dots has not been resolved. In terms of XSTM studies of this phenomenon, there has been one XSTM report on the influence of InGaAs and GaAsSb capping layers on dot size.[6] In addition, in another XSTM study, the influence of GaAs grown on top of InGaAs-capped InAs QDs was explored.[39] However, both XSTM studies did not include a comparison to dots capped with GaAs;[6,39] thus, the extent of the dot collapse due to capping with GaAs vs. InGaAs could not be compared. Furthermore, the influence of the alloy capping layers on the WL thickness was not considered. Thus, the effects of alloy layer capping on the dot sizes and wetting layer thickness remain unknown.

4.3 Experimental Details

The samples in this chapter were grown by Dr. J. D. Song and his group at the Korea Institute of Technology (KIST).[13] The details of the growth are presented in Appendix A. XSTM was used to investigate the influence of the alloy buffer and capping layers on dot formation and collapse. For XSTM, the samples were cleaved to expose a $(1\bar{1}0)$ surface as described in detail in Section 2.3 of this dissertation. Imaging was performed with commercially available Pt/Ir tips, which were cleaned in-situ by electron bombardment. We examined several high resolution images of the QD and AQD layers, spanning > 0.5 μm^2. All images in this chapter were obtained with a constant tunneling current of 0.15 nA and a sample bias of -2.0 V. To differentiate the GaAs, the QDs, and the clustered regions of the WL, we estimated the tip height criterion as explained in detail in Appendix B.[40]

4.4 Dot Dimensions, Density, and Wetting Layer Thickness

In this section, the influence of alloy layers on the shape, size, and density of QDs and AQDs and the corresponding WLs are presented. Large-scale XSTM topographic images of the QDs and AQDs are presented in Fig. 4.3, where the bright ellipses surrounded by darker layers correspond to InAs QDs in GaAs.[41] Furthermore, the WL between the QDs contains regions of In clustering, as indicated in Fig. 4.3(a), similar to that observed in previous XSTM studies of InAs/GaAs QDs grown by MBE.[18,42] The bright ellipses in Fig. 4.3 (b) correspond to a layer of AQDs. From Fig. 4.3, and several similar images, it is apparent that the dot sizes and the WL thicknesses are higher for the AQDs in comparison with the QDs.

To quantify the differences between the two types of dots, we applied the line-cut analysis described in Appendix B to the QDs and AQDs. The average dot width, dot height, and WL thickness are plotted in Fig. 4.4.[41] The QD dimensions are represented by solid circles while the AQD dimensions are represented by solid squares. The dots are typically ellipse-shaped, with major and minor axes corresponding to the reported dot widths and heights. The average QD diameters and heights are 16 ± 3 nm and 7 ± 1 nm, respectively, while the AQDs are larger with average diameters and heights of 22 ± 3 nm and 12 ± 2 nm, respectively. Thus, the diameters (heights) of the AQDs are 38% (71%) greater than those of the QDs. In addition, the WL between the QDs is 2.0 ± 0.8 nm thick whereas the WL between the AQDs is significantly thicker at 8 ± 2 nm. It is likely that intermixing with the surrounding GaAs diminished the QD dimensions and WL thickness, whereas intermixing with the $In_{0.2}Ga_{0.8}As$ alloy layers above and below the AQDs most likely lead to an increase in the AQD dimensions and WL thickness. These results suggest that the surrounding alloy layers influence the dot and WL dimensions, consistent with earlier reports, as discussed in Sections 4.2.3 and 4.2.4.

To infer dot densities, we also measured the average lateral spacing between the QDs and AQDs. The average lateral spacing between the QDs is 80 ± 21 nm whereas the average lateral spacing between the AQDs is 54 ± 12 nm, suggesting that the alloy buffer layer promoted an increase in dot density. Taking into account the reduction in mismatch strain provided by the InGaAs alloy layers at the buffer/dot and dot/cap interfaces, a strain-based mechanism for dot formation and collapse in the absence and presence of alloy layers is proposed in the following section.

4.5 Mechanism for Dot Formation and Collapse

The increase in dot density along with dot and WL dimensions in the presence of $In_{0.2}Ga_{0.8}As$ alloy layers is likely due to the alloy layer-induced reduction in mismatch strain at the buffer/dot and dot/cap interfaces. The targeted buffer/dot mismatch strain, ε, is 6.7% (ε_f = 7.2%) for the QDs and 5.4% (ε_f = 5.7%) for the AQDs. The targeted dot/cap mismatch strain is 7.2% (ε_f = 6.7%) for the QDs and 5.7% (ε_f = 5.4%) for the AQDs. In this section, we propose a strain-based mechanism for dot formation and collapse in the absence and presence of InGaAs alloy layers. This mechanism is likely to be applicable to a wide range of lattice-mismatched thin-film systems.

4.5.1 Mechanism for Dot Formation, Part I: Buffer Growth and Dot Nucleation

In Fig. 4.5, we propose a mechanism for dot formation in the absence and presence of InGaAs alloy buffer layers.[41] The diagrams on the left and right represent the growth stages and associated surface strain for the QDs and AQDs, respectively. The buffer layer growth is shown in Fig. 4.5(a) and Fig. 4.5(b). The initial InAs deposition leading to dot formation is depicted in Fig. 4.5(c) and Fig. 4.5(d). Finally, dot growth is shown in Fig. 4.5(e) and Fig. 4.5(f).

Initially, the "substrate" for the QDs is an unstrained GaAs buffer, as shown in Fig. 4.5(a), and the "substrate" for the AQDs is the strained $In_{0.2}Ga_{0.8}As$ alloy, as shown in Fig. 4.5(b). During the growth of the alloy buffer layer, the In diffuses laterally and segregates vertically, forming regions of varying [In] and surface strain on the growth surface, as illustrated in Fig. 4.5(b).[43] For QD growth directly on GaAs, shown in Fig. 4.5(c), a 2D WL, with strain distribution similar to that in Fig. 4.5(b), is observed initially. As discussed in Section 4.2.1, beyond a critical thickness which scales as $1/\varepsilon^2$, the wetting layer becomes unstable to surface perturbations, thereby allowing the formation of islands.[33,34] However, the alloy buffer layer acts as a "pre-existing" WL, so that when InAs is deposited on the alloy buffer, the In atoms nucleate to form dots in regions where the [In] is higher, as shown in Fig. 4.5(d). Therefore, the initial AQD density is expected to be higher than that of the QDs.

The final stages of InAs deposition likely proceeds as follows. As more InAs is deposited, QD nucleation occurs, and the QDs increase in size, as shown in Fig. 4.5(e). The compressive strain in the InAs layer is partially elastically relaxed by dot formation, leading to the lateral surface strain variation shown in Fig. 4.5(e), where the edges of the dot are under higher compressive strain than the top surface of the dot. With additional InAs deposition, the AQDs also increase in size, as discussed in section 4.2.1 and as shown in Fig. 4.5(f). However, at the surface, the compressive strain on the surface is lower for the AQDs than the QDs due to the lower buffer/dot mismatch strain.

4.5.2 Mechanism for Dot Formation, Part II: Cap Growth and Dot Collapse

In Fig. 4.6, a mechanism for dot collapse in the absence and presence of InGaAs alloy capping layers is proposed.[41] The diagrams on the left and right represent the growth stages and associated surface strain for the QDs and AQDs respectively. The early stages of capping are shown in Fig. 4.6(a) and Fig. 4.6(b). Intermixing after additional capping is depicted in Fig. 4.6(c) and Fig. 4.6(d), and the final dot structures after capping are represented in Fig. 4.6(e) and Fig. 4.6(f).

As the QDs are capped with GaAs, Ga preferentially accumulates in regions of highest compressive strain such as the QD edges as shown in Fig. 4.6(a). With increasing cap thickness, the high compressive dot/cap mismatch strain at the dot base facilitates the diffusion of In atoms away from the QD, leading to QD collapse, as shown in Fig. 4.6(c).[4] On the other hand, as the AQDs are capped with $In_{0.2}Ga_{0.8}As$, In adatoms preferentially attach at the regions of the lowest compressive strain, namely on the top surface of the dot, as shown in Fig. 4.6(b). Thus, $In_{0.2}Ga_{0.8}As$ accumulates both on top of and at the edges of the AQDs. The In from the surrounding alloy layers diffuses into the AQDs and WL, leading to an increase in dot dimensions and WL thickness, as illustrated in Fig. 4.6(d). Thus, for the QDs, the increase in dot size and WL thickness is limited, as shown in Fig. 4.6(e). Conversely, for the AQDs, the surrounding alloy layers promote an increase in dot and WL dimensions, as shown in Fig. 4.6(f).

Our model suggests that lattice-mismatch strain is influencing the In-Ga interdiffusion at the buffer/dot and dot/cap interfaces. Previous studies of lattice-matched InGaAs/InAlAs quantum wells revealed significant In diffusion, attributed to a difference in the mobility between the Ga and Al atoms, which apparently promoted an In chemical potential gradient across the interface.[44-46] However, in those studies, temperatures > 700 °C were necessary to initiate the interdiffusion. Since the growth temperature for the sample examined here is 480°C, and a large buffer-dot and dot-cap lattice-mismatch exists, it is likely that lattice-mismatch strain is dominating the interdiffusion between the dots and the surrounding buffer and capping layers. Furthermore, due to the difference in size between the In and Ga atoms, the contribution of strain to the interdiffusion process for the InAs/GaAs system cannot be ignored.

4.6 Conclusions

In summary, we have investigated the influence of InGaAs alloy layers on the diameter, height, shape, and density of InAs dots, as well as the thickness of the surrounding WLs. For both QDs and AQDs, XSTM images reveal uncoupled ellipse-shaped dots. The lateral spacing between the AQDs is lower than the lateral spacing between the QDs, suggesting that the alloy buffer layer promotes an increase in dot density. Furthermore, the alloy buffer and capping layers reduce the tendency for dot collapse, and the diffusion of In from the alloy layers surrounding the WL leads to an increase in the apparent WL thickness. These results provide a valuable understanding of the relationship between growth conditions and structure of semiconductor QDs.

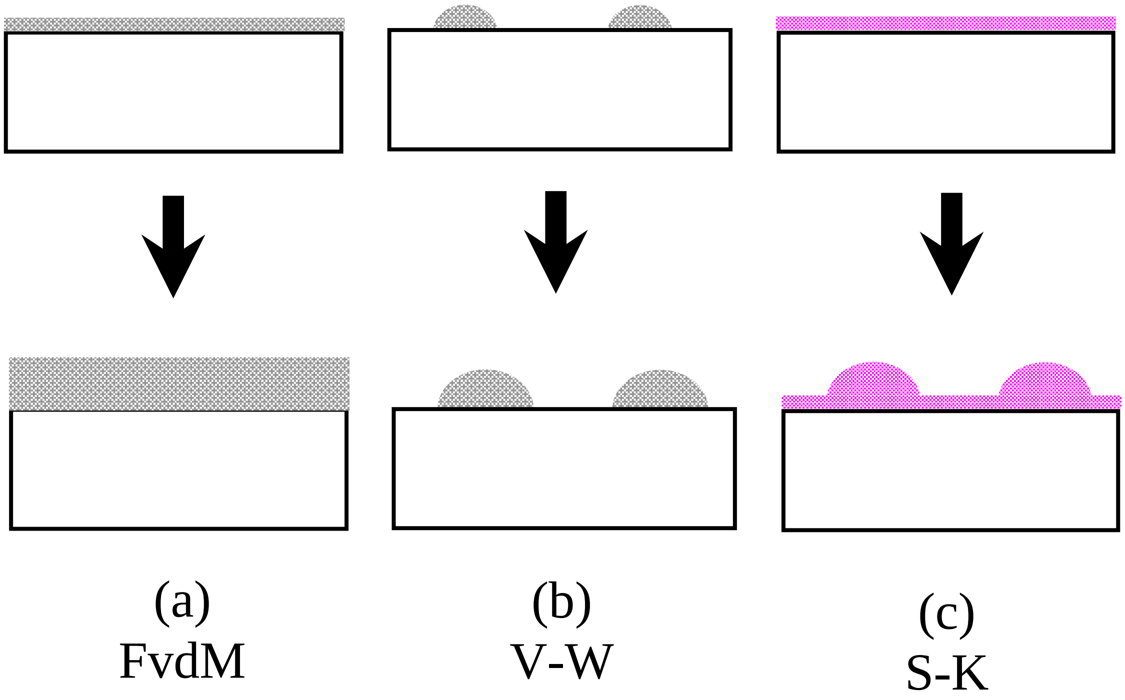

Fig. 4.1: Epitaxial growth modes: (a) layer-by-layer growth: Frank-van der Merwe (FvdM), (b) island growth: Volmer-Weber (V-W), and (c) layer-by-layer growth followed by a transition to island growth: Stranski-Krastanow (S-K).[23]

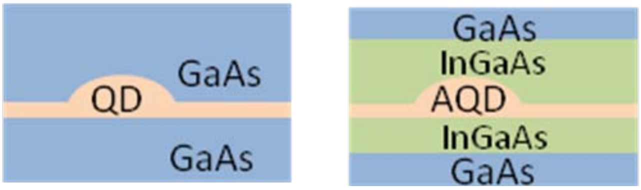

$\varepsilon_{QD} > \varepsilon_{AQD}$

Critical WL thickness: $h_c \sim \frac{1}{\varepsilon^2}$	–	+
Maximum dot volume: $V_C \sim \frac{1}{\varepsilon^6}$	–	+

Fig. 4.2: Dependence of critical WL thickness and maximum dot volume on mismatch strain for the QDs and AQDs. The critical WL thickness and maximum dot volume are higher for the AQDs than for the QDs.

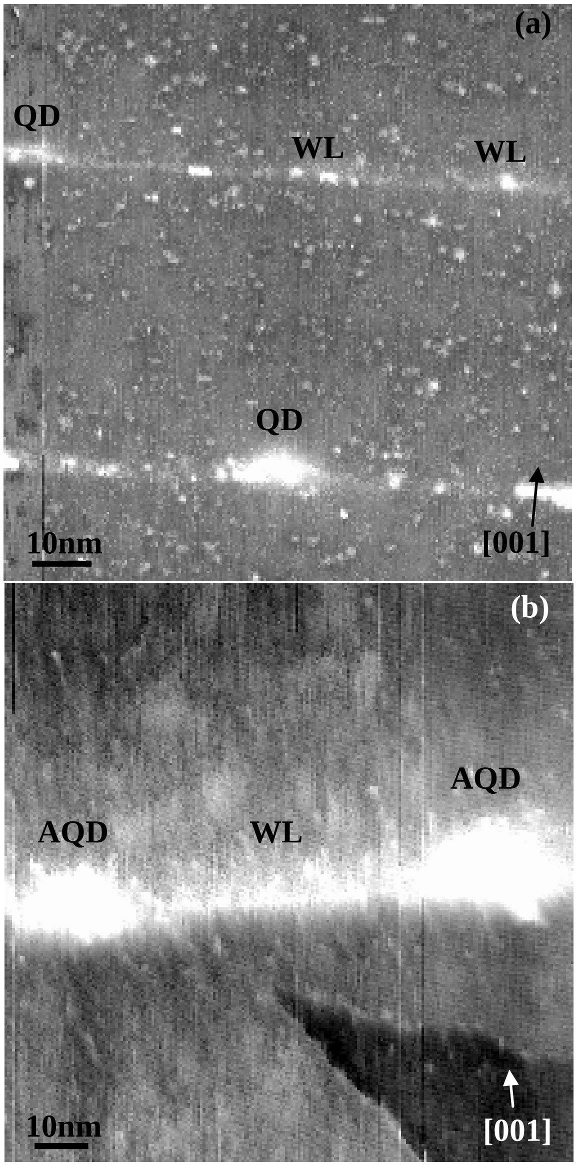

Fig. 4.3: Large-scale topographic XSTM images acquired at a sample bias of -2.0 V, with bright regions corresponding to InAs in a GaAs matrix. (a) QDs: 3 ML InAs dots in a GaAs matrix. The gray-scale range displayed is 0.7 nm. (b) AQDs: 3 ML InAs dots grown between a 1.25 nm of $In_{0.2}Ga_{0.8}As$ buffer, and a 7.5 nm of $In_{0.2}Ga_{0.8}As$ capping layer. The gray-scale range displayed is 0.8 nm. The observed periodicity is an artifact due to the lock-in amplifier that was powered during the image acquisition. The dot dimensions and WL thickness are greater for the AQDs in comparison to that of the QDs. Reprinted with permission from Ref. 41.[41] Copyright 2009, American Institute of Physics.

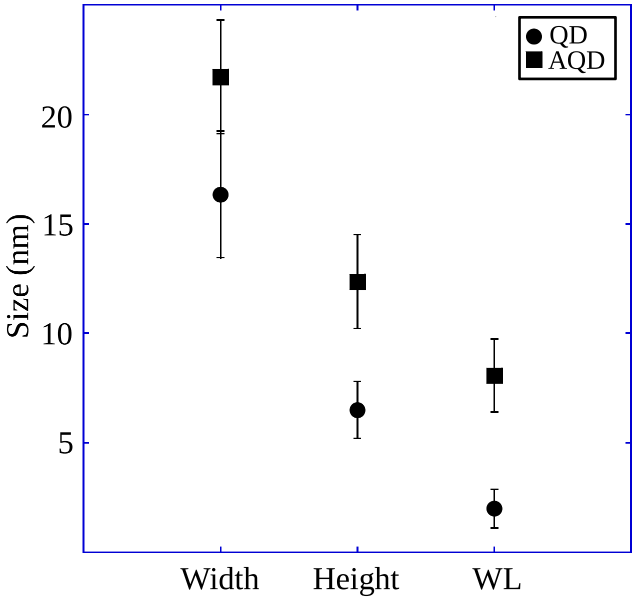

Fig. 4.4: Comparison of width, height, and WL thickness for the QDs and AQDs. These values are based upon line-cut analyses from high resolution XSTM images of the QDs and AQDs. Reprinted with permission from Ref. 41.[41] Copyright 2009, American Institute of Physics.

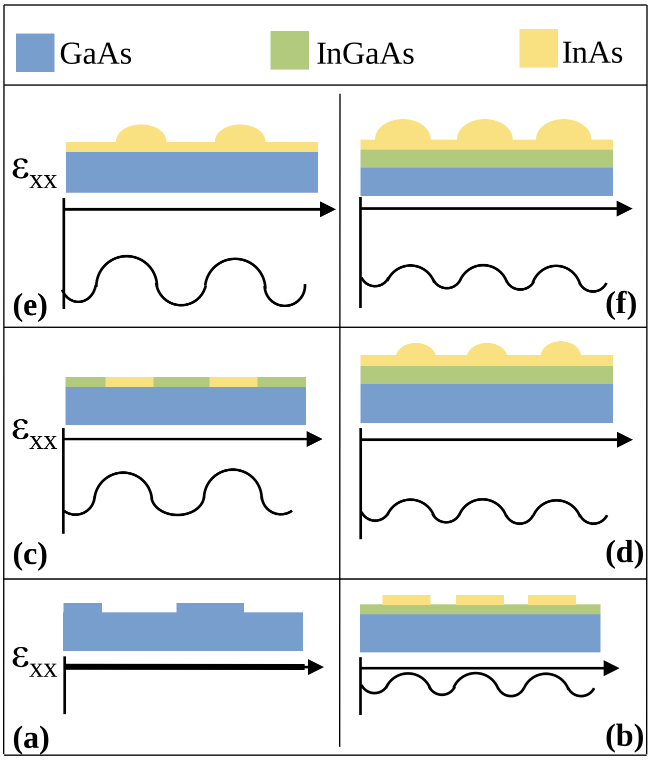

Fig. 4.5: Mechanism for dot formation in the absence and presence of InGaAs alloy layers, Part I: buffer layer growth prior to InAs deposition for the (a) QDs and (b) AQDs; initial stages of InAs deposition for the (c) QD layers and (d) AQD layers; dot nucleation for the (e) QD layers and (f) AQD layers. Reprinted with permission from Ref. 41.[41] Copyright 2009, American Institute of Physics.

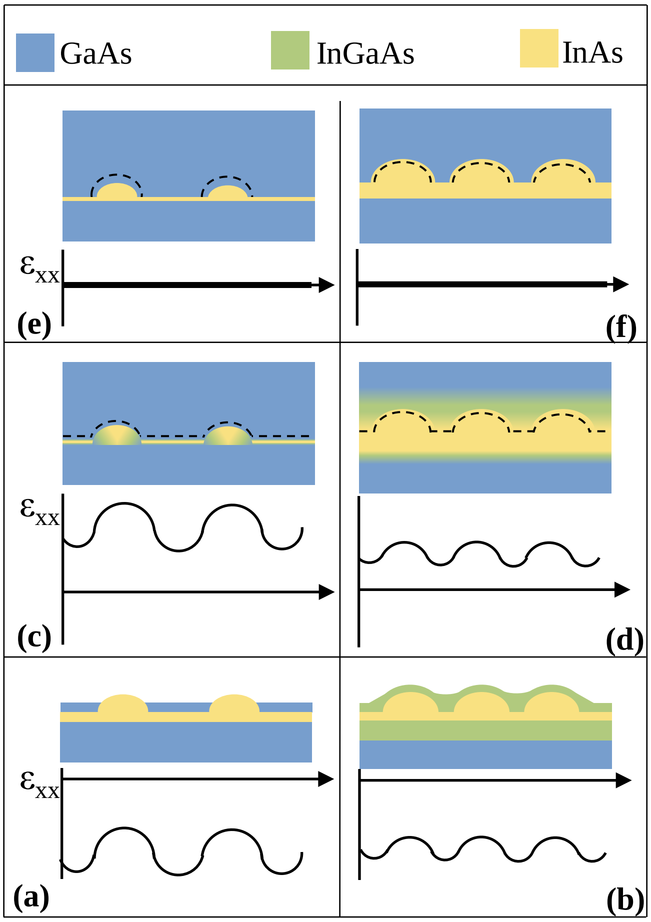

Fig. 4.6: Mechanism for dot formation in the absence and presence of InGaAs alloy layers, Part II: initial stages of capping with (a) GaAs for the QDs and (b) $In_{0.2}Ga_{0.8}As$ for the AQDs; additional capping and intermixing for the (c) QDs and (d) AQDs, and final capped structures of the (e) QDs and (f) AQDs. The dotted line represents the dot height prior to capping. Reprinted with permission from Ref. 41.[41] Copyright 2009, American Institute of Physics.

4.7 References

[1] H. Y. Liu, M. Hopkinson, C. N. Harrison, M. J. Steer, R. Frith, I. R. Sellers, D. J. Mowbray, and M. S. Skolnick, Journal of Applied Physics **93**, 2931 (2003).

[2] A. Stintz, G. T. Liu, A. L. Gray, R. Spillers, S. M. Delgado, and K. J. Malloy, Journal of Vacuum Science and Technology B **18**, 1496 (2000).

[3] J.-I. Chyi, T.-E. Nee, C.-T. Lee, J.-L. Shieh, and J.-W. Pan, Journal of Crystal Growth **175-176**, 777 (1997).

[4] R. Songmuang, S. Kiravittaya, and O. G. Schmidt, Journal of Crystal Growth **249**, 416 (2003).

[5] G. Costantini, A. Rastelli, C. Manzano, P. Acosta-Diaz, R. Songmuang, G. Katsaros, O. Schmidt, and K. Kern, Physical Review Letters **96** (2006).

[6] J. M. Ulloa, C. Celebi, P. M. Koenraad, A. Simon, E. Gapihan, A. Letoublon, N. Bertru, I. Drouzas, D. J. Mowbray, M. J. Steer, and M. Hopkinson, Journal of Applied Physics **101**, 081707 (2007).

[7] Y. Horikoshi, M. Kawashima, and H. Yamaguchi, Japanese Journal of Applied Physics **25**, L868 (1986).

[8] G. M. Guryanov, G. E. Cirlin, V. N. Petrov, N. K. Polyakov, A. O. Golubok, S. Y. Tipissev, V. B. Gubanov, Y. B. Samsonenko, N. N. Ledentsov, V. A. Shchukin, M. Grundmann, D. Bimberg, and Z. I. Alferov, Surface Science **352-354**, 651 (1996).

[9] G. E. Cirlin, V. N. Petrov, V. G. Dubrovskii, A. O. Golubok, S. Y. Tipissev, G. M. Guryanov, M. V. Maximov, N. N. Ledentsov, and D. Bimberg, Czechoslovak Journal of Physics **47**, 379 (1997).

[10] A. Bosacchi, P. Frigeri, S. Franchi, P. Allegri, and V. Avanzini, Journal of Crystal Growth **175-176**, 771 (1997).

[11] W. Cheng, Z. Zhong, Y. Wu, Q. Huang, and J. Zhou, Journal of Crystal Growth **183**, 279 (1998).

[12] Y. Horikoshi, Journal of Crystal Growth **201-202**, 150 (1999).

[13] J. D. Song, Y. M. Park, J. C. Shin, J. G. Lim, Y. J. Park, W. J. Choi, I. K. Han, J. I. Lee, H. S. Kim, and C. G. Park, Journal of Applied Physics **96**, 4122 (2004).

[14] G. S. Solomon, W. Wu, J. R. Tucker, and J. S. Harris, Jr., Physica E **2**, 709 (1998).

[15] W. Wu, J. R. Tucker, G. S. Soloman, and J. S. Harris, Jr., Applied Physics Letters **71**, 1083 (1997).

[16] L. Ouattara, A. Mikkelsen, E. Lundgren, L. Hoglund, C. Asplund, and J. Y. Andersson, Journal of Applied Physics **100**, 44320 (2006).

[17] X.-D. Wang, N. Liu, C. K. Shih, S. Govindaraju, and A. L. Holmes Jr., Applied Physics Letters **85**, 1356 (2004).

[18] B. Lita, R. S. Goldman, J. D. Phillips, and P. K. Bhattacharya, Applied Physics Letters **75**, 2797 (1999).

[19] T. Haga, M. Kataoka, N. Matsumura, S. Muto, Y. Nakata, and N. Yokoyama, Japanese Journal of Applied Physics **36**, L1113 (1997).

[20] P. B. Joyce, T. J. Krzyzewski, G. R. Bell, B. A. Joyce, and T. S. Jones, Physical Review B **58**, R15981 (1998).

[21] A. Rosenauer, D. Gerthsen, D. V. Dyck, M. Arzberger, G. Böhm, and G. Abstreiter, Physical Review B **64**, 245334 (2001).

[22] T. Maltezopoulos, A. Bolz, C. Meyer, C. Heyn, W. Hansen, M. Morgenstern, and R. Wiesendanger, Physical Review Letters **91**, 196804 (2003).

[23] D. Bimberg, M. Grundmann, and N. N. Ledentsov, *Quantum Dot Heterostructures*. (John Wiley & Sons, 1999).

[24] J. A. Venables, *Introduction to Surface and Thin Film Processes*. (Cambridge University Press, Cambridge, 2000).

[25] D. J. Eaglesham and M. Cerullo, Physical Review Letters **64**, 1943 (1990).

[26] Y.-W. Mo, D. E. Savage, B. S. Swartzentruber, and M. G. Lagally, Physical Review Letters **65**, 1020 (1990).

[27] V. Le Thanh, P. Boucaud, D. Débarre, Y. Zheng, D. Bouchier, and J.-M. Lourtioz, Physical Review B **58**, 13115 (1998).

[28] D. Leonard, M. Krishnamurthy, C. M. Reaves, S. P. Denbaars, and P. M. Petroff, Applied Physics Letters **63**, 3203 (1993).

[29] J. M. Moison, F. Houzay, F. Barthe, L. Leprince, E. Andre, and O. Vatel, Applied Physics Letters **64**, 196 (1994).

[30] F. Houzay, C. Guille, J. M. Moison, P. Henoc, and F. Barthe, Journal of Crystal Growth **81**, 67 (1987).

[31] J. Tersoff, Physical Review Letters **81**, 3183 (1998).

[32]F. Tinjod and H. Mariette, Physica Status Solidi B **241**, 550 (2004).

[33]Y. Tu and J. Tersoff, Physical Review Letters **93**, 216101 (2004).

[34]H. R. Eisenberg and D. Kandel, Physical Review Letters **85**, 1286 (2000).

[35]J. Tersoff and F. K. LeGoues, Physical Review Letters **72**, 3570 (1994).

[36]T. Nishinaga, T. Shitara, K. Mochizuki, and K. I. Cho, Journal of Crystal Growth **99**, 482 (1990).

[37]Y. Kangawa, T. Ito, A. Taguchi, K. Shiraishi, T. Irisawa, and T. Ohachi, Applied Surface Science **190**, 517 (2002).

[38]G. S. Solomon, J. A. Trezza, and J. Harris, J. S., Applied Physics Letters **66**, 991 (1995).

[39]A. Lenz, H. Eisele, R. Timm, L. Ivanova, H.-Y. Liu, M. Hopkinson, U. W. Pohl, and M. Dahne, Physica E **40**, 1988 (2008).

[40]V. D. Dasika, R. S. Goldman, J. D. Song, W. J. Choi, N. K. Cho, and J. I. Lee, Journal of Applied Physics **106**, 014315 (2009).

[41]V. D. Dasika, J. D. Song, W. J. Choi, N. K. Cho, J. I. Lee, and R. S. Goldman, Applied Physics Letters **95** (2009).

[42]B. Shin, B. Lita, R. S. Goldman, J. D. Phillips, and P. K. Bhattacharya, Applied Physics Letters **81**, 1423 (2002).

[43]T. Walther, A. G. Cullis, D. J. Norris, and M. Hopkinson, Physical Review Letters **86**, 2381 (2001).

[44]R. J. Baird, T. J. Potter, R. Lai, G. P. Kothiyal, and P. K. Bhattacharya, Applied Physics Letters **53**, 2302 (1988).

[45]R. E. Mallard, N. J. Long, G. R. Booker, E. G. Scott, M. Hockly, and M. Taylor, Journal of Applied Physics **70**, 182 (1991).

[46]C. S. Peng, H. F. Liu, T. Jouhti, E.-M. Pavelescu, J. Konttinen, and M. Pessa, IEEE Proceedings on Optoelectronics **150**, 36 (2003).

Chapter 5

Quantum Dot Electronic States

5.1 Overview

Advances in quantum dot (QD) devices will require an understanding of the influence of variations in QD shape, composition, and strain on the electronic states. In this chapter, investigations of the origins of electronic states in individual (uncoupled) QDs and the surrounding wetting layers (WLs), are presented. Room temperature scanning tunneling spectroscopy (STS) spectra reveal a gradient in the effective bandgap within the QDs with smallest values near the QD core and top surfaces. The variations in effective bandgap are apparently dominated by indium composition gradients, with minimal effects due to QD shape and strain. Indium composition gradients also dominate the effective bandgap variations in the WL.

This chapter begins with a brief review of prior work concerning the measurement of compositional variations and effective bandgaps in QDs and the surrounding WLs. The experimental details are then described. Next, we describe investigations of the effective bandgap variation across several individual, uncoupled, QDs and in the WL, respectively. Using a combination of cross-sectional scanning tunneling microscopy (XSTM) and STS, we find decreases in the effective bandgap both laterally and vertically (in the growth direction). These trends are consistent with an increase in [In] toward the center and top of the QD. Similar trends were also observed in the WL. This work was supported in part by the Army Research Office Multidisciplinary University Research Initiative under Grant No. ARO-MURI DAAD19-01-1-0462 and by the Department of Energy under Grant No. DE-FG02-06ER46339, monitored by J. Zhu.

5.2 Background

In this section, a brief summary of prior work on the compositional variations in QDs and the WL is presented, along with prior STS measurements of the QD effective bandgap.

A number of reports have suggested that QDs often have non-uniform compositions across their width[1,2] and height[1-6] due to indium (In) segregation and inter-diffusion at the interface between the GaAs and InAs layers. These reports suggest that the lateral [In] is highest at the QD core and that the vertical [In] increases in the growth direction. The regions between the QDs, the so-called wetting layers (WLs), contain sparse concentrations of individual In atoms which have not agglomerated to form a 3D island.[7] The WLs are typically 2D inhomogeneous films with significant [In] gradients, including vertical In segregation and lateral In clustering.[6-9]

To date, the effect of compositional variations on the QD and WL electronic states remains unknown. Although one cross-sectional STS study of molecular beam epitaxially (MBE)-grown QDs revealed a variation in QD effective bandgap in the growth direction,[12] any corresponding lateral variations in effective bandgap were not considered. Thus, the origins of the effective bandgap variations have not been identified.

5.3 Experimental Details

The QD samples in this chapter were grown by Dr. J. D. Song and his group at the Korea Institute of Technology (KIST).[13,14] The growth details are presented in Appendix A.

XSTM and STS measurements were used to investigate the origins of electronic states in the QDs. For XSTM, the samples were prepared as described in Section 2.3. STS measurements were performed using the variable tip-sample separation method,[15] described in Section 2.4. We examined several high resolution images of the QDs spanning > $0.5\mu m^2$ and acquired STS spectra from more than 70 QDs. To differentiate the GaAs, the QDs, and the clustered regions of the WL, we used the tip height criterion described in Appendix B.[16]

5.4 Uncoupled QDs

In this section, we report on the effective bandgap variations across individual, uncoupled QDs. An example large-scale XSTM topographic image of the QDs and the surrounding WL is shown in Fig. 5.1. In Fig. 5.1, the bright ellipses surrounded by darker layers correspond to InAs dots in GaAs. Due to the relatively thick (50 nm) spacer layer between the QDs, the dots are uncorrelated, similar to earlier reports.[17]

Furthermore, the WL contains regions of significant In clustering, which are labeled with dashed lines on the image.

Figure 5.3(a) shows an example XSTM image where the bright ellipse, with major and minor axes of 16 nm and 6 nm respectively, corresponds to an InAs QD in a GaAs matrix. In Fig. 5.3(b), the normalized conductance versus sample bias voltage is plotted for the edge and center of the QD shown in Fig. 5.3(a), in comparison with a region of clean GaAs. The GaAs spectrum, shown at the bottom of Fig. 5.3(b), displays well-defined band edges, with a bandgap of 1.45 eV, similar to that of bulk GaAs at room temperature. The measured bandgap is slightly larger than the predicted 1.42 eV, likely due to tip induced band bending.[15,18] In Fig. 5.3(b), at the edge of the QD, the effective bandgap is 1.09 eV (plot 1), while at the QD core, the effective bandgap is 0.87 eV (plot 2). Thus, a gradient in the effective bandgap is observed, with the effective bandgap decreasing laterally toward the QD core. A similar trend was observed in a real-space computational study using a moments-based tight-binding method, with a STM image contrast algorithm to determine the atom types and positions.[19] In that study, the computations suggested a variation in the effective bandgap within the QD, with the narrowest bandgap near the QD center as shown in Fig. 5.2(d), consistent with the STS data (collected by the author) shown in Fig. 5.2(c). However, for the computations, we assumed a QD composed of pure InAs, and only lateral variations in effective bandgap were considered.

To gain a more thorough understanding of the effective bandgap variation within and between QDs, we measured the effective bandgap both laterally and vertically across QDs. Thus, spatially-resolved STS spectra were collected from several ellipse-shaped

QDs with 14 ± 1 nm major axes. The plots of normalized conductance vs. energy, such as that shown in Fig. 5.3(b), were then used to determine the energetic positions of the effective valence and conduction band edges, which presumably correspond to the lowest confined hole (E_h) and electron (E_e) levels respectively. In Fig. 5.4(a) and Fig. 5.4(b), average values of E_h and E_e as a function of the lateral and vertical position within a QD are plotted as solid circles.

In a QD, due to confinement, the lowest confined electron and hole levels are expected to be higher in energy than the band edges of a bulk semiconductor. Thus, the measured E_e and E_h for an InGaAs/GaAs QD are expected to be larger than the corresponding values for a bulk-like InGaAs alloy. However, for a given materials system, similar trends are expected for both the bulk-like alloy and the quantum-confined structure. Thus, using the In composition gradients reported previously for similar-sized QDs,[2,6] the lateral and vertical band-edge variation for an undoped bulk-like InGaAs alloy (without quantum confinement) was estimated, and plotted as a solid line in Fig. 5.4.

The lateral variations in QD effective bandgap are shown in Fig. 5.4(a). In this case, the effective bandgap is narrowest at the QD center. Since the InAs/GaAs lattice-mismatch strain is predicted to increase the lateral effective bandgap towards the QD core,[20] as shown in Fig. 5.5(c), it is unlikely that strain is dominating the lateral effective bandgap variation. Given that the QD is widest at the center, and the [In] is expected to be highest at the QD center, it is possible that lateral variations in the well width and/or [In] in the QD are dominating the lateral effective bandgap variation.[1,2]

The vertical variations in the QD effective bandgap are shown in Fig. 5.4(b). Here, the effective bandgap is narrowest at the top of the QD. The QDs are wider at the center, and the InAs/GaAs lattice-mismatch strain is predicted to increase the effective bandgap for a 0D structure in the growth direction.[20,21] As shown in Fig. 5.5(d), it is unlikely that strain or vertical variations in the well width are dominating the effective bandgap variation in the growth direction. Since both the lateral and vertical variations of the effective conduction and valence band edges follow the trend of the In-composition gradient induced band-edge variations, it is likely that [In] variations dominate the effective bandgap variations. Furthermore, since both the lateral and vertical variations of the effective conduction and valence band edges follow the trend of the In-composition gradient induced band-edge variations, it is likely that [In] variations dominate the effective bandgap variations in the QD.

5.5 Wetting Layer

We also examined the lateral and vertical variations in effective bandgap of the WL, as shown in Fig. 5.6. The WLs typically exhibit [In] gradients due to interdiffusion and surface segregation, and contain sparse concentrations of individual In atoms which have not agglomerated to form a 3D island.[7,9-11] Regions of significant In clustering were identified using the procedure described in Appendix B, and STS spectra were collected both laterally and vertically across the WL regions with significant In clustering. The normalized conductance was used to estimate the energetic positions of the effective valence and conduction band edges, using the analysis described in Section 2.4. The resulting effective bandgap variations as a function of position within the WL laterally and vertically are shown in Fig. 5.6(a) and 5.6(b) respectively. In the plot, ‘0’ marks the edge of a clustered region. The measured effective bandgap in the WL was linearly corrected for tip induced band bending by multiplying the measured value for E_e and E_h by a correction factor which would produce a GaAs bandgap of 1.42 eV, as described in Appendix C. For comparison, the band edges for bulk $In_xGa_{1-x}As$ were calculated using x values from previous XSTM and TEM studies of the WL,[6] and plotted in Fig. 5.6 as a solid line.

Laterally, the effective bandgap decreases towards the center of the cluster, where the [In] is presumably the highest,[7-9] similar to the trend observed within the QDs, discussed in Section 5.4. Vertically, there is limited variation in the [In],[6,10] and correspondingly, the variation in effective bandgap is also limited, and is approximately equal to 1.31 ± 0.01 eV. Thus, the lateral and vertical variations in the [In] dominate the effective bandgap in the WL as well as in the QDs.

5.6 Conclusions

In summary, we have used variable separation STS to examine nanoscale variations in the effective bandgap within InAs/GaAs QDs and the clustered regions of the WL. The data reveal variations in the effective band gap across individual QDs both laterally and in the growth direction. Laterally, the effective bandgap decreases toward the QD core and vertically, the effective bandgap decreases in the growth direction. These results are consistent with an increase in [In] toward the center and top of the QD, suggesting that [In] variations dominate the variations in QD effective bandgap. Similarly, in the clustered regions of the WL, [In] variations dominate the variations in the WL effective bandgap. Thus, the variations in effective bandgap are apparently dominated by In composition gradients, with minimal effects due to QD shape and strain.

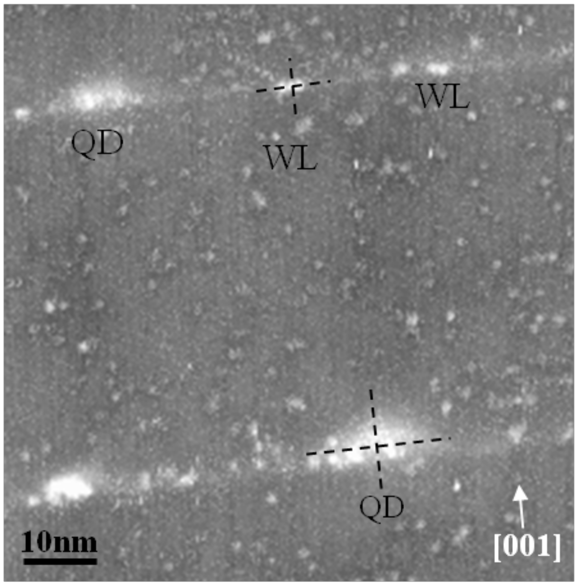

Fig. 5.1: Large-scale XSTM topographic image of the uncoupled InAs/GaAs QDs, with bright regions corresponding to InAs. WL regions with significant In clustering are labeled. The image was acquired at a sample bias of -2.0 V. The gray-scale range displayed is 0.7 nm. The QDs and the clustered regions of the WL are indicated by the dashed lines near the top and bottom of the image. Reprinted with permission from Ref 17.[16] Copyright 2009, American Institute of Physics.

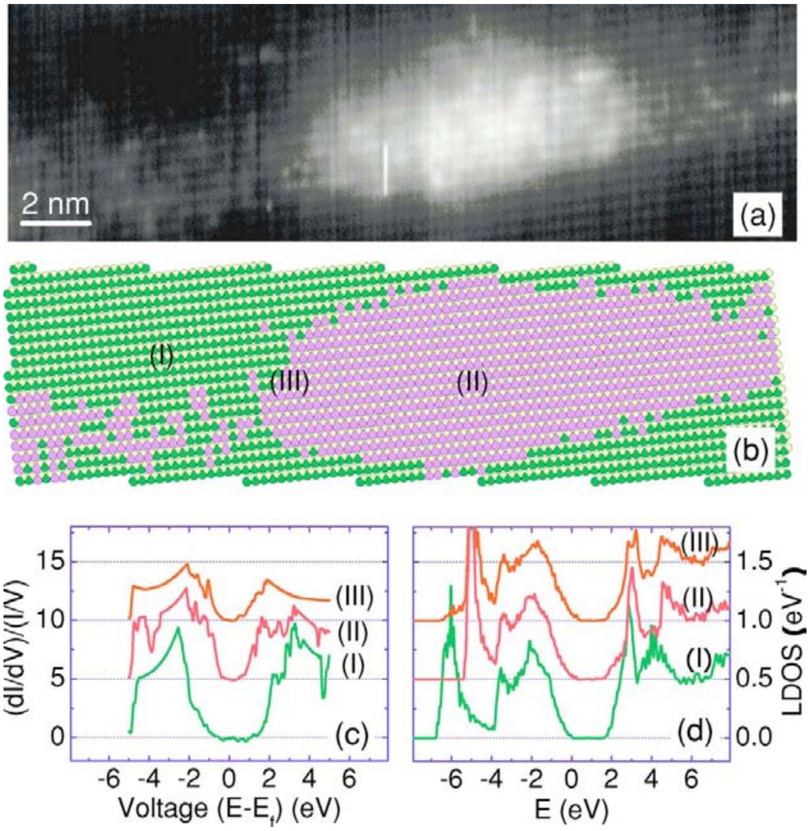

Fig. 5.2: (a) Atomic resolution XSTM image of an InAs/GaAs QD. The bright region is the QD and the dark is the GaAs buffer. (b) The atomic structure of the QD determined from the STM image. The LDOS of (I) the Ga atom in the buffer, (II) an In atom in the QD, and (III) an In atom near the interface from (c) the experimental STS spectra collected by the author and (d) the computational studies at UIUC. Reprinted with permission from Ref 20.[19] Copyright 2006, American Institute of Physics.

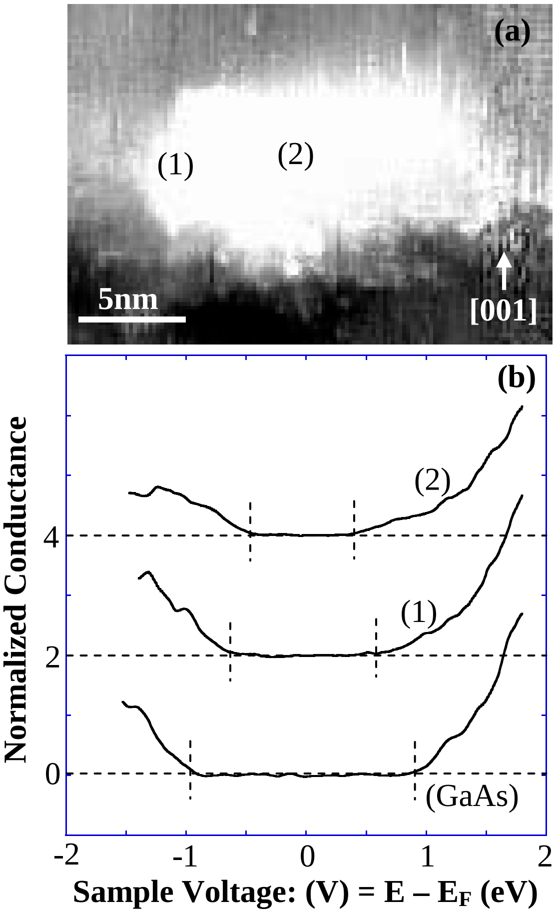

Fig. 5.3: (a) XSTM topographic image acquired at a sample bias of -2.0V. The gray-scale range displayed is 1 nm. In (b), spatially resolved STS spectra from points (1) and (2) are plotted in comparison with a region of clean GaAs. The effective valence and conduction band edges are indicated by vertical dashed lines at negative and positive sample voltages, respectively. The sample voltage corresponds to the energy relative to the Fermi level. Reprinted with permission from Ref 17.[16] Copyright 2009, American Institute of Physics.

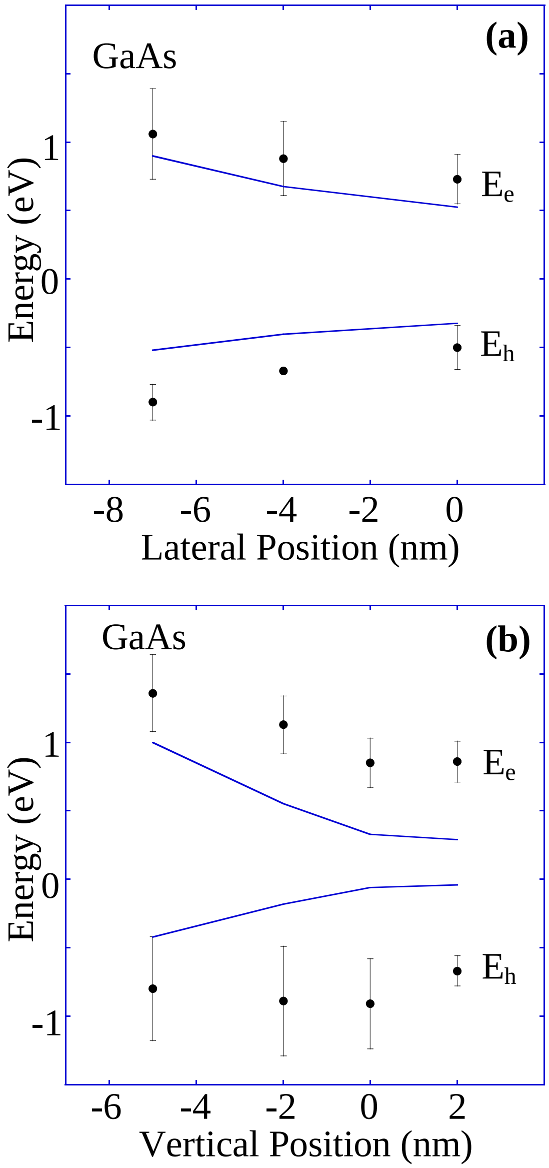

Fig. 5.4: Spatial variations in the energies of the effective conduction and valence band edges in the GaAs and QD in the (a) horizontal and (b) vertical directions, with respect to the QD center. The calculated $In_xGa_{1-x}As$ band edges with x=0.35 at the QD edge, x=0.65 at the QD core, x=0.6 at the QD bottom, and x=0.9 at the QD top surface are indicated by the solid line. The x values were determined from XSTM measurements of [In] across similarly-sized QDs.[2] Reprinted with permission from Ref 17.[16] Copyright 2009, American Institute of Physics.

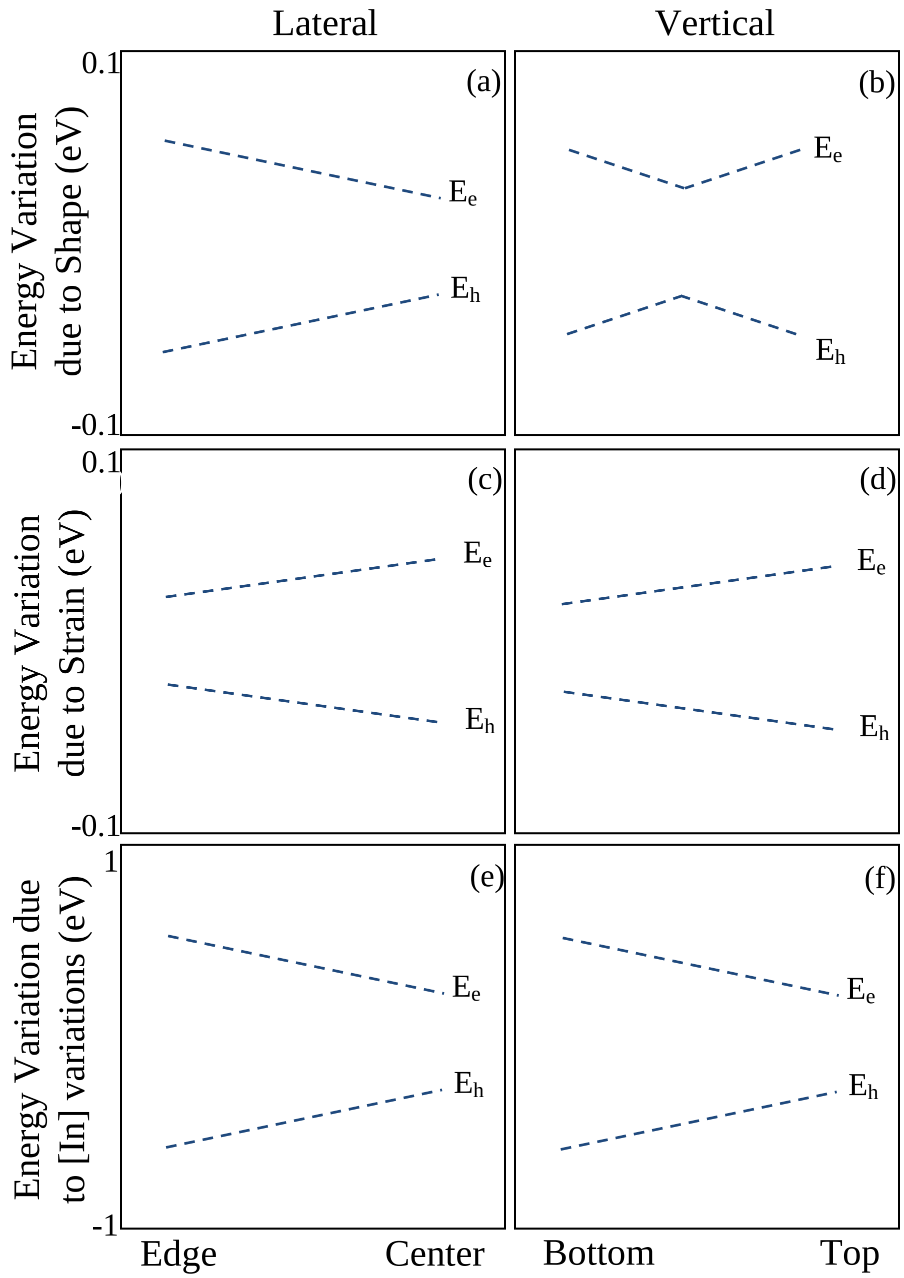

Fig. 5.5: Predicted trends in QD effective bandgap variation due to shape ((a),(b)), strain ((c),(d)), and [In] variations ((e),(f)). (a) Laterally, the QD is wider at the center than at the edges; thus, the effective bandgap is expected to decrease towards the QD center. (b) Vertically, the effective bandgap is expected to be narrowest towards the center of the QD. (c) Laterally, the bandgap is predicted to decrease towards the edges of the QD. (d) Vertically, strain is expected to increase the bandgap towards the top surface of the QDs. (e) Laterally, the [In] is highest towards the center of the QD, and thus, the effective bandgap decreases towards the QD center. (f) Vertically, the [In] is highest near the top surface of the QD; thus, the calculated effective bandgap decreases towards the top of the QD.

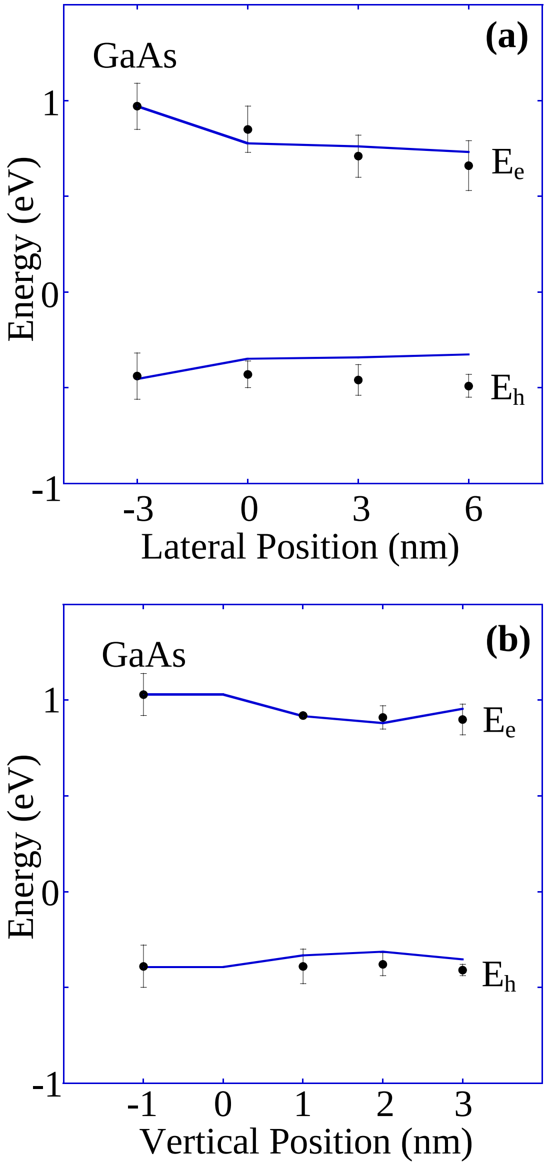

Fig. 5.6: Spatial variations in the energies of the effective conduction and valence band edges in the WL (a) laterally and (b) vertically with respect to the WL edge. The calculated $In_xGa_{1-x}As$ band edges with x=0.26 at the edge of the WL clustered region, x=0.32 at center, x=0.15 at the bottom of the clustered region, and x=0.10 at the top surface is indicated by the solid line. The x values were determined from XSTM and TEM measurements of [In] across the WL between QDs.[6]

5.7 References

[1]N. Liu, J. Tersoff, O. Baklenov, A. L. Holmes, Jr, and C. K. Shih, Physical Review Letters **84**, 334 (2000).

[2]A. Lenz, R. Timm, H. Eisele, C. Hennig, S. K. Becker, R. L. Sellin, U. W. Pohl, D. Bimberg, and M. Dahne, Applied Physics Letters **81**, 5150 (2002).

[3]A. Urbieta, B. Grandidier, J. P. Nys, D. Deresmes, D. Stievenard, A. Lemaitre, G. Patriarche, and Y. M. Niquet, Physical Review B **77**, 155313 (2008).

[4]P. B. Joyce, T. J. Krzyzewski, G. R. Bell, B. A. Joyce, and T. S. Jones, Physical Review B **58**, R15981 (1998).

[5]A. Lemaitre, G. Patriarche, and F. Glas, Applied Physics Letters **85**, 3717 (2004).

[6]P. Wang, A. L. Bleloch, M. Falke, P. J. Goodhew, J. Ng, and M. Missous, Applied Physics Letters **89**, 072111 (2006).

[7]T. R. Ramachandran, A. Madhukar, I. Mukhametzhanov, R. Heitz, A. Kalburge, Q. Xie, and P. Chen, Journal of Vacuum Science and Technology B **16**, 1330 (1998).

[8]B. Shin, B. Lita, R. S. Goldman, J. D. Phillips, and P. K. Bhattacharya, Applied Physics Letters **81**, 1423 (2002).

[9]G. Sek, K. Ryczko, M. Motyka, J. Andrzejewski, K. Wysocka, J. Misiewicz, L. H. Li, A. Fiore, and G. Patriarche, Journal of Applied Physics **101**, 63539 (2007).

[10]B. Lita, R. S. Goldman, J. D. Phillips, and P. K. Bhattacharya, Surface Review Letters **7**, 539 (2000).

[11]P. Offermans, P. M. Koenraad, R. Notzel, J. H. Wolter, and K. Pierz, Applied Physics Letters **87**, 111903 (2005).

[12]D. M. Bruls, J. W. A. M. Vugs, P. M. Koenraad, M. S. Skolnick, M. Hopkinson, and J. H. Wolter, Applied Physics A **72**, S205 (2001).

[13]J. D. Song, Y. M. Park, J. C. Shin, J. G. Lim, Y. J. Park, W. J. Choi, I. K. Han, J. I. Lee, H. S. Kim, and C. G. Park, Journal of Applied Physics **96**, 4122 (2004).

[14]N. K. Cho, S. P. Ryu, J. D. Song, W. J. Choi, J. I. Lee, and H. Jeon, Applied Physics Letters **88**, 133104 (2006).

[15]R. M. Feenstra, Physical Review B **50**, 4561 (1994).

[16]V. D. Dasika, R. S. Goldman, J. D. Song, W. J. Choi, N. K. Cho, and J. I. Lee, Journal of Applied Physics **106**, 014315 (2009).

[17]X.-D. Wang, N. Liu, C. K. Shih, S. Govindaraju, and A. L. Holmes Jr., Applied Physics Letters **85**, 1356 (2004).

[18]O. Madelung, *Semiconductors - Basic Data*. (Springer-Verlag, 1996).

[19]J. Q. Lu, H. T. Johnson, V. D. Dasika, and R. S. Goldman, Applied Physics Letters **88**, 053109 (2006).

[20]H. Shin, E. Yoon, Y. H. Yoo, and W. Lee, Journal of the Physical Society of Japan **73**, 3378 (2004).

[21]H. Shin, Y. H. Yoo, and W. Lee, Journal of Physics D **36**, 2612 (2003).

Chapter 6

Summary and Suggestions for Future Work

6.1 Summary

Over the past several years, mercury cadmium telluride (MCT) and InAs/GaAs quantum dot heterostructures have enabled significant advances in optoelectronic devices. In both cases, further advances will require an improved understanding of the interface issues in these structures. For example, dark currents in MCT-based infrared detectors have been attributed to various defects at the heterostructure interfaces. Although earlier studies of MCT based heterostructures had revealed significant concentrations of point defect clusters[1] and dislocations[2] in MCT-based structures, only a few studies had considered the effects of alloy non-uniformities on detector properties.[3,4,5] In the case of InAs/GaAs self-assembled quantum dots, further advances in dot-based devices will require a narrowing of the density of states. This may be achieved through an improved understanding and control of dot size, density, and shape, and their influence on the electronic states. In this dissertation, II-VI substrate growth and processing procedures were developed to lower the substrate resistivity. In the future, these substrates can be used for the subsequent growth of MCT heterostructures to be examined using a combination of cross-sectional scanning tunneling microscopy (XSTM) and variable separation scanning tunneling spectroscopy (STS). In addition, the nanometer-scale influence of surrounding alloy layers on the structural properties of InAs/GaAs quantum dots were investigated using XSTM. Furthermore, the origins of electronic states in InAs/GaAs quantum dots were explored using a combination of XSTM and STS. In the following sections, a brief summary of the results from these studies will be presented.

6.1.1 CdZnTe Substrate Design and Characterization

We investigated the influence of substrate orientation and thickness on the cleavage of CdTe and $Cd_{0.96}Zn_{0.04}Te$ substrates, as well as the influence of In doping and annealing on the substrate resistivity. The flattest cleaves were achieved with (111)-oriented $Cd_{0.96}Zn_{0.04}Te$ and CdTe substrates. Furthermore, a thickness of 900 μm provided consistently flat cleaves for this material system. In an attempt to lower the resistivity of the substrates, the influence of doping and annealing were also investigated. Doping a CdTe crystal with indium to ~ 2.2×10^{17} cm^{-3} brought the resistivity down to 3-5 Ω-cm, and annealing the substrates under a Cd overpressure at 750 °C further reduced the resistivity to 0.04 Ω-cm. Thus, substrates suitable for the subsequent growth of epitaxial MCT layers for XSTM studies have been identified. These CdTe:In substrates also have potential applications in x-ray and γ-ray detectors.[6,7] Furthermore, a heterostructure to enable XSTM investigations of $Hg_{1-x}Cd_xTe$ films sensitive to mid-to-long wavelength infrared radiation was designed. Since Hg can vaporize from the MCT surface in appreciable quantities, at ~ 70 °C,[8,9] any cleaved pieces of MCT on the chamber bottom would release appreciable quantities of Hg during a chamber bakeout (typically ~ 150 °C), detrimentally contaminating the STM and the chamber. Thus, to pursue XSTM studies of the MCT heterostructures, a dedicated system with cleaving capabilities in a separate but interconnected chamber would be needed.

6.1.2 Influence of Alloy Buffer and Capping Layers on Quantum Dot Structure

The influence of $In_{0.2}Ga_{0.8}As$ alloy layers on the diameter, height, shape, and density of InAs dots, as well as the thickness of the surrounding WLs were investigated using XSTM. The lateral spacing between the AQDs was found to be lower than the lateral spacing between the QDs, suggesting that the alloy buffer layer promoted an increase in dot density. Furthermore, the alloy buffer and capping layers reduced the tendency for dot collapse, and the diffusion of In from the alloy layers surrounding the WL led to an increase in the apparent WL thickness. Taking into account the reduction in mismatch strain provided by the InGaAs alloy layers at the buffer/dot and dot/cap interfaces, a strain-based mechanism for dot formation and collapse in the absence and presence of InGaAs alloy layers was proposed. These results provide a valuable understanding of the relationship between growth conditions and structure of semiconductor dots, and are applicable to a wide range of similarly lattice-mismatched systems.

6.1.3 Influence of Structural Variations on Quantum Dot Electronic States

Nanometer-scale variations in the effective bandgap, the energy difference between the lowest confined electron (E_e) and hole (E_h) energies, within individual InAs/GaAs QDs and the clustered regions of the WL, were examined using variable separation STS.[10] The data reveal variations in the effective band gap across individual QDs both laterally and in the growth direction. Laterally, the effective bandgap decreases toward the QD core, and vertically, the effective bandgap decreases in the growth direction. These results are consistent with an increase in [In] toward the center and top of the QD, suggesting that [In] variations dominated the variations in QD effective bandgap. Similarly, in the clustered regions of the WL, [In] variations dominate the variations in the WL effective bandgap. Thus, the variations in effective bandgap are apparently dominated by indium composition gradients, with minimal effects due to QD shape and strain.

6.2 Suggestions for Future Work

In the following sections, suggestions for future work are described. In all cases, preliminary work has been completed by the author. The work in Harvard was supported by the Horace H. Rackham School of Graduate Studies and the Radcliffe Institute for Advanced Studies.

6.2.1 Influence of Dopant Atoms on QD Electronic States

Doping of III-V semiconductors with transition metals such as Mn leads to simultaneous semiconducting and ferromagnetic behavior, thus enabling devices such as spin-valves and spin-injection contacts.[11-19] In the case of QD structures, Mn-doping enables the achievement of spin-polarized optoelectronic devices such as lasers and LEDs.[13-16] For epitaxially grown GaMnAs heterostructures, ferromagnetism has been reported to occur below the reported Curie temperature of < 180 K, although the use of ion implantation to form nano-clusters of MnAs in GaAs has produced Curie temperatures as high as 360 K.[20-22] On the other hand, for InAs:Mn QDs, Curie temperatures > 300 K have been reported.[15-18] It has been suggested that Mn atoms act as acceptors in both GaAs and in InAs QDs,[13,14] and prior STS studies have revealed the presence of mid-gap states in the STS spectra of GaAs:Mn and InAs:Mn. Furthermore, it has been suggested that the majority of the Mn atoms in InAs:Mn QDs are contained within the QD, rather than in the surrounding GaAs matrix.[16] However, those conclusions are based upon Electron Energy Loss Spectroscopy (EELS) measurements performed in a TEM, which has a limited spatial resolution as discussed in Section 1.2 of this dissertation.[23-25] Thus, the distribution of the Mn atoms in and around the QDs and the influence of Mn atoms on QD electronic states remains unknown.

To examine the atomic-scale distribution of Mn atoms and their influence on the electronics states of the InAs:Mn QDs, a combination of XSTM and STS is a promising alternative. Using XSTM, we have previously quantified the distribution of Mn defects in GaMnAs films,[26] and using STS, we have previously compared measurements of the effective bandgap from different locations within the same QD, as discussed in Chapter

5.[10] Thus, we have the tools and skills necessary to study the distribution and influence of Mn atoms in and around InAs:Mn QDs.

To examine the influence of Mn atoms on the QD effective bandgap, STS spectra were acquired from the QD center, edge, and surrounding GaAs matrix, of the structure shown in Fig. A.2 of Appendix A.[16] Preliminary STS data from InAs:Mn QDs reveals mid-gap features indicated by arrows in Fig. 6.1. The mid-gap features are most likely due to states associated with Mn atoms, similar to a recent report for bulk-like InAs:Mn.[24] From the STS data, it appears that the number of mid-gap features increases towards the outskirts of the QD. For example, there are more mid-gap features at the QD edge compared to the QD core. In addition, there are significantly more features in the GaAs surrounding the QDs in comparison to those of the QD core and QD edge. Thus, it is likely that the Mn dopants within the QD modify the band structure of the surrounding GaAs.

In the future, additional XSTM and STS measurements are suggested to further quantify the distribution of Mn atoms and their influence on the band structure of the QDs and surrounding GaAs matrix. XSTM would be used to map out the distribution of the Mn atoms in and around the QDs. STS data would allow the quantification of energies of the mid-gap features with position relative to the QD core, and a comparison of STS spectra from the InAs QDs and the InAs:Mn QDs would enable further analysis of the source of the mid-gap features observed in the STS spectra. In addition, low temperature STS measurements would enable (i) a greater energy resolution in the spectra, as will be discussed in Section 6.2.3, and (ii) the measurement of the Mn-induced electronic states at temperatures below the Curie temperature.

6.2.2 Effect of Capping on Quantum Dot Structure and Electronic States

To date, the influence of alloy buffer and capping layers has primarily been investigated qualitatively using plan-view STM or AFM, and therefore, the quantitative structure of the buried dots was not resolved.[27-29] In Chapter 4, XSTM studies of the influence of alloy layers on InAs dot formation suggested that the use of buffer and capping layers composed of InGaAs in lieu of GaAs promotes an increase in dot dimensions.[30] However, the separate influence of alloy buffer and capping layers was not considered. Using a combination of plan-view STM and XSTM, it would be possible to consider the effects of the alloy buffer and capping layers separately. To investigate the influence of alloy buffer layers on dot dimensions, 3 ML InAs dots grown on (i) a GaAs buffer or (ii) an $In_{0.2}Ga_{0.8}As$ buffer would be examined using in situ plan-view STM. STM images such as the one shown in Fig. 6.2 would be used to quantify the dot diameters, height, and density. The dots would then be capped with (i) 300 nm GaAs or (ii) an $In_{0.2}Ga_{0.8}As$ capping layer followed by 300 nm GaAs. Subsequent XSTM measurements are expected to reveal the influence of the alloy capping layers on dot dimensions, shape, and density, as well as WL thickness. Thus, using a combination of plan-view STM and XSTM to measure dot dimensions both before and after capping (with GaAs or $In_{0.2}Ga_{0.8}As$), it should be possible to quantify the enhancement or reduction in dot dimensions due to the capping layer.

6.2.3 Low Temperature STS of Quantum Dots and Wetting Layer

In this thesis, the room temperature structural and electronic properties of QDs were investigated using a combination of XSTM and variable separation STS. These room temperature XSTM and STS results provided insight into how the electronic band structure varies within individual QDs. However, many of the confined states within the nanostructures are expected to be separated by fractions of kT, and due to thermal broadening at room temperature, only the ground states could be measured in this thesis. To improve the energy resolution of the spectra, it is necessary to perform XSTM and STS experiments at low temperatures. To date, in addition to the room temperature measurements presented in this dissertation, the author also used an Omicron VT-25 at Harvard University during January – June 2006. Prior to the trip to Harvard, modifications to the sample holders, cleaving tool, and telescope, were designed. Upon arrival at Harvard, further modifications to the sample holders and cleaving tool were made, and a number of programs were written to drive the data collection electronics for STS. Details of the sample holder design and cleaver modifications are provided below. An additional opportunity to perform low temperature measurements on the Omicron VT was available at the Materials Research Lab (MRL) at the University of Illinois at Urbana Champaign (UIUC), and the research staff suggested an alternate sample holder configuration, which will also be discussed in this section. In August 2009, the Goldman group acquired a new Omicron VT, and the designs from the trip to Harvard were used to fabricate additional sample holders for use at Michigan.

XSTM Sample Holder (SH) Design for Low Temperature Experiments

For XSTM, special sample holders, which minimize vibration, but enable sample cleaving, are needed. To design the new XSTM sample holder (SH) for low temperature experiments, we first considered the key features of the Park Autoprobe VP SH used to obtain all the data in this thesis, shown in Fig. 6.3(a). This was described in more detail in Chapter 2 of this thesis, and in the PhD thesis of B. Lita.[31] For the Autoprobe VP, to minimize sample vibrations, the entire SH was carved out of one large piece of molybdenum. Within the SH, the cantilever-shaped sample was clamped by metal plates termed SH 'jaws'. The moveable lower 'jaw' of the SH, shown in Fig. 6.3(a), enabled positioning the sample flush against the back of the SH prior to subsequent sample clamping.

To optimize the design of the new XSTM SH, the key features of the Autoprobe VP SH were carefully mapped onto the Omicron VT STM, considering size and design differences. First, the SH size was scaled down to fit into the Omicron VT stage, with dimensions of 1.8 cm × 1.2 cm (in lieu of the 3.1 cm × 3.1 cm for the Autoprobe VP). Carving such a small SH out of one piece of molybdenum proved to be difficult because it is very brittle. To provide thermal isolation between the STM electronics and the sample, the Omicron VT SH includes a top ceramic plate with a window to allow tip access, as shown in Fig. 6.3(b). The top ceramic plate is attached to the metal SH using threaded rods and spacers, as shown in Fig. 6.3(c). This connection was enabled by drilling 1 mm screw holes into the base plate.

An alternate SH design was suggested by the research staff at the UIUC MRL, but the SH could not be used for our experiments. The SH modification involved a single clamping screw would be used, as shown in Fig. 6.4. However, the single screw was ineffective in clamping the sample (leading to the sample falling out of the SH jaws), and thus, the single-screw SH could not be used. Therefore, for the new Omicron VT of the Goldman group, we have fabricated SHs using our original Omicron VT XSTM SH design shown in Figs. 6.3(b) and (c).

Cleaver Design

For XSTM, cleaving is typically performed in the UHV chamber by lowering a cleaver onto the sample in a controlled manner. In the Autoprobe VP, to cleave the sample, the fixture containing a 60˚ diamond tip is lowered via a Z-linear slider on the manipulator. Cleaving is achieved by the controlled lowering of the diamond tip until it is in contact with the sample surface. Ideally, this causes the sample to cleave along the scribe mark, ideally revealing a flat surface. Additional details on cleaving the sample in the Autoprobe VP are provided in Chapter 2 of this thesis and in the PhD Thesis of Dr. B. Lita.[31]

For the experiments at Harvard, we used the cleaver from Omicron, which consisted of a 2-armed clamping device. Since our samples are cleaved from the epilayer side and not the substrate side, as discussed in Section 2.3.5, we utilized only one arm of the Omicron cleaver. In addition, to utilize the 1-armed Omicron cleaver, the samples were vertically oriented during the cleaving. Thus, the cleaved pieces would often land on the sample instead of falling to the bottom of the chamber.

To avoid such problems in the new VT-STM, the author designed a new cleaver to be mounted on top of the analysis chamber of the Omicron VT STM, as shown in Fig.

6.5. The cleaver consists of a metal rod connected to a linear feed-through. A diamond tip mounted onto the end of the metal rod will contact the sample in order to cleave it. The linear feed-through will allow us to extend the cleaver into the chamber in order to cleave the sample, and then, after cleaving, retract the cleaver away from the center of the chamber, as shown in Fig. 6.5.

Low T STM/STS Measurements

The author was able to test the first generation of the SHs in 2006 while visiting Harvard, and the preliminary data is discussed in this paragraph. An XSTM topographic image of an InAs/GaAs QD is presented in Fig. 6.6(a), where the bright ellipse corresponds to an InAs QD in a GaAs matrix. In Fig. 6.6 (b), the normalized conductance versus sample bias voltage is plotted for the edge and center of the QD shown in Fig. 6.6(a), in comparison with a region of clean GaAs. The effective bandgap decreases laterally towards the center of the QD, similar to the trend discussed in Section 5.4 of this dissertation. However, we note that the measured bandgaps are larger than the expected values for GaAs and the QD. Since the system at Harvard lacked a suitable tip preparation tool, the STM tips were not cleaned via electron emission prior to the experiments, and were likely covered in a layer of oxide.

It is anticipated that using the new sample holder and cleaver on the Goldman Group Omicron VT, combined with the in-situ tip preparation tool (which will enable tip cleaning prior to experiments as discussed in Section 2.3.4) will enable low temperature STS measurements from the InAs/GaAs QD samples. Thus, experiments are planned to examine the influence of temperature on the QD and WL electronic states, and will likely reveal a series of features corresponding to the hole and electron ground and excited states separated by an effective bandgap.[32-35] The influence of dopant atoms such as Mn can also be examined at both room and low temperatures using the Omicron VT.

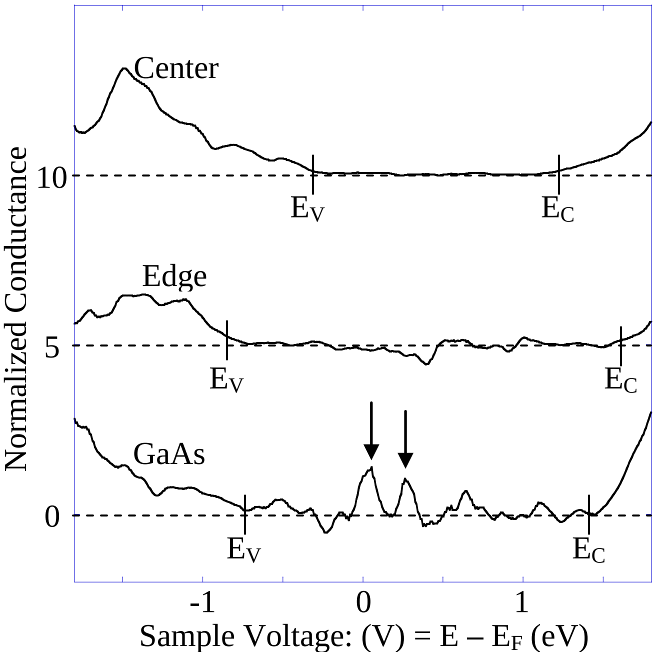

Fig. 6.1: Plot of spatially-resolved STS spectra from the center and edge of InAs:Mn QDs, in comparison with a region of clean GaAs. The effective valence and conduction band edges are indicated by vertical lines at negative and positive sample voltages, respectively. The sample voltage corresponds to the energy relative to the Fermi level. Vertical arrows indicate mid-gap features in the GaAs spectrum, which presumably correspond to Mn-induced electronic states.

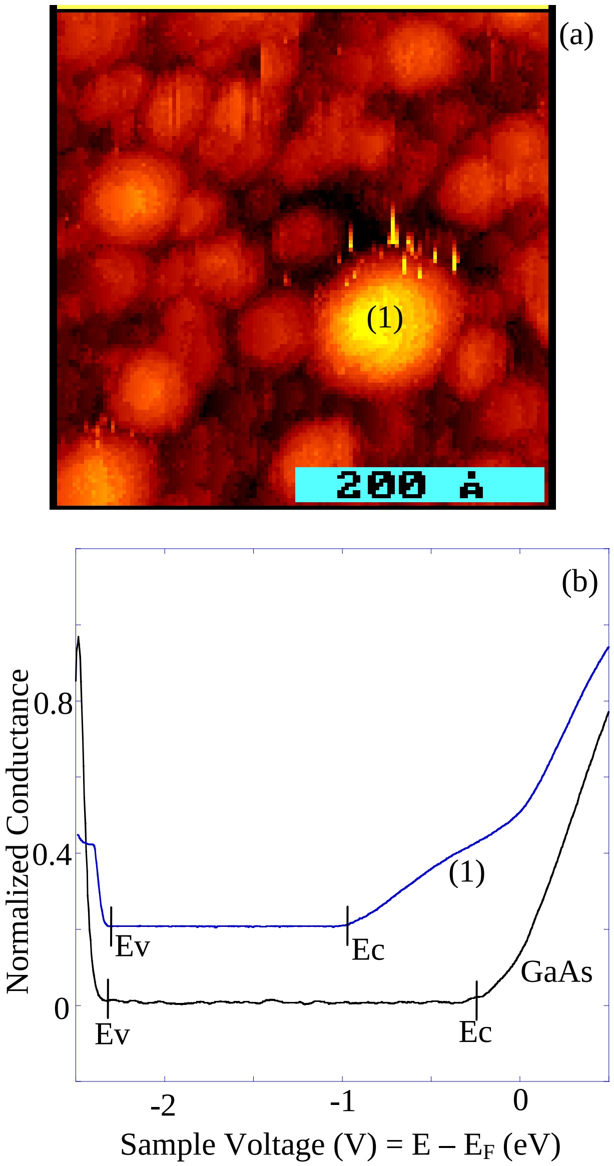

Fig. 6.2: (a) Plan-view STM topographic image of InAs/GaAs quantum dots grown on a GaAs buffer acquired at a sample bias of -2.0 V. The scale bar has not been corrected to account for scanner calibration. In (b), a spatially-resolved STS spectrum from point (1) is plotted in comparison with a region of clean GaAs. The effective valence and conduction band edges are indicated by vertical lines. The sample voltage corresponds to the energy relative to the Fermi level. The measured bandgap is 1.90 eV (1.23 eV) for the GaAs (QD). Although the bandgaps are larger than the expected values of 1.43 eV (0.36 eV), the appropriate trend (InAs E_g < GaAs E_g) is apparent.

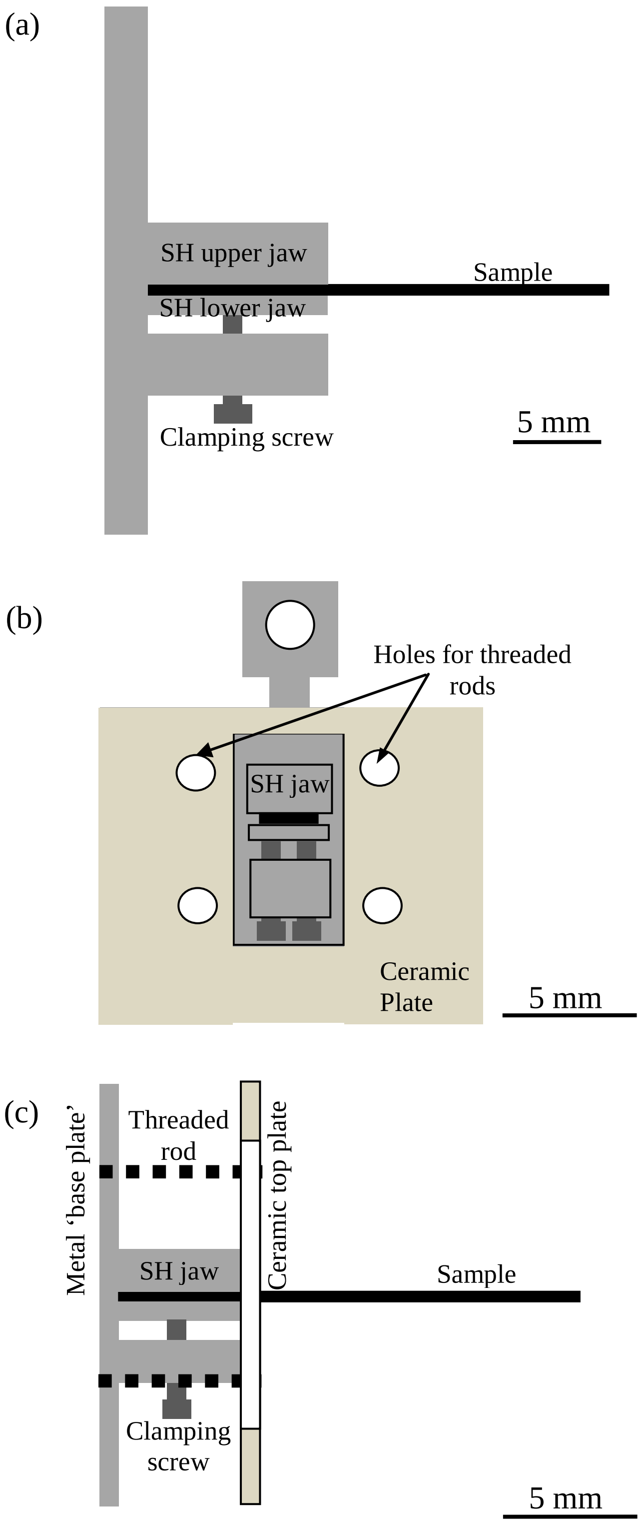

Fig. 6.3: (a) Diagram of PSI XSTM sample holder showing the key features including a moveable clamping plate and 'jaws'. Diagram of the (b) front and (c) side views of the new XSTM sample holder for the Omicron VT-25.

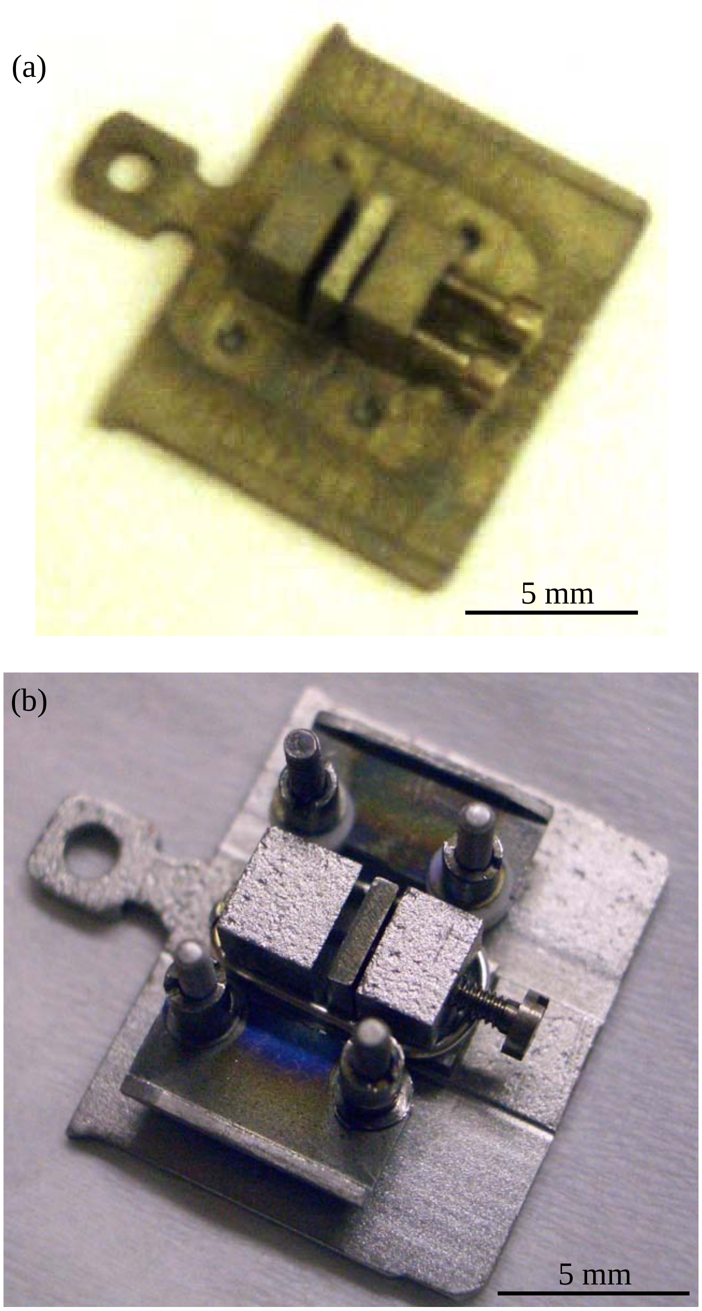

Fig. 6.4: (a) Sample holder designed by the author and fabricated at Harvard. Two screws are used to clamp the sample in the holder. (b) Sample holder suggested by research staff at the MRL in UIUC. Since only one clamping screw is used in this case, the sample holder was ineffective at clamping the sample within the sample holder jaws.

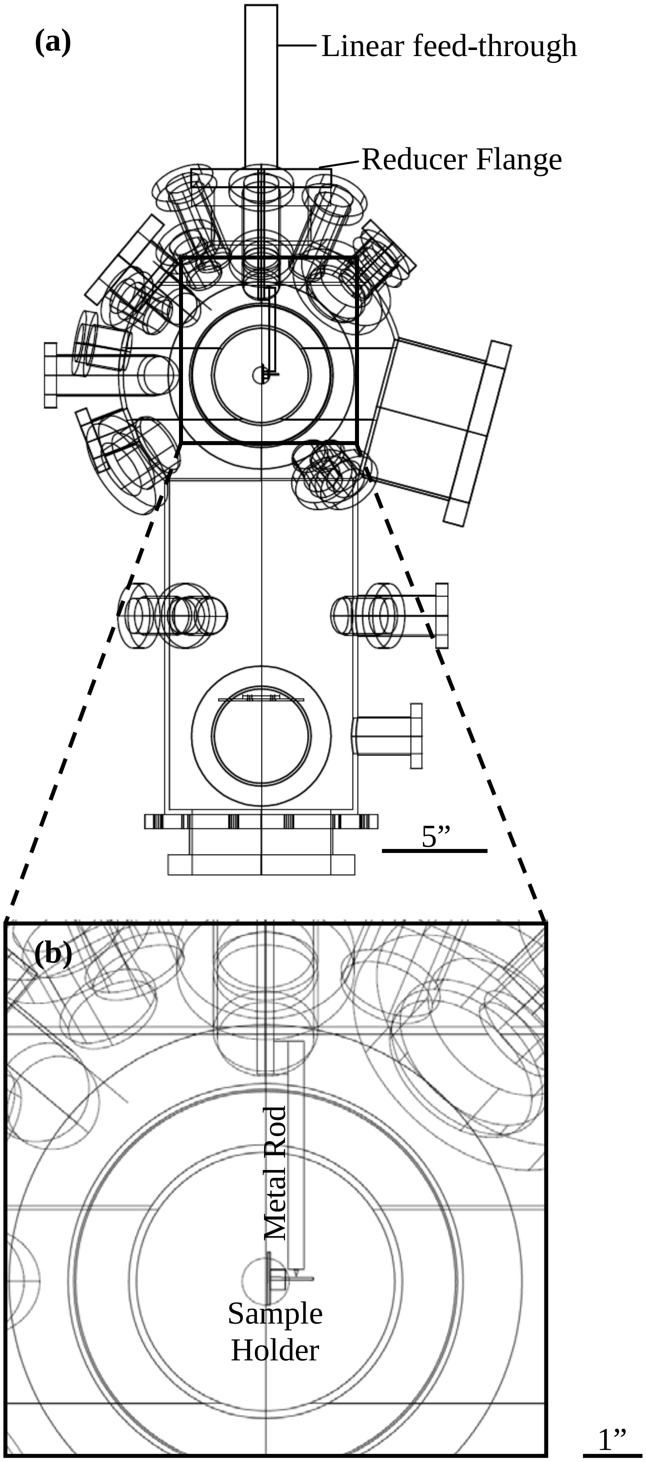

Fig. 6.5: Cleaver design for Omicron VT-25. (a) The cleaver is mounted on the top of the analysis chamber and consists of a metal rode connected to a linear feedthrough. (b) The diamond tip mounted onto the end of the metal rod contacts the sample in order to cleave it. The linear feedthrough extends or retracts the cleaver in the chamber.

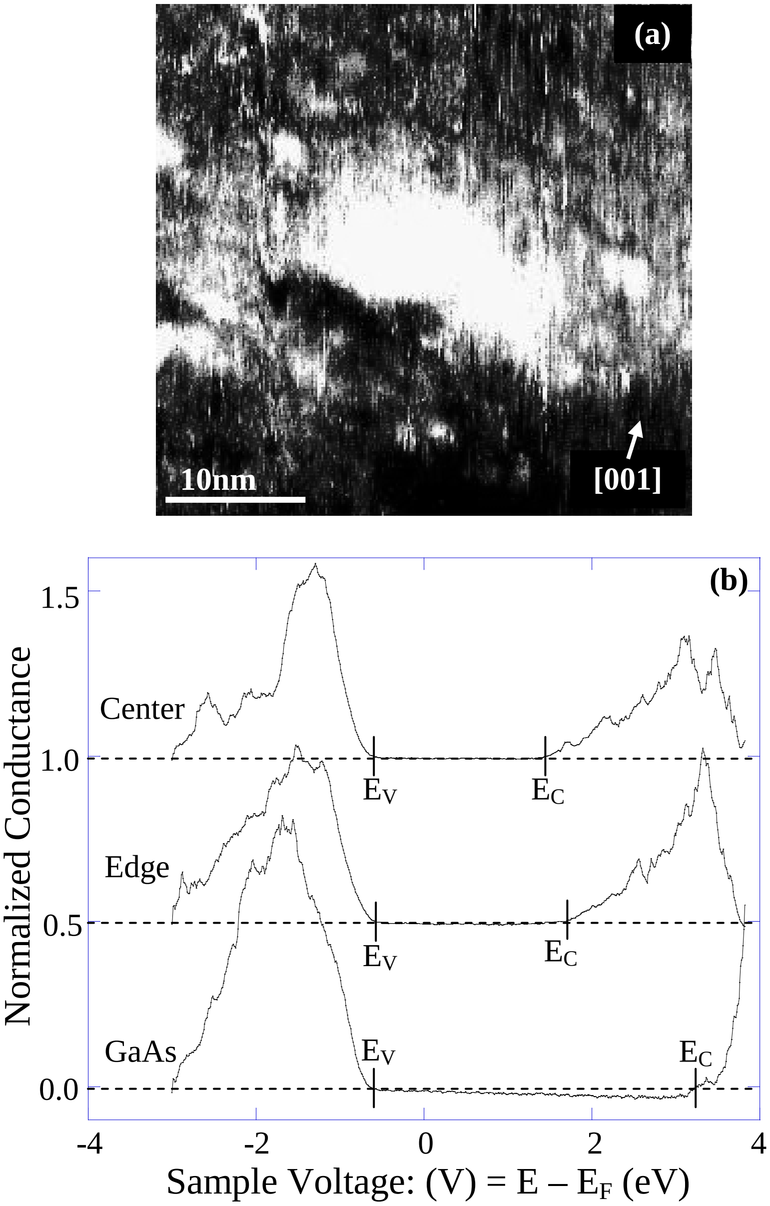

Fig. 6.6: (a) XSTM topographic image of InAs/GaAs quantum dots grown on a GaAs buffer acquired with the Omicron VT-25 at Harvard University, using a sample bias of -2.0 V. Spatially-resolved STS spectra from the edge and center of the QD are plotted in (b), in comparison with a region of clean GaAs. The effective valence and conduction band edges are indicated by vertical lines. The sample voltage corresponds to the energy relative to the Fermi level. The effective bandgap at the QD edge is larger than the effective bandgap at the QD center, mimicking the trend observed in Chapter 5.

6.3 References

[1]N. Mainzer and E. Zolotoyabko, Diffusion and Defect Data A **183**, 103 (2000).

[2]T. Aoki, Y. Chang, G. Badano, J. Zhao, C. Grein, S. Sivananthan, and D. J. Smith, Journal of Crystal Growth **265**, 224 (2004).

[3]X. Z. Liao and T. S. Shi, Applied Physics Letters **66**, 2089 (1995).

[4]M. W. Muller and A. Sher, Applied Physics Letters **74**, 2343 (1999).

[5]J. D. Phillips, K. Moazzami, J. Kim, D. D. Edwall, D. L. Lee, and J. M. Arias, Applied Physics Letters **83**, 3701 (2003).

[6]C. Matsumoto, T. Takahashi, K. Takizawa, R. Ohno, T. Ozaki, and K. Mori, IEEE Transactions on Nuclear Science **45**, 428 (1998).

[7]C. Szeles, Physica Status Solidi (b) **241**, 783 (2004).

[8]J.-P. Faurie, Progress in Crystal Growth and Characterization of Materials **29**, 85 (1994).

[9]R. F. C. Farrow, G. R. Jones, G. M. Williams, P. W. Sullivan, W. J. O. Boyle, and J. T. M. Wotherspoon, Journal of Physics D **12**, L117 (1979).

[10]V. D. Dasika, R. S. Goldman, J. D. Song, W. J. Choi, N. K. Cho, and J. I. Lee, Journal of Applied Physics **106**, 014315 (2009).

[11]T. Hayashi, M. Tanaka, T. Nishinaga, H. Shimada, H. Tsuchiya, and Y. Otuka, Journal of Crystal Growth **175-176**, 1063 (1997).

[12]J. De Boeck, R. Oesterholt, H. Bender, A. Van Esch, C. Bruynseraede, C. Van Hoof, and G. Borghs, Journal of Magnetism and Magnetic Materials **156**, 148 (1996).

[13]A. Kudelski, A. Lemaitre, A. Miard, P. Voisin, T. C. M. Graham, R. J. Warburton, and O. Krebs, Physical Review Letters **99**, 247209 (2007).

[14]J. van Bree, P. M. Koenraad, and J. Fernandez-Rossier, Physical Review B **78**, 165414 (2008).

[15]S. Chakrabarti, M. A. Holub, P. Bhattacharya, T. D. Mishima, M. B. Santos, M. B. Johnson, and D. A. Blom, Nano Letters **5**, 209 (2004).

[16]M. Holub, S. Chakrabarti, S. Fathpour, P. Bhattacharya, Y. Lei, and S. Ghosh, Applied Physics Letters **85**, 973 (2004).

[17]L. J. Hu, Y. H. Chen, X. L. Ye, Y. H. Jiao, L. W. Shi, and Z. G. Wang, Physica E **40**, 2869 (2008).

[18] X. W. Zhang, W. J. Fan, S. S. Li, and J. B. Xia, Applied Physics Letters **92**, 013129 (2008).

[19] M. Holub, J. Shin, S. Chakrabarti, and P. Bhattacharya, Applied Physics Letters **87**, 091108 (2005).

[20] K. W. Edmonds, K. Y. Wang, R. P. Campion, A. C. Neumann, N. R. S. Farley, B. L. Gallagher, and C. T. Foxon, Applied Physics Letters **81**, 4991 (2002).

[21] K. Olejnik, M. H. S. Owen, V. Novak, J. Masek, A. C. Irvine, J. Wunderlich, and T. Jungwirth, Physical Review B **78**, 054403 (2008).

[22] M. Wang, R. P. Campion, A. W. Rushforth, K. W. Edmonds, C. T. Foxon, and B. L. Gallagher, Applied Physics Letters **93**, 132103 (2008).

[23] D. Kitchen, A. Richardella, J.-M. Tang, M. E. Flatte, and A. Yazdani, Nature **442**, 436 (2006).

[24] F. Marczinowski, J. Wiebe, J.-M. Tang, M. E. Flatte, F. Meier, M. Morgenstern, and R. Wiesendanger, Physical Review Letters **99**, 157202 (2007).

[25] S. Loth, M. Wenderoth, and R. G. Ulbrich, Physical Review B **77**, 115344 (2008).

[26] J. N. Gleason, M. E. Hjelmstad, V. D. Dasika, R. S. Goldman, S. Fathpour, S. Charkrabarti, and P. K. Bhattacharya, Applied Physics Letters **86**, 011911 (2005).

[27] R. Songmuang, S. Kiravittaya, and O. G. Schmidt, Journal of Crystal Growth **249**, 416 (2003).

[28] G. Costantini, A. Rastelli, C. Manzano, P. Acosta-Diaz, R. Songmuang, G. Katsaros, O. Schmidt, and K. Kern, Physical Review Letters **96** (2006).

[29] J. M. Ulloa, C. Celebi, P. M. Koenraad, A. Simon, E. Gapihan, A. Letoublon, N. Bertru, I. Drouzas, D. J. Mowbray, M. J. Steer, and M. Hopkinson, Journal of Applied Physics **101**, 081707 (2007).

[30] V. D. Dasika, J. D. Song, W. J. Choi, N. K. Cho, J. I. Lee, and R. S. Goldman, Applied Physics Letters **95** (2009).

[31] B. Lita, Ph.D. Thesis, University of Michigan, 2002.

[32] O. Millo, D. Katz, Y. W. Cao, and U. Banin, Physical Review B **61**, 16773 (2000).

[33] O. Millo, D. Katz, Y. Cao, and U. Banin, Physical Review Letters **86**, 5751 (2001).

[34] B. Wang, K. Wang, W. Lu, J. Yang, and J. G. Hou, Physical Review B **70**, 205411 (2004).

[35] P. Liljeroth, P. A. Z. van Emmichoven, S. G. Hickey, H. Weller, B. Grandidier, G. Allan, and D. Vanmaekelbergh, Physical Review Letters **95**, 086801 (2005).

Appendix A

InAs/GaAs Quantum Dot Sample Growth Details

In this appendix, the growth details for the samples examined in Chapters 4, 5, and 6 of this dissertation are described. This includes the uncoupled InAs/GaAs quantum dot superlattices with and without surrounding alloy layers, discussed in Chapters 4 and 5, and the InAs/GaAs quantum dots doped with Mn, discussed in Chapter 6.

The samples examined in Chapters 4 and 5 of this dissertation were grown by Dr. J. D. Song and his group at the Korea Institute of Technology (KIST).[1,2] The epitaxial layers were grown on (001) *n*+ GaAs substrates in a solid-source VG80 MBE. The heterostructures consisted of one layer of InAs dots with $In_{0.2}Ga_{0.8}As$ alloy buffer and capping layers (termed alloy quantum dots or "AQDs"), and 3 sets of superlattices (SLs) with 1, 3, and 8 layers of 3 ML InAs quantum dots (QDs), without surrounding alloy layers, followed by 50 nm of GaAs. Each set of SLs was separated by a multilayer consisting of 20 or 40 nm of AlAs/GaAs short-period SLs sandwiched between two 70 nm GaAs layers. The dot layers were separated by > 50 nm of GaAs to prevent dot stacking and coupling.

In both cases, for dot growth, the In and As were deposited alternately for 8s, followed by a 5s growth interruption in the absence of As to allow dot nucleation.[1] The beam equivalent pressures for In and As were ~ 10^{-8} Torr and ~ 10^{-7} Torr respectively. A total of 3ML InAs was deposited in this way. For the AQD layers, the dots were grown on 1.25 nm of $In_{0.2}Ga_{0.8}As$, followed by capping with 7.5 nm of $In_{0.2}Ga_{0.8}As$. The entire structure was grown at 480ºC and capped with 300 nm GaAs, as shown in Fig. A1. All layers, except the InAs and $In_{0.2}Ga_{0.8}As$ layers, were Si-doped at ~ 3×10^{18} cm^{-3}. The targeted buffer/dot mismatch strain, ε, is 6.7% for the QDs and 5.4% for the AQDs.

The InAs:Mn QD structure discussed in Chapter 6 was grown via MBE by Dr. M. Holub at the University of Michgan.[3] The samples were grown on (001)-oriented *p*+ GaAs substrates in a Varian GEN-II MBE. The heterostructures consisted of one layer of InAs QDs and one layer of InAs:Mn QDs (10% Mn) separated by 20 nm of GaAs. First, a 500 nm GaAs buffer layer, followed by 40 nm AlAs/GaAs superlattices and 50 nm of GaAs were grown at 610 °C.[4] The substrate temperature was then reduced to 280 °C, and 4.2 ML of InAs were deposited, followed by a 45 second growth interruption to allow dot formation. Next, a 20 nm GaAs spacer layer was grown, followed by the InAs:Mn QDs. For the growth of the InAs:Mn QDs, 2.0 ML of InAs was initially deposited in the absence of Mn. The Mn effusion cell shutter was then opened for the growth of the final 2.2 ML of InAs, thus producing InAs:Mn QDs. Dot growth was again followed by a 45 second growth interruption prior to additional capping at the low growth temperature. During the growth of this structure, an As_4:Ga beam equivalent pressure of ~16:1 was used, and the InAs growth rate was 0.07ML/s. The structure was capped with 500 nm GaAs, and all layers, except the InAs QDs, were Be doped at ~ 5×10^{18} cm^{-3} as shown in Fig. A2.

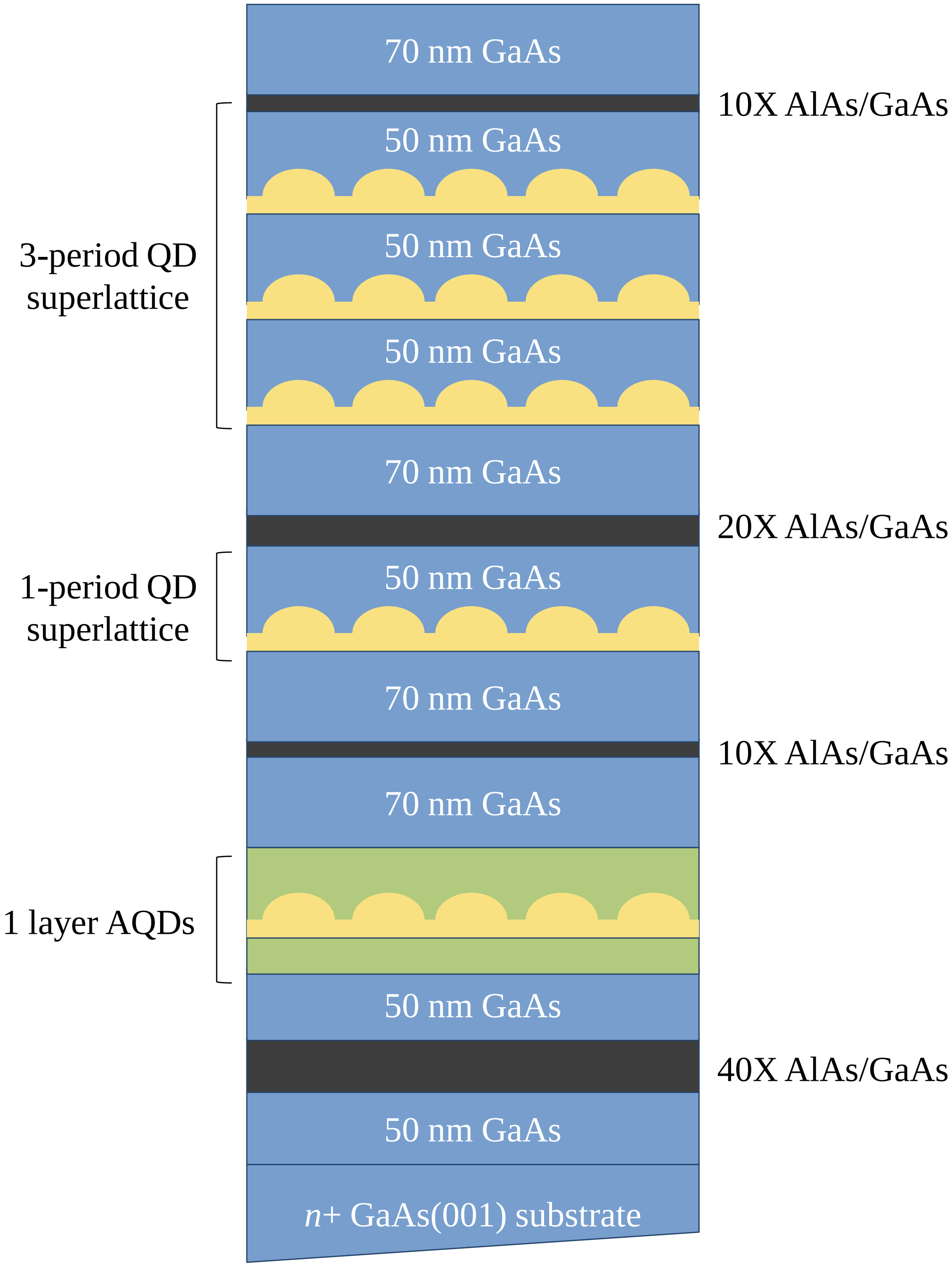

Fig. A1: Cross-section of the target layer structure which consisted of Si-doped 1-, 3-, and 8-period QD superlattices (SLs) consisting of 3 ML InAs and 50 nm GaAs, and an AQD layer grown on 1.25 nm $In_{0.2}Ga_{0.8}As$ and capped with 7.5 nm $In_{0.2}Ga_{0.8}As$. The entire structure was grown on a (001)-oriented GaAs substrate. Each set of QD SLs was separated by a by a multilayer consisting of 20 or 40 nm of AlAs/GaAs short-period SLs sandwiched between two 70 nm GaAs layers. Not shown in the diagram are the 8-period QD SL followed by a 300 nm GaAs cap.

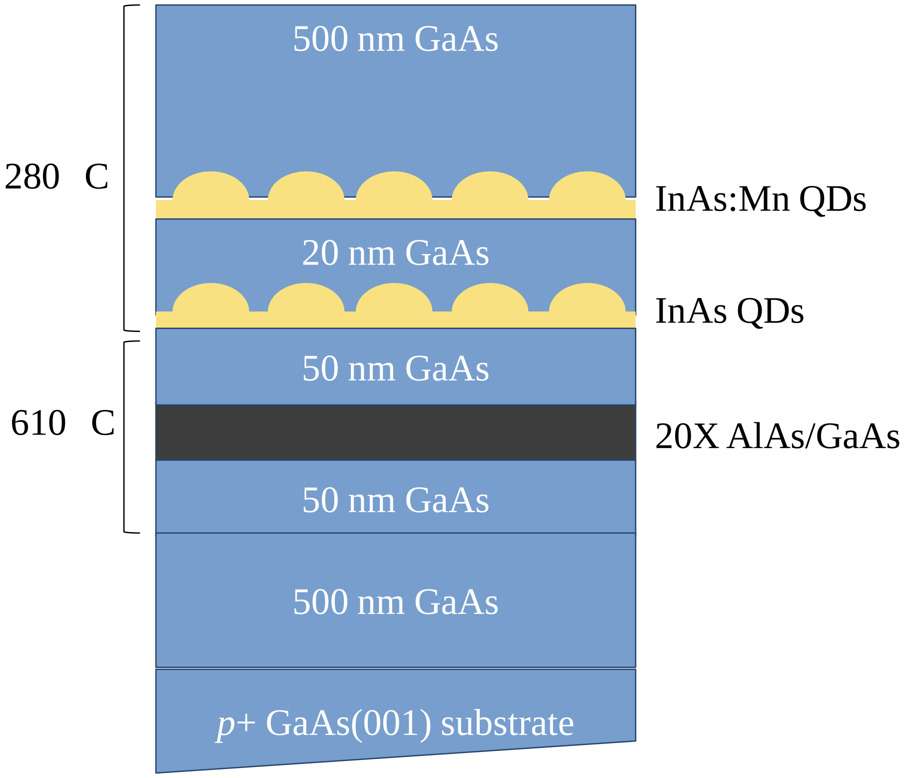

Fig. A2: Cross-section of the target layer structure which consisted of 1 layer of 4.2 ML InAs QDs and 1 layer of 4.2 ML InAs QD doped with 10% Mn, separated by 20 nm GaAs. A multilayer consisting of 20 nm of AlAs/GaAs short-period SLs sandwiched between two 50 nm GaAs layers was grown on top of a buffer layer at 610 C. The QD layers and 500 nm cap layer were grown at 280 C. The entire structure was grown on a *p*+ (001)-oriented GaAs substrate.

Appendix B

Tip Height Criterion for QDs and the Clustered Regions of the WL

This Appendix describes the tip height criterion used to differentiate the GaAs, the clustered regions of the WL, and the QDs and AQDs that were discussed in Chapters 4 and 5 of this dissertation. The Line Analysis tool of the Park Scientific Instruments' (PSI) Image Processing Software, version 1.5 was used for this analysis. Details of the Line Analysis tool are described in Appendix D of the Ph.D. Thesis of Dr. B. Lita.[5] Plots of the "line-cut", i.e., the variation in tip height as a function of position, are also included in his thesis.

To differentiate the GaAs, the QDs, and the clustered regions of the WL, we estimated the tip height criterion as follows. Bright regions with maximum tip heights at least 2.1 Å above the GaAs background were considered to be possible QDs. Within the bright regions, pixels with tip heights at least 1.1 Å above the GaAs background were considered to be part of the QD.[5] Surrounding the QDs, bright regions with maximum tip heights between 0.4 and 1.5 Å above the GaAs background were considered to be possible clustered WL In atoms. Within these regions of the WL, we estimated an indium atom tip height criterion of 0.85 Å ± 0.05 Å with respect to the GaAs background.[6]

Appendix C

Correction Factor for Tip Induced Band Bending

This Appendix describes the procedure that was used for a linear correction of the tip-induced band bending in the STS spectra from the clustered regions of the WL, discussed in Section 5.5 of this dissertation. The linear correction for tip-induced band bending described here provides a reasonable estimate of the measured bandgap for bulk semiconductors (such as GaAs) after correcting for tip-induced band bending.[7] However, for dimensionally confined structures (such as the InAs QDs), a more detailed calculation is necessary to correct for the tip-induced band bending. As discussed in Section 2.5, we are in the process of calculating the influence of tip-induced band bending in InAs QDs using three-dimensional finite element analysis.[8]

Following an STS measurement, the measured differential conductance is normalized using the procedure described in Section 2.4 of this dissertation. Plots of the normalized conductance are used to estimate the energetic positions of the valence (E_V) and conduction band (E_C) edges, using the analysis described in Section 2.4. When the measured bandgap for the GaAs spectrum is larger than expected, this is usually due to tip induced band bending. As a first approximation, we multiply the measured value for E_C and E_V by a correction factor which produces a GaAs bandgap of 1.42 eV. Thus, the correction factor, CF, is defined as:

$$CF = \frac{1.42}{E_{C(measured)} - E_{V(measured)}} \qquad \text{(C.1)}$$

After *CF* has been calculated using a calibration spectrum for the GaAs, the values for the effective conductance (E_e) and valence (E_h) band edges in the QDs and WL can be corrected using the equations below:[7]

$$E_e = E_{e(measured)}*CF \qquad \text{(C.2)}$$

$$E_h = E_{h(measured)}*CF \qquad \text{(C.3)}$$

Thus, measured values for E_e and E_h can be approximately corrected for tip induced band bending.

Appendix D

Materials Parameters

This appendix lists a variety of materials parameters used in this dissertation. Table D.1 lists the material parameters of the II-VI and III-V semiconductors used in Chapters 3, 4, and 5 of this dissertation.[9-11] Silicon has also been included in the table because of it is commonly used as a substrate for the subsequent growth of $Hg_{1-x}Cd_xTe$ heterostructures.[9,12] The microhardness value for $In_{0.2}Ga_{0.8}As$ was calculated using a linear interpolation of the microhardness values of InAs and GaAs.

Material	Lattice Parameter (Å)	Microhardness (kg/mm^2)
Si	5.43	985
CdTe	6.48	47
ZnTe	6.10	67
HgTe	6.46	23
GaAs	5.65	670
InAs	6.06	310
$In_{0.2}Ga_{0.8}As$	5.73	598

Table D.1: Material parameters of the II-VI and III-V semiconductors used in this dissertation, in comparison to Si. [9-12]

References

[1] J. D. Song, Y. M. Park, J. C. Shin, J. G. Lim, Y. J. Park, W. J. Choi, I. K. Han, J. I. Lee, H. S. Kim, and C. G. Park, Journal of Applied Physics **96**, 4122 (2004).

[2] N. K. Cho, S. P. Ryu, J. D. Song, W. J. Choi, J. I. Lee, and H. Jeon, Applied Physics Letters **88**, 133104 (2006).

[3] M. Holub, S. Chakrabarti, S. Fathpour, P. Bhattacharya, Y. Lei, and S. Ghosh, Applied Physics Letters **85**, 973 (2004).

[4] J. N. Gleason, Master's Thesis, University of Michigan, 2006.

[5] B. Lita, Ph.D. Thesis, University of Michigan, 2001.

[6] B. Shin, B. Lita, R. S. Goldman, J. D. Phillips, and P. K. Bhattacharya, Applied Physics Letters **81**, 1423 (2002).

[7] R. M. Feenstra, Y. Dong, M. P. Semtsiv, and W. T. Masselink, Nanotechnology **18** (2007).

[8] W. Morgan, H. T. Johnson, V. D. Dasika, and R. S. Goldman, (in preparation).

[9] O. Madelung, *Semiconductors - Basic Data*. (Springer-Verlag, 1996).

[10] E. P. Trifonova and L. Hitova, Thin Solid Films **224**, 153 (1993).

[11] R. Triboulet, A. Lasbley, B. Toulouse, and R. Granger, Journal of Crystal Growth **79**, 695 (1986).

[12] A. V. Brodovoy, V. A. Brodovoy, and V. A. Skryshevsky, Applied Surface Science **225**, 170 (2004).